Einsatz von FRET-Flim zur Beobachtung von Protein-Protein Wechselwirkungen in Lebenden Zellen: Einblicke in Interaktionen des Präsynaptischen Proteins Bassoon

Investigating Protein-Protein Interactions by FRET-Flim in Living Cells: Insights into Interactions mediated by the Presynaptic Protein Bassoon

Dissertation

zur Erlangung des akademischen Grades

doctor rerum naturalium
(Dr. rer. nat.)

genehmigt durch die Fakultät für Naturwissenschaften
der Otto-von-Guericke-Universität Magdeburg

von **Master of Science in Physics Mini Jose**

geb. am 26.12.1979 in Kanjirapally, Kerala, India

Gutachter: Prof. Dr. Eckart D. Gundelfinger
Prof. Dr. Fred S. Wouters

eingereicht am 24. April 2007

verteidigt am 25. October 2007

Dedicated to my loving father, late Prof. Dr. P.K. Jose, Director, School of Distance Education, Mahatma Gandhi University, Kerala, India without whose support, I would never have achieved what I have.

ACKNOWLEDGEMENTS

24th April 2007, Magdeburg   _____

Mini Jose

TABLE OF CONTENTS

SUMMARY

Förster's Resonance Energy Transfer (FRET) combined with Fluorescence Lifetime Imaging Microscopy (FLIM) is becoming a powerful tool to map protein-protein interactions in living specimens. In contrast to the in vitro methods which are useful to assess the potential of proteins for physical interactions, a combination of these techniques provides high spatial (nanometer) and temporal resolution (picosecond) in monitoring interactions within protein complexes in their natural environment. A completely new microscopic system including non-scanning detectors based on Time and Space Correlated Single Photon Counting was constructed for the interaction studies. In time-domain FLIM, the plots of contributions of the different lifetimes of the donor and acceptor fluorophores as a function of wavelength, (Decay Associated Spectra/DAS), were used to study the presence of FRET.

The developmental shift of chloride ions in neurons is important in both neurobiological as well as biophysical aspects. It is an essential feature to maintain equilibrium between excitation and inhibition in the developing brain. Also, the biophysical properties of the fluorescent probes are significantly affected due to this shift. A ratiometric chloride sensor Clomeleon, consisting of CFP (Cyan Fluorescent Protein) and a chloride sensitive variant of YFP (Yellow Fluorescent Protein) called Topaz, was used for studying the changes in intracellular chloride concentrations during neuronal development. A multi-wavelength approach with simultaneous detection and analysis of donor and acceptor probes was employed, with which a discrimination of energy transfer from other excited state reactions was possible along development of living hippocampal neurons. Clomeleon was used as an optical indicator for monitoring the intracellular chloride concentrations in living cells by steady-state and time-resolved spectroscopy. A direct correlation of FRET in Clomeleon with the overall development of individual neurons as well as at different subcellular compartments was also possible. The results helped to arrive at a kinetic model for the mechanism when competitive quenching effects as well as energy transfer simultaneously occur in the same molecule.

A principal candidate for investigation was the presynaptic protein Bassoon, a major scaffolding component of the CAZ (Cytomatrix at the Active Zone). Currently it is believed that prefabricated complexes comprising of presynaptic scaffolding proteins including Bassoon are assembled at the trans-Golgi network and are transported via dense-core vesicles to the presynapses. Using immunofluorescence techniques we could show that a central fragment of Bassoon, which contains essential signals for the recruitment of Bassoon to the presynapse, can simultaneously recruit CtBP1 and CAST to the same molecular complexes. Time-lapse studies indicated a co-transport of these proteins along neuronal axons and growth cones to possible synapses. In order to address a Bassoon-dependent recruitment of CtBP1 to different subcellular compartments, the studies were extended to observe a direct physical association of these proteins using a combination of FRET and FLIM in COS-7 cells and in the trans-Golgi network and synapses of living hippocampal neurons. The fluorescence properties of the donor probe were observed to be significantly affected depending on the property of the protein component to which it was fused and the environment in which it was expressed. Even in presence of high challenges posed for FRET-FLIM studies due to the varying intracellular ionic concentrations in neurons, our modified approaches in combination with immunocytochemistry made it possible to address the questions of interest.

Thus a deep investigation to address the changes in intracellular chloride along neuronal development and their photophysical effects on fluorescence, as well as interactions of proteins involved in synaptogenesis was done, which included the construction of a highly complex microscopic system as well as characterisation of the biophysical and biochemical properties of the proteins involved by microscopic, spectroscopic, biochemical, molecular biological and computational techniques.

1 PROLOGUE

1.1 THE NERVOUS SYSTEM

The nervous system regulates all aspects of bodily functions and is staggering in its complexity. The brain is probably the most intricate structure in the known universe; complex enough to coordinate the fingers of a concert pianist or to create a three-dimensional landscape from light that falls on a two-dimensional retina. For centuries, scientists and philosophers have been fascinated by the brain, but until recently they viewed the brain as nearly incomprehensible. Now, however, the brain is beginning to relinquish its secrets. Scientists have learned more about the brain in the last 10 years than in all previous centuries because of the accelerating pace of research in neurological and behavioral science and the development of new research techniques. In order to reveal active processes at the molecular level and to dissect key components of molecular pathways, biochemical studies in combination with modern imaging techniques provide a foundation for the elucidation of dynamic molecular mechanisms. Förster's Resonance Energy Transfer (FRET) and Fluorescence Lifetime Imaging Microscopy (FLIM) provide promising possibilities for a deeper understanding in this arena at high spatial and temporal resolution.

1.1.1 Neuronal differentiation and development of neuronal connectivity

The neuron is the major functional unit of the nervous system. Although the morphology of various types of neurons differs in some respects, they all contain four distinct regions with differing functions: the cell body, the dendrites, the axon, and the axon terminals. The cell body contains the nucleus and is the major site of synthesis of virtually all neuronal proteins and membranes. Growth and maintenance of neuronal processes require the timely, efficient delivery of material to axonal and dendritic domains (Hammerschlag et al., 1994). These proteins are assembled into membraneous vesicles and are transported along microtubules down the processes to the terminals by a process called anterograde transport, where they are inserted into the required organelles. Fast anterograde transport in mammals ranges from 3 to 5 μm/sec (Brady, 1991, 1992). Axonal microtubules are also the tracks along which damaged membranes and organelles move toward the cell body by retrograde transport.

Early in development, neurons are generated from dividing progenitor cells. Cell division stops soon after, and long extensions of axons grow out of the neurons in specific directions with growth cones at their tips. When these axons reach their targets, they form

characteristic terminal branches. Dendrites which extend out from the cell body are specialised to receive signals from the axon termini of other neurons and thus form contacts, so that they can pass messages on to the brain. Eventually, the growth cones develop into bulbous enlargements that possess a rudimentary capacity for spontaneous and evoked release of neurotransmitters.With time (hours to days), these structures differentiate into typical presynaptic terminals and gradually acquire mature functional characteristics (Sanes and Lichtman, 1999). Axons are specialised for the conduction of a particular type of electric impulse called an action potential, which is a series of sudden changes in the voltage or equivalently the electric potential across the plasma membrane (Lodish et al., 2000). A neuron in the resting state possesses a membrane potential of approximately -60 mV. At the peak of an action potential the membrane potential can be as much as +50 mV, a net change of ~110 mV. This depolarisation of the membrane is followed by a rapid repolarisation, returning the membrane potential to the resting value (Lodish et al., 2000).

1.1.2 Developmental shift of intracellular chloride in neurons

Anions are distributed differentially across the cell membrane. The main anions of the intracellular fluid are organic molecules, such as negatively charged amino acids, proteins and nucleic acids, whereas chloride is the principal anion in the extracellular fluid. Under physiological conditions of the adult CNS (central nervous system), the concentration gradient for chloride across the plasma membrane is such that there will be an influx of chloride when chloride-permeable channels such as GABA (γ-aminobutyric acid) receptors are open (Ben-Ari, 2002). However, the direction and magnitude of ion diffusion will be determined by both the concentration gradient and the membrane potential. In young neurons, however, GABA was found to be excitatory; the activation of GABA synapses producing a depolarisation (Ben-Ari, 2002). In these neurons, unlike those of adults, the reversal potential for chloride (electrochemical equilibrium potential-E_{Cl}) was at a more depolarised level than the resting membrane potential, indicating that intracellular concentration of chloride was high in developing neurons (Ben-Ari et al., 1989). This was in contrast to the inhibitory nature of GABA in mature neurons, where intracellular chloride concentrations were low; the activation of GABA synapses producing its characteristic hyperpolarisation (Ben-Ari, 2002). Several observations indicate that the key player in the developmental switch from GABA mediated excitation to inhibition is the K^+–Cl^--coupled co-transporter KCC2, whose expression predominates in mature neurons leading to a negative shift in the reversal potential for chloride ions (Ganguly et al., 2001; Rivera et al., 1999). Different studies indicate a simultaneous change in GABA, E_{Cl} and KCC2 activity in rodent hippocampal neurons

(Ganguly et al., 2001). Thus the activation of GABA receptors generates an efflux of chloride and a resulting excitation in immature neurons, in contrast to an influx of chloride and inhibition in adult neurons. An important feature of chloride gradients is that even small changes in its concentration can have profound consequences. In the immature brain where GABA is excitatory, GABA-releasing synapses are formed before glutamatergic contacts in a wide range of species and structures (Ben-Ari, 2002). This shift in the nature of GABA from excitatory to inhibitory due to the switch in intracellular chloride concentrations is especially important in maintaining the equilibrium between excitation and inhibition to avoid pathological consequences.

1.2 THE SYNAPSE

The human brain - the control centre that stores, computes, integrates and transmits information - contains about 10^{12} neurons, each forming as many as thousand connections with other neurons. Millions of specialised neurons sense features of both the external and and internal environments and transmit this information to the brain for processing and storage. Each neuron uses biochemical reactions to receive, process and transmit information. Synapses are specialised contact sites that enable neurons to form connections between each other in order to transmit and process neural information (Shepherd, 1998). Synaptic organisation is thus concerned with the principles by which neurons form circuits that mediate the specific functional operations of different brain regions.
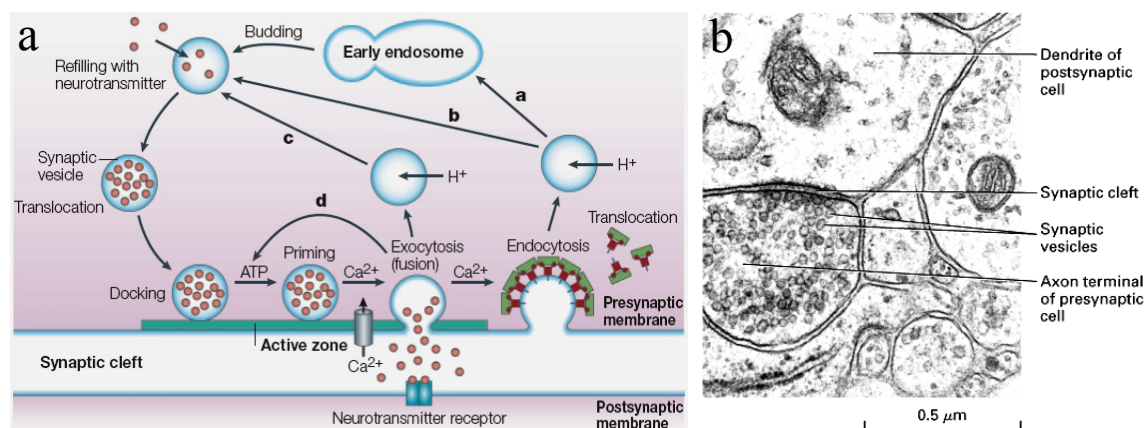
Fig. 1.1 *A chemical synapse a) A narrow region - the synaptic cleft - separates the plasma membranes of the presynaptic and postsynaptic cells. Arrival of action potential at the presynaptic terminal leads to Ca^{2+} influx, in response to which the primed synaptic vesicles undergo exocytosis and release neurotransmitters (red circles). They diffuse across the synaptic cleft and bind to specific receptors on the plasma membrane of the postsynaptic cell. b) Electron micrograph shows a dendrite synapsing with an axon terminal filled with synaptic vesicles. In the synaptic region, the plasma membrane of the presynaptic cell is specialised for vesicle exocytosis; synaptic vesicles containing neurotransmitters are clustered in these regions. The opposing membrane of the postsynaptic cell contains receptors for the neurotransmitters. a) Taken from Gundelfinger et al., 2003, Part (b) from C. Raine et al., eds., 1981, Basic Neurochemistry, 3rd ed., Little, Brown, p.32.*

Structurally, synapses are characterised by their asymmetric organisation with a presynaptic nerve terminal (bouton) that contains synaptic vesicles, a synaptic cleft, and a postsynaptic neurotransmitter reception apparatus, the postsynaptic density (PSD) (Fig. 1.1, (Gundelfinger and tom Dieck, 2000)). The mechanism for the action of a synapse involves a series of steps. These include (1) depolarisation of the presynaptic membrane, (2) influx of Ca^{2+} ions into the presynaptic terminal, (3) fusion of primed synaptic vesicles with the plasma membrane, (4) quantal release of a packet of neurotransmitter molecules, (5) diffusion of the transmitter molecules across the narrow synaptic cleft separating the presynaptic and postsynaptic membranes and (6) action of the transmitter molecules on receptor molecules in the postsynaptic membrane leading to different signalling pathways (Shepherd, 1998). Thus in chemical synapses, signal transduction is achieved by converting the electrical signal into a chemical signal that diffuses between cells. This signal conversion occurs at highly specialised sites of the presynaptic nerve terminal called active zones (Zhai and Bellen, 2004).

The term "active zone" was coined in 1970 by Couteaux and Pecot-Dechavassine (Couteaux and Pecot-Dechavassine, 1970) during their ultrastructural studies of partially contracted frog muscles, in which they observed that profiles of open synaptic vesicles occurred immediately adjacent to the presynaptic dense bands, and consequently they designated these dense bands "les zones actives." Subsequently, similar observations were made in other types of synapses. Ultrastructural studies of synapses have revealed that the presynaptic active zone is closely and precisely aligned with the PSD, and that the plasma membrane on both sites of the synaptic cleft appears as electron-dense structures suggesting their proteinaceous nature (Gundelfinger and tom Dieck, 2000; Zhai and Bellen, 2004). The similarity in structural organisations of active zones in different types of synapses found in a variety of organisms suggests that all active zones are organised according to the same pattern.

1.3 MOLECULAR ORGANISATION OF THE CAZ

A key signature of active zones is a dense meshwork of cytoskeletal filaments originating at the presynaptic plasma membrane and extending into the SV domain (Fig. 1.2, (Burns and Augustine, 1995; Landis et al., 1988)). This meshwork, termed cytomatrix at the active zone (CAZ) or presynaptic particle web, may serve pivotal synaptic functions including anchoring and mobilisation of SVs and spatial restriction of SV exocytosis to and assembling presynaptic molecules at the active zone (Dresbach et al., 2001; Garner et al., 2000; Phillips et

al., 2001; Zamorano and Garner, 2001). A variety of proteins has been identified that are associated with the CAZ, most of which are not restricted to active zones but can also be found in other compartments of the cell, including proteins involved in synaptic vesicle fusion, cytoskeletal proteins, scaffolding proteins, voltage gated calcium channels, and cell adhesion molecules (Dresbach et al., 2001; Gundelfinger and tom Dieck, 2000; Ziv and Garner, 2004). So far, five CAZ-enriched protein families have been identified and functionally analysed: UNC13/Munc13 proteins, RIMs (Rab3-interacting molecule), Bassoon and Piccolo/Aczonin, ELKS (ERC/CAST), and Liprins-α. Through physical interactions, these proteins form a scaffold at the active zone and play a role in organising the release and retrieval of synaptic vesicles and in regulating changes in release during short-term and long-term forms of synaptic plasticity (Fejtova and Gundelfinger, 2006; Schoch and Gundelfinger, 2006).
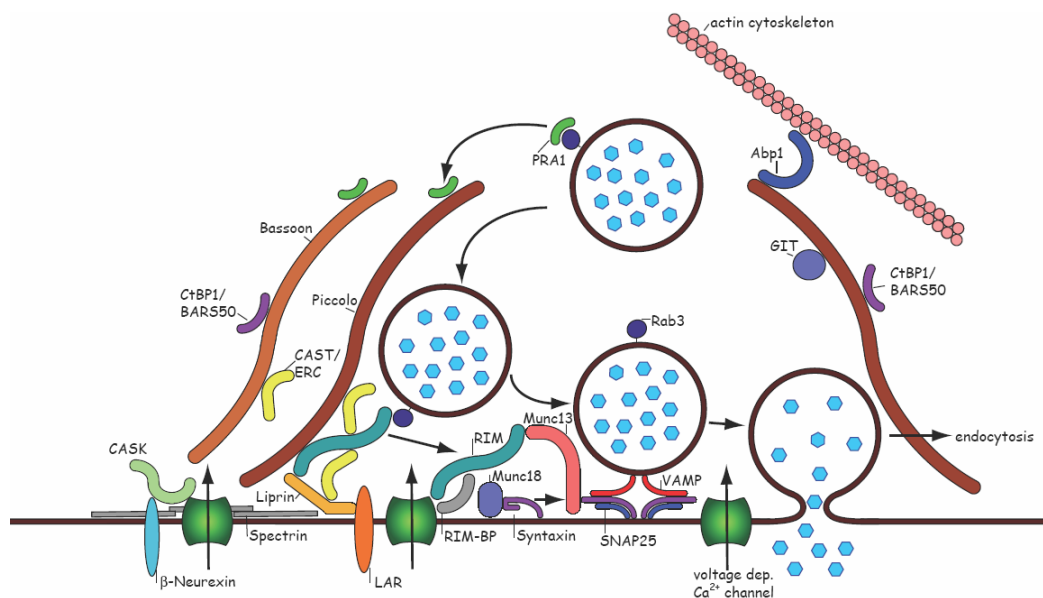
Fig. 1.2 *Molecular organisation of the CAZ. The CAZ-specific proteins RIMs, Munc13s, Bassoon, Piccolo and CAST/ERC are thought to localise and organise membrane trafficking events of the synaptic vesicle cycle and connect it to the active zone membrane proteins including voltage-gated Ca^{2+} channels and cell adhesion molecules such as the neurexins. Components that are not CAZ exclusive include Ca^{2+}/calmodulin kinase domain-containing membrane-associated guanylate kinase CASK, the transcriptional co-repressor CtBP1/BARS50, the RIM-binding proteins (RIMBP), the prenylated Rab3 acceptor protein PRA1, the ARF-GTPase-activating protein GIT, the receptor tyrosine phosphatase LAR and its interacting protein Liprin, components of the SNARE complex and its control elements (e.g. Munc18). The picture was taken from the website of IfN (http://www.ifn-magdeburg.de/en/departments/neurochemistry_and_molecular_biology) and from Fejtova and Gundelfinger, 2006. Courtesy: Dr. Anna Fejtova, ifN.*

1.3.1 Piccolo and Bassoon

Bassoon (tom Dieck et al., 1998) and Piccolo/Aczonin (Cases-Langhoff et al., 1996; Fenster et al., 2000; Wang et al., 1999) are structurally related and are the largest active zone-specific proteins identified so far (420 and 530 kDa). In contrast to RIM, Munc13 and ELKS, Piccolo and Bassoon are not evolutionary conserved in worms and flies, but are present in all

vertebrates. Piccolo and Bassoon share 10 regions of particular sequence similarity called Piccolo Bassoon homology domains (PBH, Fig. 1.3, (Schoch and Gundelfinger, 2006)) including two N-terminal zinc finger domains that show a limited degree of homology to the zinc fingers of α-RIMs and Rabphilin and three coiled-coil regions (CC) in the central region of each protein (Fenster et al., 2000; tom Dieck et al., 1998; Wang et al., 1999; Winter et al., 1999). In addition, the Piccolo C-terminal region is composed of a unique PDZ-domain and two C2-domains (C2A and C2B), which are structurally related to those in RIMs, and the N-terminus contains a proline-rich Q-domain. Bassoon has been shown to be post-translationally modified by N-terminal myristoylation (Dresbach et al., 2003). Based on sequence similarity considerations, Piccolo might also be acylated at its N-terminus. The N-terminal 609 amino acids of Bassoon are targeted to the Golgi apparatus and to synaptic vesicle clusters, but are not required for either trafficking step. By contrast, a central region of Bassoon is essential for its anchoring within the CAZ and for synaptic transmission at a certain set of synapses (Altrock et al., 2003; Dresbach et al., 2003). Different studies suggest an important role for Bassoon in the assembly and functioning of various types of synapses (Dick et al., 2003; Khimich et al., 2005).
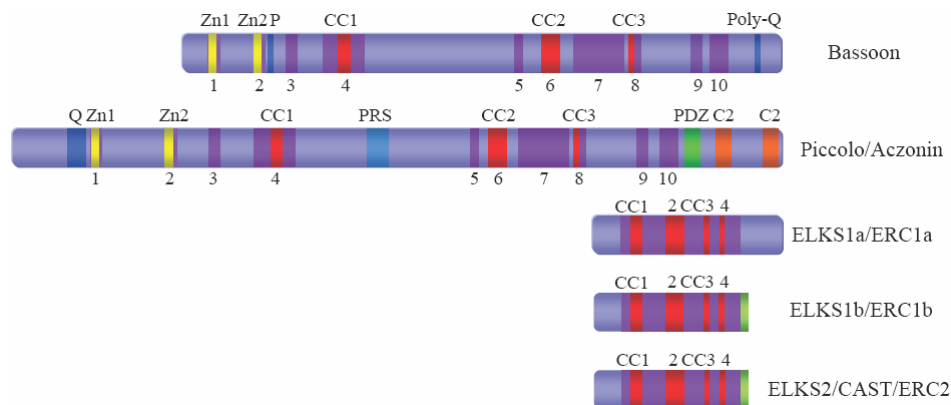
Fig. 1.3 Domain structure of CAZ protein families. Bassoon and Piccolo are structurally related proteins composed of two zinc finger domains (Zn1, Zn2), three coiled-coil domains (CC), several proline-rich sequences (Q), and 10 regions of homology called Piccolo Bassoon homology domains (PBH1–10). ELKS are composed of three coiled-coil (CC) domains and an isoform-specific C-terminus, which in case of ELKS1b and ELKS2 contains the RIM-PDZ-binding motif.

Bassoon and Piccolo are present at both excitatory and inhibitory synapses (Cases-Langhoff et al., 1996; Fenster et al., 2000; Richter et al., 1999; tom Dieck et al., 1998; Wang et al., 1999). Both proteins are tightly anchored to the subsynaptic cytoskeleton as judged by their resistance to detergent extraction from synaptosomal fractions (Cases-Langhoff et al., 1996; tom Dieck et al., 1998). Long regions of Bassoon and Piccolo share features of extended cytoskeletal proteins and it is possible that they span the entire CAZ extending from the presynaptic plasma membrane deeply into the presynaptic space (Dresbach et al., 2001). Both Piccolo and Bassoon interact through their third CC domain with members of the ELKS

protein family (Takao-Rikitsu et al., 2004) and with the two members of the CtBP (C-terminal binding protein/connected to Bassoon and Piccolo) protein family, namely CtBP1 and CtBP2 (tom Dieck et al., 2005). Their multidomain structure and enormous size suggest that these proteins can act as major scaffolding proteins of the CAZ, i.e. to spatially organise elements of the active zone including voltage-gated calcium channels and the SV endo- and exocytotic machinery (Dresbach et al., 2001). They are among the earliest proteins to be incorporated into nascent synapses, consistent with a role in active zone assembly (Friedman et al., 2000; Zhai et al., 2000; Zhai et al., 2001).

In differentiating neurons, Piccolo and Bassoon exhibit fine punctuate distributions and become progressively concentrated in axons (Zhai et al., 2000; Zhai et al., 2001). Using electron microscopy (EM), Piccolo and Bassoon have been found to be associated with a novel class of 80 nm diameter dense-core vesicles referred to as Piccolo-Bassoon transport vesicles (PTVs) that are intimately associated with microtubules in axons and axonal growth cones (Zhai et al., 2001). These vesicles were deficient of the characteristic synaptic vesicle molecules like synaptophysin and Vamp2/synaptobrevin II. Intriguingly, additional active zone molecules genetically and functionally coupled to synaptic vesicle exocytosis including Syntaxin, SNAP25, and N-cadherin (Shapira et al., 2003) as well as Liprin-α (Kim et al., 2003) and ERC (Ohtsuka et al., 2002), implicated in linking together components of the active zone cytoskeletal matrix, were found on these vesicles. Time-lapse studies have shown that functional presynaptic sites can form rapidly (in <30 min) after initial axo–dendritic contact (Friedman et al., 2000). As both Piccolo and Bassoon clusters were found at nascent synapses as soon as these displayed a capacity for activity-dependent recycling of SVs (Friedman et al., 2000; Zhai et al., 2001), it was suggested that PTVs may be 'active zone precursor vesicles' that upon fusion with the presynaptic plasma membrane lead to the rapid formation of new active zones (Ziv and Garner, 2001, 2004) or proto-terminals (Roos and Kelly, 2000). Quantitative immunocytochemical analysis indicated that the Bassoon, Piccolo and Rim content of presynaptic boutons could be accounted for by their recruitment from integer multiples of the protein contents of PTVs, indicating that presynaptic sites might be assembled in a unitary fashion from small numbers of precursor particles (Shapira et al., 2003). Time-lapse imaging of PTVs labelled with GFP-tagged variants of Bassoon revealed that they are transported rapidly along axons, and that the formation of new functional synaptic vesicle release sites is preceded by the recruitment of 2–5 PTVs to these sites (Bresler et al., 2004; Shapira et al., 2003).

Bassoon and Piccolo were observed to be colocalised with the trans-Golgi network in cultured neurons (Dresbach et al., 2006). Impairing vesicle exit from the Golgi complex, either using brefeldin A, recombinant proteins, or a low temperature block, prevented transport of Bassoon out of the soma. Thus, during synaptogenesis the delivery of Bassoon and Piccolo to nascent synapses depended on an intact Golgi apparatus (Dresbach et al., 2006). Deleting a newly identified Golgi-binding region of Bassoon impaired subcellular targeting of recombinant Bassoon (Dresbach et al., 2006). Overexpressing this region to specifically block Golgi binding of the endogenous protein reduced the concentration of Bassoon at synapses (Dresbach et al., 2006). These results indicated that transport via Golgi-derived vesicles is essential for delivery of cytomatrix proteins to the synapse. Together with the previous reports, the findings suggested that active zone and CAZ molecules assemble into a complex at the Golgi apparatus and are deposited as preformed complexes at nascent synapses via PTVs (Fig. 1.4, (Fejtova and Gundelfinger, 2006; Garner et al., 2002; Ziv and Garner, 2004).
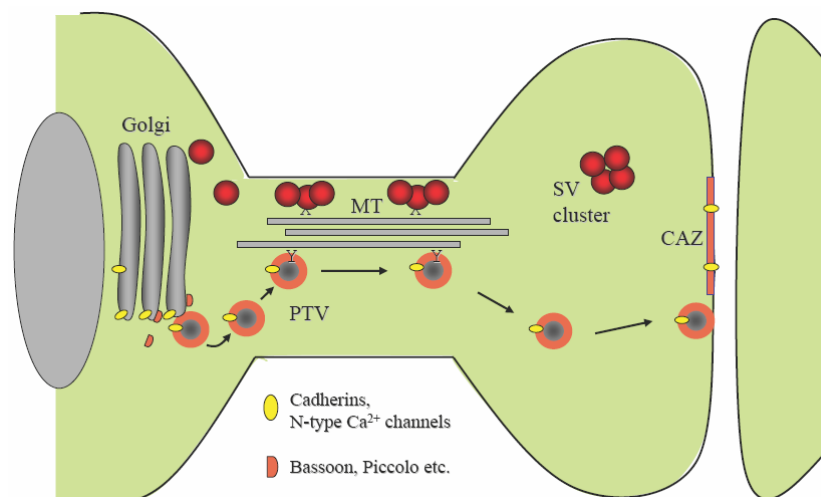
Fig. 1.4 The Active Zone Transport Vesicle Hypothesis: PTVs are thought to bud from the trans-Golgi-Complex. Bassoon and Piccolo are packaged onto the cytoplasmic surface of PTVs already at this site, most likely at a sub-compartment of the trans-Golgi-network, and this event seems obligatory for presynaptic targeting of these proteins. At the same site, PTVs may receive the entire complement of proteins. PTVs are supposed to travel along the axon via microtubule-based transport and are directed to nascent active zones by unknown signalling mechanisms. Fusion of PTVs with the axonal plasma membrane results in formation of an active zone. The topology of membrane fusion predicts that the CAZ proteins traveling on PTVs become located immediately underneath the plasma membrane, their contents are released, and transmembrane proteins become incorporated into the plasma membrane. SV precursors are also generated at the Golgi complex (left) and move along the axon along microtubules using independent pathways. (Adapted from Dresbach, Altrock, Gundelfinger, Neuroforum 03/2003).

1.3.2 ELKS/CAST/ERC proteins

ELKS/CAST/ERC proteins whose name arises from their high content in the amino acids glutamate (E), leucine (L), lysine (K), and serine (S), are the most recent proteins to be

identified that are enriched at the active zone. Mammals contain two inordinately large ELKS genes, ELKS1 and ELKS2. The amino acid sequences of ELKS1 (synonymous with ERC1/CAST2) and ELKS2 (CAST/ERC2) exhibit a high degree of homology except for short subtype-specific alternatively spliced regions (Fig. 1.3, (Wang et al., 2002)). Alternative splicing of the ELKS1 C-terminus produces two isoforms, referred to as ELKS1a and ELKS1b, with diverging tissue distributions and biochemical properties (Deguchi-Tawarada et al., 2004; Ohtsuka et al., 2002; Wang et al., 2002). The expression of ELKS1b and ELKS2 proteins is restricted to the brain in contrast to the ubiquitous expression of ELKS1a. ELKS1b and ELKS2 are 120-kDa proteins that are composed of four coiled-coil (CC) domains and a C-terminal-consensus-binding motif for binding to PDZ domains (Fig. 1.3). ELKS binds through its CC regions to the multidomain proteins Liprin-α (Ko et al., 2003) and to Piccolo/Aczonin and Bassoon (Takao-Rikitsu et al., 2004). Interference with ELKS binding to RIM and Bassoon has been shown to diminish synaptic transmission in cultured neurons (Takao-Rikitsu et al., 2004).

1.3.3 CtBP family of proteins

CtBPs belong to the group of proteins which are restricted not only to the CAZ, but are present at other intracellular compartments as well. CtBP1 and CtBP2 were first described as nuclear regulators of gene expression interacting with numerous transcription factors (Furusawa et al., 1999). Interestingly, an isoform of CtBP2 that is transcribed from a specific promoter has been identified as a protein called RIBEYE and is thought to be an exclusive structural component of synaptic ribbons, both in retinal photoreceptor cells (Schmitz et al., 2000) and in inner ear hair cells (Khimich et al., 2005). CtBP/BARS (an isoform of CtBP1 also named CtBP3 or BARS-50, i.e. brefeldin A-ADP-ribosylation substrate of 50 kDa) has been reported to be involved in dynamin-independent vesicle fission from the trans-Golgi network and to be a substrate for brefeldin A-ADP-ribosylation (Bonazzi et al., 2005; Hidalgo Carcedo et al., 2004). A recent study has also described a synaptic localisation of CtBP/BARS, where it might be involved in presynaptic membrane trafficking processes of the synaptic vesicle cycle along with Bassoon (tom Dieck et al., 2005).

1.4 AIMS OF THE STUDY

The present work is broadly classified into two parts. The first part deals with how a new microscopic system including wide-field non-scanning detectors based on Time and Space Correlated Single Photon Counting (TSCSPC) was developed, to study interactions

within living cells at high spatial and temporal resolution utilising a combination of FRET and FLIM techniques. The second part demonstrates how the system was successfully used for addressing different biological questions, including investigation of synaptic scaffolding proteins. The results have been divided into two sections.

1.4.1 Studying intracellular chloride changes during neuronal development

In order to address interactions of proteins involved in neuronal synaptic scaffolding machinery using FRET-FLIM, it was essential to have a clear understanding of the photophysics of the fluorescent probes to discriminate energy transfer from other photophysical processes. Neuronal development is characterised by changes in intracellular ionic concentrations which affects the biophysical properties of fluorescent molecules. Concurrently, this ionic shift is an essential feature to maintain equilibrium between excitation and inhibition in the developing brain. Chloride is supposed to be the main mediator of this shift. Thus, the studies in the changes of intracellular chloride concentrations during neuronal development were important in both biophysical as well as neurobiological aspects. Making use of the high anionic sensitivity of YFP (Griesbeck et al., 2001), a novel optical indicator called 'Clomeleon' was developed for studying the intracellular chloride concentrations (Kuner and Augustine, 2000). In Clomeleon, a chloride sensitive variant of YFP called Topaz (Ormo et al., 1996) was linked with a relatively chloride insensitive CFP using a 24 amino acid linker to form a ratiometric chloride indicator. Clomeleon was used to study the changes in intracellular chloride concentrations during neuronal development.

The major challenges addressed in this work were *1)* Discrimination of FRET from other excited state reactions along neuronal development. *2)* Investigation of the photophysics of Clomeleon at picosecond time scale. *3)* To ensure the suitability of Clomeleon as a ratiometric and lifetime indicator for chloride along development of living hippocampal neurons. The simultaneous study of the photophysical properties of Clomeleon, the calcium indicator Cameleon and ECFP with neuronal development were used to postulate a kinetic model for the mechanism when competitive quenching effects as well as energy transfer occur in the same molecule.

1.4.2 Studying interactions of synaptic proteins in vivo

Active zone proteins are believed to form a highly interactive and dynamic protein complex at the site of synaptic vesicle exocytosis. However, little is known about the mechanisms of CAZ assembly and of targeting of cytomatrix proteins to active zones. In

particular, because Bassoon and Piccolo have little homology to any other known protein it is difficult to extract information on putative targeting signals from their primary structure.

Upon blockade of the Golgi exit in neurons or heterologous expression in non-neuronal cells, Bassoon forms protein clusters in the cell soma (Dresbach et al., 2006). Currently, it is not clear whether these macromolecular complexes are functional and can recruit binding partners of Bassoon. The CAZ-associated structural protein CAST/ELKS2 and the C-terminal binding protein 1/ brefeldin A-ADP ribosylated substrate (CtBP1/BARS) have been suggested to directly interact with Bassoon-containing complexes, though the clear functional relevance of these interactions is yet to be addressed. It has been shown biochemically that a central fragment of Bassoon of approximately 1500 amino acids (aa), namely Bsn1692-3263 which is recruited to the presynapse when expressed in primary neuronal cultures, can interact with CtBP1 (tom Dieck et al., 2005) while it also harbours the potential binding site for CAST/ELKS2 (Takao-Rikitsu et al., 2004). To date, a direct confirmation of this interaction under real cell conditions has never been done.

The ionic changes during neuronal development significantly affect the properties of fluorescent probes. In addition, the presence of endogenous interaction partners notably reduces the possibility for observing FRET between the fluorescent tagged proteins. Therefore, heterologous expression in COS-7 cells was initially used to assess the formation of macromolecular complexes involving CtBP1 and CAST recruited by Bassoon. A direct physical association of these proteins was studied using a combination of FRET and FLIM in living cells with fusion constructs of stock shifted GFP-variants, namely Cerulean and Citrine.

In neurons, Bassoon and CtBP1 are colocalised in synapses (tom Dieck et al., 2005), though a direct association between them in living cells has not yet been proven. The suggested model of a recruitment of the CAZ associated proteins, Bassoon, CtBP1 and CAST from the Golgi apparatus to presynapses as a preformed complex was addressed using a combination of time-lapse imaging, FRET and FLIM followed by immunocytochemistry to recognise different subcellular compartments. A simultaneous study of donor and acceptor fluorescence decays along with comparison of their DAS was necessary to discriminate energy transfer from cellular influences. These studies would be a prerequisite in understanding the different cell signalling pathways in living neurons.

Thus a combination of spectroscopic, molecular biological, biochemical, immunocytochemical and computational techniques was adopted to directly address the different biological questions of interest, which will be discussed in the subsequent chapters.

2 THEORY AND INSTRUMENTATION

2.1 THEORY

2.1.1 Fluorescence

Luminescence is the emission of light from any substance and occurs from electronically excited states. Luminescence is formally divided into two categories, fluorescence and phosphorescence, depending on the nature of the excited state. In excited singlet states, the electron in the excited orbital is paired (of opposite sign) to the second electron in the ground-state orbital. Consequently, return to the ground state is spin-allowed and occurs rapidly by emission of a photon. This is fluorescence, whose emission rates are typically in the range of nanoseconds. Phosphorescence is the emission of light from triplet excited states, in which the electron in the excited orbital has the same spin orientation as the ground-state electron. Transitions to the ground state are forbidden and the emission rates are slow, so that phosphorescence lifetimes are typically milliseconds to seconds.
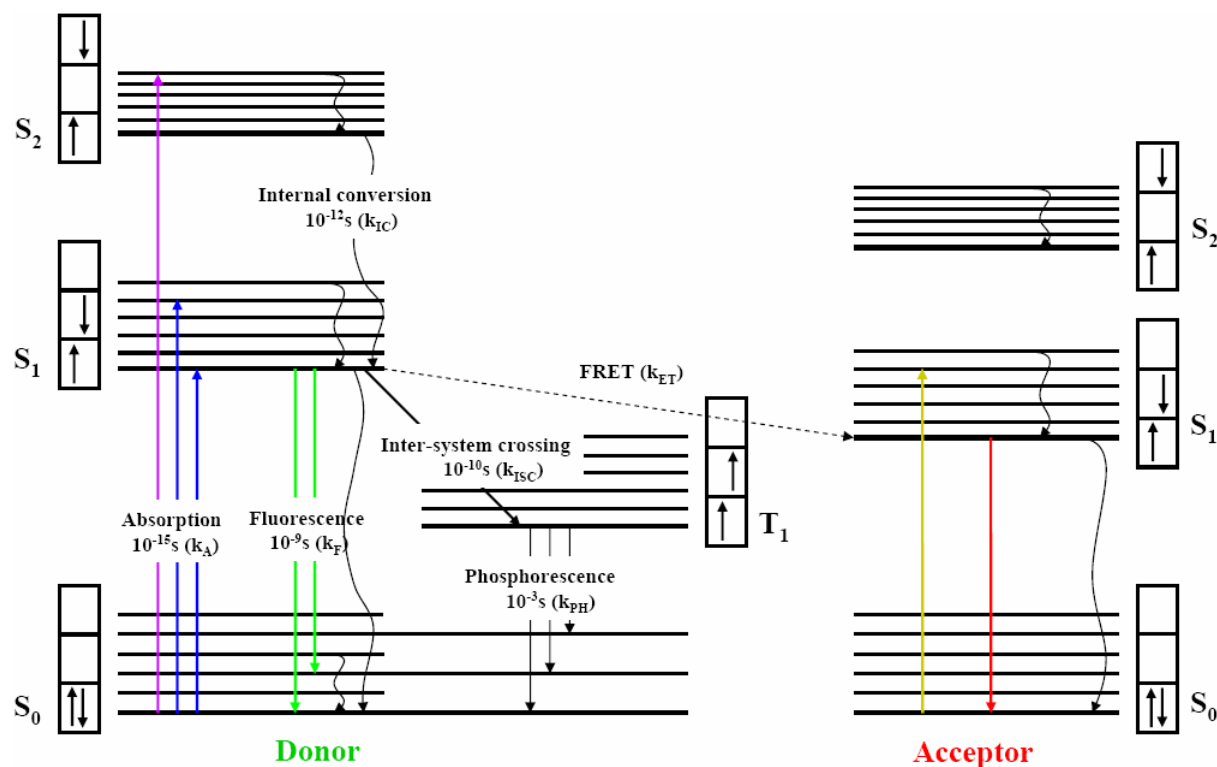
Fig. 2.1 *Jablonski Diagram (energy level diagram). The different deactivation pathways through which an excited molecule can return to its ground-state, are labeled with the corresponding rate constants: Fluorescence k_F, Förster's energy transfer k_{ET}, internal conversion k_{IC}, intersystem crossing k_{ISC} and phosphorescence k_{PH}. The colours indicate the relative wavelengths of light absorbed or emitted during each process, violet being the shortest and red the longest.*

A typical Jablonski diagram is shown in Fig. 2.1. The singlet ground, first and second electronic states are depicted as S_0, S_1, and S_2, respectively. At each of these electronic energy levels, the fluorophores can exist in a number of vibrational energy levels. The transitions

between states are depicted as vertical lines to illustrate the instantaneous nature of light absorption. Transitions occur in about 10^{-15} s, a time too short for significant displacement of nuclei. This is the Franck-Condon principle. A fluorophore is usually excited to higher vibrational levels of either S_1 or S_2. These molecules usually relax back rapidly to the lowest vibrational level of S_1. This process is called internal conversion and generally occurs in 10^{-12} s or less. Thus, internal conversion is generally complete prior to fluorescence emission. Hence, fluorescence emission generally results from a thermally equilibrated state, i.e. the lowest-energy vibrational state of S_1. This is Kasha's rule. The energy loss by internal conversion results in the emission to be lower in energy or to be red-shifted, which is also referred to as the Stokes shift. Molecules in the S_1 state can also undergo a spin conversion to the triplet state, T_1. Conversion of S_1 to T_1 is called intersystem crossing. Emission from T_1 results in phosphorescence.

Fluorescence measurements can be broadly classified into two types of measurements, steady-state and time-resolved. Steady–state measurements are performed with constant illumination and observation. Time-resolved measurements are used for measuring intensity decays. Because of the short time scale of fluorescence, measurement of time-resolved emission requires sophisticated optics and electronics. In spite of the experimental difficulties, time-resolved fluorescence is adopted because of the increased information available from the data, compared to stationary or steady-state measurements. Much of the molecular information available from fluorescence is lost during time-averaging process. Frequently, macromolecules can exist in more than a single conformation, and the decay time of a bound probe may depend on its conformation. The intensity decay could reveal two decay times and thus the presence of more than one conformational state. The steady-state intensity will only reveal an average intensity dependent on a weighted average of the two decay times.

2.1.2 Fluorescence Lifetime Imaging Microscopy (FLIM)

A typical example of time-resolved fluorescence measurement is fluorescence lifetime imaging. The fluorescence lifetime and quantum yield are the most important characteristics of a fluorophore. The fluorescence quantum yield is the ratio of the number of photons emitted to the number of photons absorbed. Radiative and non-radiative processes depopulate the excited state of a fluorophore. The fraction of fluorophores which decay through emission, and hence the quantum yield, is given by

$$Q = \frac{\Gamma}{\Gamma + k_{nr}} \qquad\qquad [1]$$

where Γ is the emissive rate of the fluorophore and k_{nr} is the rate of non-radiative decay to S_0. The lifetime of the excited state is defined by the average time the molecule spends in the excited state, prior to its return to the ground state. Thus the fluorescence lifetime gives information on the time available for the fluorophore to interact with or diffuse in its environment.

The fluorescence lifetime of a fluorophore is given by,

$$\tau = \frac{1}{\Gamma + k_{nr}} \qquad\qquad [2]$$

The lifetime of the fluorophore in the absence of non-radiative processes is called the intrinsic or natural lifetime and is given by

$$\tau_n = \frac{1}{\Gamma} \qquad\qquad [3]$$

where the radiative decay rate Γ can be calculated using

$$\Gamma \sim 2.88 \times 10^{-9} \eta^2 \frac{\int F(\bar{v}) d\bar{v}}{\int F(\bar{v}) d\bar{v} / \bar{v}^3} \int \frac{\varepsilon(\bar{v})}{\bar{v}} d\bar{v}$$

$$\Gamma \sim 2.88 \times 10^{-9} \eta^2 < \bar{v}^{-3} >^{-1} \int \frac{\varepsilon(\bar{v})}{\bar{v}} d\bar{v} \qquad\qquad [4]$$

where $F(\bar{v})$ is the emission spectrum plotted on the wavenumber (cm-1) scale, $\varepsilon(\bar{v})$ is the absorption spectrum and η is the refractive index of the medium. The integrals are calculated over the $S_0 \leftrightarrow S_1$ absorption and emission spectra.

Combining eqs. [1]- [3], the natural lifetime can be calculated from the measured lifetime (τ) and quantum yield as

$$\tau_n = \frac{\tau}{Q} \qquad\qquad [5]$$

Fluorescence lifetime imaging makes it possible to obtain information on the molecules while observing a living cell. The factors affecting the fluorescence lifetime include ion intensity, hydrophobic properties, oxygen concentration, molecular binding, and molecular interaction by energy transfer when two proteins approach each other. Lifetime is,

however, independent of dye concentration, photobleaching, light scattering and excitation light intensity. Therefore, fluorescence lifetime imaging allows us to perform accurate ion concentration measurement and Fluorescence Resonance Energy Transfer (FRET) analysis. FLIM can be performed either in the time domain or in the frequency domain.

2.1.2.1 Time-domain FLIM

In the time domain method, the sample is excited with a pulse of light whose pulse width is much shorter than the decay time (τ) of the sample. The time-dependent intensity is measured following the excitation pulse and the decay time τ is calculated from the slope of a plot of log I(t) versus t, or from the time at which the intensity decreases to 1/e of the value at t=0. When fluorophores are excited with an infinitely sharp (δ-function) pulse of light, this results in an initial population (n_0) of fluorophores in the excited state. The excited-state population decays with a rate $\Gamma + k_{nr}$ according to

$$\frac{dn(t)}{dt} = -(\Gamma + k_{nr})n(t) \qquad [6]$$

where $n(t)$ is the number of excited molecules at time t following excitation.

In a fluorescence experiment, we observe fluorescence intensity, which is proportional to $n(t)$. Integration of eq. [6] yields the time-dependent intensity $I(t)$ for a single exponential decay, which is given by

$$I(t) = I_0 \exp(-t/\tau) \qquad [7]$$

where I_0 is the intensity at time zero.

The lifetime τ is the inverse of the total decay rate: $\tau = (\Gamma + k_{nr})^{-1}$.

The average time $<t>$ obtained by averaging t over the intensity decay of the fluorophore is given by

$$<t> = \frac{\int_0^\infty t I(t)dt}{\int_0^\infty I(t)dt} = \frac{\int_0^\infty t \exp(-t/\tau)dt}{\int_0^\infty \exp(-t/\tau)dt} \qquad [8]$$

The denominator equals τ, whereas following integration by parts, the numerator equals to τ^2. Hence for a single-exponential decay, the average time a fluorophore remains in the excited state is equal to its lifetime.

$$< t >= \tau \tag{9}$$

In a multi-exponential model, the intensity is assumed to decay as the sum of individual single-exponential decays:

$$I(t) = \sum_{i=1}^{n} \alpha_i \exp(-t / \tau_i) \tag{10}$$

Lifetime is a statistical average since fluorophores emit randomly throughout the decay. This time distribution of emitted photons is the intensity decay.

2.1.2.2 Frequency-domain FLIM

The alternative method for measuring the decay time is in the frequency domain. In the frequency domain or phase-modulation method, the sample is excited with intensity-modulated light. The intensity of the incident light is varied at a high frequency, comparable to the reciprocal of the decay time τ. The fluorescence lifetime is calculated by measuring the phase shift of fluorescence and the reduction in its amplitude.

2.1.3 Förster's Resonance Energy transfer (FRET)

FRET is a quantum mechanical process involving the radiation-less transfer of energy from a donor fluorophore to an appropriately positioned acceptor fluorophore over a very limited distance, with subsequent fluorescence emission by the acceptor fluorophore. Energy transfer occurs without the appearance of a photon and is the result of long-range dipole-dipole interactions between the donor and the acceptor. Four conditions must be fulfilled for FRET to occur. First, the donor emission spectrum must significantly overlap (>70%) with the acceptor absorption spectrum. Second, the distance between the donor and acceptor fluorophores must fall within the range of 1 to 10 nm. Third, the donor emission dipole moment, the acceptor absorption dipole moment and their separation vectors must be in favourable mutual orientation. Further, the donor molecules should have high quantum yield. The rate of energy transfer depends upon all these factors. The distance at which FRET is 50% efficient, called the Förster distance, is typically in the range of 2-6 nm.

Several FRET microscopy techniques exist. They can be generally classified as time-resolved and intensity-based FRET.

2.1.3.1 Time-resolved FRET

Temporal resolution of the imaging modalities can be achieved by the technique of fluorescence lifetime imaging. This technique monitors the localised changes in probe fluorescence lifetime and provides an enormous advantage for imaging dynamic events within

the living cells. When combined with FRET, this approach provides direct evidence for the physical interactions between two or more proteins with very high spatial and temporal resolution.

The rate of energy transfer from a donor to an acceptor (k_T) is given by

$$k_T = \frac{1}{\tau_D}\left(\frac{R_0}{r}\right)^6 \qquad\qquad [13]$$

where τ_D is the decay time of the donor in the absence of acceptor, R_0 is the Förster distance and r is the donor-to-acceptor (D-A) distance. Hence, the rate of transfer is equal to the decay rate of the donor in the absence of acceptor ($1/\tau_D$) when the D-A distance (r) is equal to the Förster distance (R_0). When the D-A distance is equal to the Förster distance ($r=R_0$), then the transfer efficiency is 50%. At this distance ($r=R_0$), the donor emission would be decreased to one-half of its intensity in the absence of acceptor. The rate of FRET depends strongly on distance, being inversely proportional to r^6.

The theory of energy transfer is based on the concept of a fluorophore as an oscillating dipole, which can exchange energy with another dipole of similar frequency. In contrast to radiative energy transfer which is due to inner filter effects and involves emission and re-absorption of photons, non-radiative energy transfer contains a wealth of structural information concerning the donor-acceptor pair. Non-radiative energy transfer is effective over much longer distances compared to solvent relaxation, fluorescence quenching or anisotropy and the intervening solvent or macromolecules have little effects on the efficiency of energy transfer.

The rate of transfer for a donor and acceptor separated by a distance r is given by

$$k_T(r) = \frac{Q_D \kappa^2}{\tau_D r^6}\left(\frac{9000(\ln 10)}{128\pi^5 A \eta^4}\right)\int_0^\infty F_D(\lambda)\varepsilon_A(\lambda)\lambda^4 d\lambda \qquad\qquad [14]$$

where Q_D is the quantum yield of the donor in the absence of acceptor; η is the refractive index of the medium; A is Avogadro's number; τ_D is the lifetime of the donor in the absence of acceptor; $F_D(\lambda)$ is the corrected fluorescence intensity of the donor in the wavelength range λ to $\lambda + \Delta\lambda$, with the total intensity (area under the curve) normalised to unity; $\varepsilon_A(\lambda)$ is the extinction coefficient of the acceptor at λ, typically in units of $M^{-1}cm^{-1}$ and κ^2 is a factor describing the relative orientation in space of the transition dipoles of the donor and acceptor, which is 2/3 for dynamic random averaging of the donor and acceptor.

The overlap integral $J(\lambda)$ expresses the degree of spectral overlap between the donor emission and the acceptor absorption,

$$J(\lambda) = \int_0^\infty F_D(\lambda)\varepsilon_A(\lambda)\lambda^4 d\lambda = \frac{\int_0^\infty F_D(\lambda)\varepsilon_A(\lambda)\lambda^4 d\lambda}{\int_0^\infty F_D(\lambda)d\lambda} \qquad [15]$$

where $F_D(\lambda)$ is dimensionless.

At the Förster distance (R_0), one-half of the donor molecules decay by energy transfer, whereas the other-half decay by the usual radiative and non-radiative decays. Thus from eqs. [13] and [14] with $k_T(r) = \tau_D^{-1}$, we get

$$R_0^6 = \frac{9000(\ln 10)\kappa^2 Q_D}{128\pi^5 A\eta^4}\int_0^\infty F_D(\lambda)\varepsilon_A(\lambda)\lambda^4 d\lambda \qquad [16]$$

This allows the Förster distance to be calculated from the spectral properties of the donor and the acceptor and the donor quantum yield.

If the wavelength is expressed in nanometers, then $J(\lambda)$ is in units of M^{-1} cm^{-1} $(nm)^4$ and the Förster distance, in angstroms, is given by

$$R_0 = 0.211\left[\kappa^2\eta^{-4}Q_D J(\lambda)\right]^{1/6} \qquad [17]$$

Once the value of R_0 is known, the rate of energy transfer can be calculated using

$$k_T(r) = \frac{1}{\tau_D}\left(\frac{R_0}{r}\right)^6 \qquad [18]$$

The efficiency of energy transfer (E) is the fraction of photons absorbed by the donor that are transferred to the acceptor. This fraction is given by

$$E = \frac{k_T}{\tau_D^{-1} + k_T} \qquad [19]$$

which is the ratio of the transfer rate to the total decay rate of the donor. Eqs. [17]-[18] yields

$$E = \frac{R_0^6}{R_0^6 + r^6} \qquad [20]$$

The transfer efficiency is typically measured using the relative fluorescence intensity of the donor in the absence (F_D) and presence (F_{DA}) of acceptor. The transfer efficiency can also be calculated from the lifetimes under these respective conditions (τ_D and τ_{DA}):

$$E = 1 - \frac{\tau_{DA}}{\tau_D} \qquad [19]$$

$$E = 1 - \frac{F_{DA}}{F_D} \qquad [20]$$

The orientation factor κ^2 is given by

$$\kappa^2 = (\cos\theta_T - 3\cos\theta_D \cos\theta_A)^2 \qquad [21]$$

$$\kappa^2 = (\sin\theta_D \sin\theta_A \cos\phi - 2\cos\theta_D \cos\theta_A)^2 \qquad [22]$$

where θ_T is the angle between the emission transition dipole of the donor and the absorption transition dipole of the acceptor; θ_D and θ_{DA} are the angles between these dipoles and the vector joining the donor and the acceptor and φ is the angle between the planes. Depending upon the relative orientation of donor and acceptor, κ^2 can range from 0 to 4. For collinear and parallel transition dipoles, $\kappa^2 = 4$, and for parallel dipoles, $\kappa^2 = 1$. Since the sixth root of κ^2 is taken in calculating the distance, variation of κ^2 from 1 to 4 results in only a 26% change in r. With $\kappa^2 = 2/3$, as is usually assumed, the calculated distance can be in error by no more than 35%. This is the value for donors and acceptors that randomise by rotational diffusion prior to energy transfer.

2.1.3.2 Decay Associated Spectra (DAS)

From eq [10], the intensity decay in a multi-exponential model is given by

$$I(t) = \sum_{i=1}^{n} \alpha_i \exp(-t/\tau_i)$$

When involved in excited state reactions, this equation is altered. For a two state excited state reaction (Fig. 2.2), where F and R represent initially excited and reacted species, the decay rates can be written as $\gamma_F = \Gamma_F + k_1 + k_{nr}^F$ and $\gamma_R = \Gamma_R + k_2 + k_{nr}^R$ where Γ_F and Γ_R are the radiative decay rates and k_{nr}, the non-radiative decay rates. The rates of forward and reverse reactions are given by k_1 and k_2. For an irreversible reaction, $k_2 = 0$.
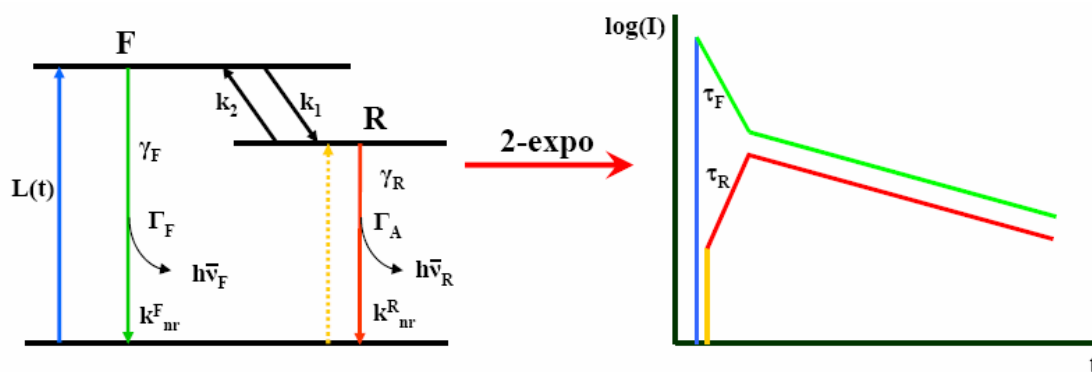
Fig. 2.2 *Jablonski diagram for a reversible excited state reaction. L(t) is the excitation function. The resulting lifetime plots from states F and R are shown on the right, where in presence of an excited state reaction, a resulting decay (green) and a corresponding rise (red) are observed, which deexcite with similar lifetimes after a certain time.*

Assuming that emission occurs only from the unreacted F state or reacted R state, the relative quantum yield of the F state I is given by the ratio of the emissive rate to the total rate of depopulation of the F state. Thus,

$$F_0 = \Gamma_F / \left(\Gamma_F + k_{nr}^F \right) \tag{23}$$

$$F = \Gamma_F / \left(\Gamma_F + k_{nr}^F + k_1 \right) \tag{24}$$

where F_0 and F are the fluorescence intensities observed in the absence and presence of the reaction, respectively. Division of eq. [24] by eq. [23] yields

$$\frac{F}{F_0} = \frac{1}{1 + k_1 \tau_{0F}} \quad \text{where } \tau_{0F} = \gamma_F^{-1} = \left(\Gamma_F + k_{nr}^F \right)^{-1} \text{ is the lifetime of the F state in the absence of}$$

the reaction.

The yield of the reaction product R is the fraction of F molecules which have reacted. This yield is given by

$$\frac{R}{R_0} = 1 - \frac{F}{F_0} = \frac{k_1 \tau_{0F}}{1 + k_1 \tau_{0F}} \quad \text{where } R \text{ and } R_0 \text{ are the intensities of the reacted species when the}$$

reaction is incomplete and complete, respectively. This model can be described by the following kinetic equations:

$$\frac{-d[F]}{dt} = \gamma_F [F] - k_2 [R] - L(t) \tag{25}$$

$$\frac{-d[R]}{dt} = \gamma_R [R] - k_1 [F] \tag{26}$$

where [F] and [R] are the concentrations of these states and $L(t)$ is the time profile of excitation.

Following δ-pulse excitation, the fluorescence decays of the F and R states are given by

$$I_F(t) = \alpha_1 \exp(-\gamma_1 t) + \alpha_2 \exp(-\gamma_2 t) \tag{27}$$

$$I_R(t) = \beta_1 \exp(-\gamma_1 t) + \beta_1 \exp(-\gamma_2 t) \tag{28}$$

where α_i and β_1 represent the pre-exponential factors. The values of $\gamma_1 = \tau_1^{-1}$ and $\gamma_2 = \tau_2^{-1}$ are given by

$$\gamma_1, \gamma_2 = \frac{1}{2} \left\{ (x + y) \pm \left[(y - x)^2 + 4 k_1 k_2 \right]^{1/2} \right\} \tag{29}$$

where $x = \Gamma_F + k_{nr}^F + k_1 = \gamma_F + k_1$ and $y = \Gamma_R + k_{nr}^R + k_2 = \gamma_R + k_2$

For a reversible two state reaction, both species display biexponential decay with the same decay times (Fig. 2.2). Also, if only the R state is observed, then the pre-exponential factors for the two lifetimes are expected to be equal and opposite (β_1 in eq. [28]). The negative pre-exponential factor results in a rise in intensity, which is characteristic of excited state reactions.

For many molecules that display excited state reactions, there is spectral overlap of the F and R states. The wavelength-dependent intensity decays in this case is given by

$$I(\lambda,t) = \alpha_1(\lambda)\exp(-t/\tau_1) + \alpha_2(\lambda)\exp(-t/\tau_2) \qquad\qquad [30]$$

where the same two decay times will be present at all wavelengths. In this case, global analysis can be performed with two wavelength-dependent lifetimes. As the observation wavelength is increased, an increasing fraction of the R state is observed. The $\alpha_i(\lambda)$ values shift from those characteristic of the F state (eq. [27]) to those characteristic of the R state (eq. [28]). On the long wavelength side of emission, a negative pre-exponential factor is expected unless the spectral shift is small so that the F and R states overlap at all wavelengths. In the time domain, the characteristics of an excited state reaction are a rise time in the decay and a negative pre-exponential factor in the multi-exponential analysis. The values of $\alpha_i(\lambda)$ plotted along the wavelength axis yields the Decay Associated Spectra (DAS), which show positive and negative amplitudes in presence of excited state reactions. The DAS do not correspond to the emission spectrum of either species. $I(\lambda,t)$ can be used to calculate the species associated spectra (SAS), which represent the spectra of each species.

If the reaction is irreversible, $k_2=0$. In this case, eq. [29] yies $\gamma_1=\gamma_F+k_1$ and $\gamma_2=\gamma_R$. Also, one of the pre-exponential factors becomes zero, yielding

$$I_F(t) = \alpha_1 \exp(-\gamma_1 t) \qquad\qquad [31]$$

$$I_R(t) = \beta_1 \exp(-\gamma_1 t) - \beta_1 \exp(-\gamma_2 t) \qquad\qquad [32]$$

Hence the decay of the initially excited state becomes a single exponential. The negative pre-exponential factor may be associated with either of the decay times.

Energy transfer between chemically distinct donors and acceptors is called hetero-transfer. FRET can also occur between chemically identical molecules. Such transfer, termed homo-transfer, typically occurs for fluorophores which display small Stoke's shifts and results in decrease in the anisotropy of fluorophores. This transfer is made possible by the "anti-Stokes" overlap of fluorescence with the absorption spectrum of the same fluorophore. In this case, though theoretically $k_1=k_2$; in real conditions $k2<<k1$, thereby resulting in an overall fluorescence decay for the molecules. No negative pre-exponential factors would be observed due to the small Stoke's shift.

2.1.3.3 Intensity-based FRET

Intensity-based approaches are based on the changes of the fluorescence intensity or brightness of the probes under different conditions. The results are dependent on the fluorophore concentrations and on the FRET efficiency. Fluorescence recovery after photo-bleaching (FRAP) is a popularly adopted method in this group, where the changes in the donor intensity is recorded before and after photo-bleaching of the acceptor. The FRET efficiency is calculated from the donor recovery.

Intensity-based FRET imaging microscopy suffers from various drawbacks, including autofluorescence, detector noise, optical noise, and photo-bleaching. In addition, spectral bleed through (SBT) or contributions of donor and acceptor fluorescence emission into the FRET channel is a major problem. Due to these effects, the observed FRET signal is higher than the actual signal. To correct for these problems, various methods of FRET data analysis for wide-field microscopy have been developed which also poses limitations of their own.

Though wide-field as well as confocal microscopy are used for studying FRET-FLIM, the former was adopted in our case to minimise photo-toxicity when imaging living cells. The standard laser lines used in confocal microscopes induces photo-bleaching as well as limited range of excitation. Therefore, non-scanning approaches using a tunable laser and ultra-sensitive detectors proved to be the best system for us to study the interactions in living cells by FRET using lifetime imaging.

2.1.4 FRET-FLIM: an optimal tool for monitoring interactions in living cells

A number of techniques have been developed so far to study the dynamic events taking place inside living cells. The complex organisation of the cells makes it probable that the molecular behaviour studied by artificial means and that in realistic conditions is not identical and therefore it is essential to study molecules in their natural environment (Hink et al., 2002). Making use of the current advances in fluorescence microscopy and development of variants of green fluorescent proteins (GFPs), FRET has become a powerful tool to localise and monitor ion binding as well as to map protein-protein interactions in living specimens (Day et al., 2001; Pollok and Heim, 1999). Förster distances are convenient for studies of biological macromolecules. These distances are comparable to the diameter of many proteins, the thickness of biological membranes and the distance between sites on multi-subunit proteins. Any phenomenon which affects the D-A distance will affect the transfer rate, allowing the phenomenon to be quantified. Energy transfer measurements have been used to estimate the distances between sites on macromolecules and the effects of conformational changes on these distances (dos Remedios and Moens, 1995; Wu and Brand, 1994). In this type of application, the extent of energy transfer between a fixed donor and acceptor is used to calculate the D-A distance and thus obtain structural information about the macromolecule. Such distance measurements have resulted in the description of FRET as a ''spectroscopic ruler'' (Stryer, 1978; Stryer and Haugland, 1967). Thus, in contrast to the in vitro methods which are useful to assess the potential of proteins for physical interactions, FRET allows direct access to these interactions within a macromolecular complex inside a living cell at a

resolution higher than conventional microscopy (Ballestrem and Geiger, 2005; Jares-Erijman and Jovin, 2003).

When measuring in living cells, one of the major challenges is to overcome the difficulty of the concentration dependence of the measured parameters, whose determination is practically impossible in living cells. FLIM monitors localised changes in the probe fluorescent lifetime which is independent of local fluorophore concentrations, but sensitive to environmental conditions such as pH and excited state reactions such as FRET or quenching properties (Bastiaens and Squire, 1999; Elangovan et al., 2002; Gadella et al., 1993; Lakowicz et al., 1992; Sanders et al., 1995). Thus a combination of these techniques in turn provides high spatial (nanometer) and temporal resolution (picosecond) in monitoring interactions within protein complexes in their natural environment.

The failure to detect FRET from a pair of labeled proteins may not always translate to the absence of interaction between them. Because the detection of FRET signal relies on the efficiency of FRET, it is important to optimise the efficiency by choosing a donor fluorophore that has a significant overlap with the acceptor absorption. Since FRET is most efficient with a stoichiometry favouring the interaction of proteins fused to the donor and acceptor fluorophores, similar concentrations of acceptor to donor molecules would be important. Intensity-based FRET measurements are limited by the accuracy of quantifying fluorescence intensity, which is more prone to artefacts at weaker energy transfer signals. To quantify lower intensities accurately, lifetime imaging of the donor and acceptor fluorophores offer significant improvement in sensitivity for determining the physical interactions between molecules in living cells.

Section 2.1 is modified from (Birks, 1970; Lakowicz, 1999; Van Der Meer et al., 1994).

2.2 INSTRUMENTATION

2.2.1 Time correlated single photon counting

TCSPC is a digital technique, counting photons which are time-correlated in relation to the excitation pulse. A pulsed light source, typically a laser or a flash lamp produces the excitation pulse which excites the sample. Each pulse is optically monitored by a high speed photodiode to produce a start signal which is used to trigger the voltage ramp of a time-to-amplitude converter (TAC). The voltage ramp is stopped when the first fluorescence photon from the sample is detected. The TAC provides an output pulse whose voltage is proportional to the time between the start and stop signals. A multi-channel analyser (MCA) converts this

voltage to a time channel using an analog-to-digital converter (ADC). Once the first photon is detected, the dead time of the electronics prevents detection of another photon resulting from the same excitation pulse. Summing over many pulses, the MCA builds up a probability histogram of counts versus time channels. The histogram of photon arrival times thus represents the intensity decay of the sample.

The use of a constant fraction discriminator provides improved time resolution by removing the variability due to the amplitude of each pulse. The TAC is a rate-limiting component in TCSPC. It takes several microseconds to discharge the capacitor and reset the TAC. With high-repetition-rate laser sources, the TAC will be overloaded due to continuous start pulses. This would require the TAC to be operated in reverse mode. In this mode of operation, the first photon detected from the sample serves as the start pulse and the signal from the excitation pulse is the stop signal. In this way, TAC is activated only if the emitted photon is detected. This type of operation has been adopted in our system, which is described below.

2.2.2 Experimental set up for FRET-FLIM

The experimental set up is depicted in (Fig. 2.3). The set up can be broadly divided into 3 parts namely, Laser system, Optical system and Electronics.

2.2.2.1 Laser system

Components:

Millennia Vs (5W, 543 nm, Spectra-Physics GmbH)
Titanium Sapphire laser (Tsunami 3955, 690-1080 nm, 80 MHz, Spectra-Physics GmbH)
Frequency doubler / Pulse picker (Spectra-Physics 3986)

A femtosecond modelocked Titanium Sapphire laser pumped by a continuous diode laser, Millennia Vs, was tuned and frequency doubled using a frequency doubler/pulse picker to a desired wavelength of 420 nm with a pulse repetition rate of 8 MHz. This wavelength was optimal to excite the donor CFP to at least 80% and the acceptor YFP to less than 5% (Lippincott-Schwartz and Patterson, 2003). The repetition rate of the excitation pulses (125 ns) provided enough time for the fluorophores to relax back to the ground state before they were excited by the next pulse, since the fluorescence lifetimes of the fluorophores used were in the range of 1-5 ns.

2.2.2.2 Optical system

Components

Microscope: IX81, Olympus
OCFD: Optical Constant Fraction Discriminator triggered by laser pulse (Becker & Hickl)
M: mirrors (Edmund Optics)
ND: neutral density filters (Thorlabs)

UV: mercury lamp for steady state imaging (Osram GmbH)
FC: optic fibre coupler (Olympus)
L: planar convex lens (f=+150 mm, Edmund Optics)
I: iris to control the area of excitation of the sample
S: micrometer screw
Polychromator
Dual Image: Europhoton GmbH
CCD: Charge Coupled Device for steady state imaging (F View, SIS Imaging Systems GmbH)
All filters were from AHF Analysentechnik AG unless otherwise stated.

The laser output from the frequency doubler/pulse picker was guided by mirror M1 to a beam splitter (BS). About 10% of the beam was used to trigger the OCFD to provide the stop pulse of the excitation beam to the electronics of the detectors. Two circularly variable neutral density filters ND1 and ND2 were arranged in series to control the power of the beam. The laser beam was coupled alternatively via two optical fibres, with the fibre couplers (FC) mounted on three dimensional micrometer stages (Thorlabs), to different ports of an inverted microscope. This allowed illumination of the sample for the point and imaging detectors via beam paths 1 and 2, respectively. Manually switchable mirrors M2 and M4 were used to alternate between the illumination paths.

To illuminate the sample for the point detector via beam path1, the collimated laser beam from the fibre output was focussed by a convex lens L1, decreasing the area of illumination for the excitation beam. The region of interest was selected by closing an iris I within the excitation path around the beam to limit the area of excitation. The laser beam was finally focussed onto the sample using an oil immersion 100x objective (Plan Apo 100x/1.45 oil, TIRFM, Olympus) after passing a beam splitter 450 DCLP. The fluorescence emission from the tiny selected area passed an emission filter HQ 460 ALP and the slit (11 mm x 0.10 mm) of the polychromator fixed in front of the sensitive area of the point detector, to translate the spectrally resolved intensity decays on the detector. In beam path 2, the collimated beam from the optical fibre was used to provide whole field illumination for the imaging detector which passed the beamsplitter 450 DCLP and illuminated the back focal plane of the 100x objective. The fluorescence was collected via the objective and was reflected to the side port of the microscope after passing an emission filter HQ 460 LP. In front of the imaging detector, a Dual Image was mounted to split the fluorescence into two specific cut off wavelength bands via a beamsplitter (dichroic 505 DCXR). Two bandpass filters defined the width of the wavelength bands of the donor (CFP: D 480/40 M) and the acceptor (YFP: 540/40 ALP). These two fluorescence bands illuminated two different areas of the imaging detector, collecting the dynamics of the donor and acceptor simultaneously.

A possibility to alternate between epifluorescence and TIRF illuminations was also feasible in beam path 2. This was provided by a micrometer screw S attached to a collimating lens L2, which allowed to change the angle of incidence of the excitation beam from epifluorescence mode to TIRF mode, where the beam undergoes total internal reflection at the glass-buffer interface. It was also possible to study the anisotropy of fluorescent probes by including minor changes in the optical set up.
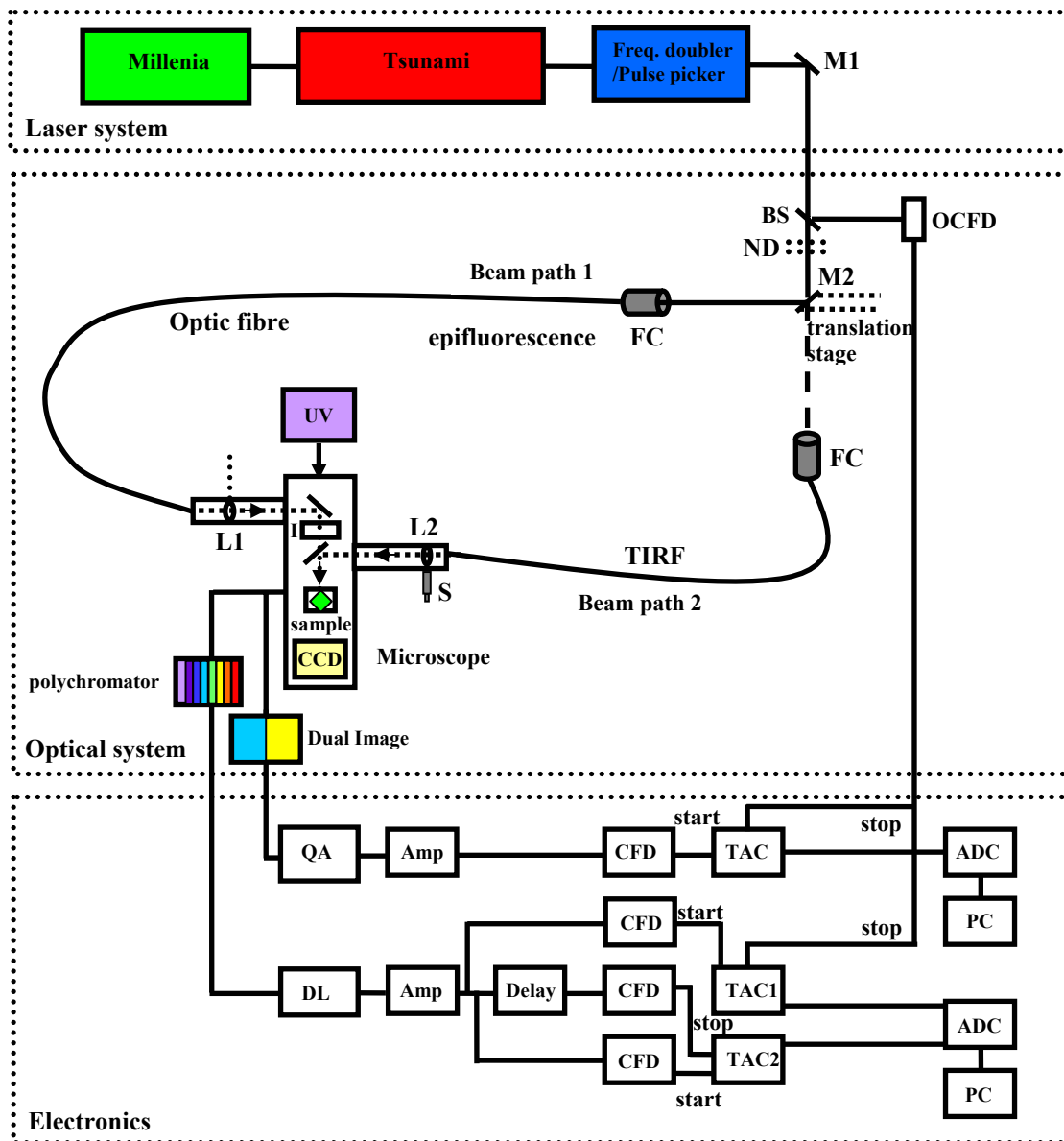
Fig. 2.3 *Experimental system to study picosecond FLIM and FRET. M: mirrors, BS: Beam Splitter, OCFD: Optical Constant Fraction Discriminator, ND: neutral density filters, FC: optic fibre coupler, TIRF: Total Internal Reflection Fluorescence mode, L: planar convex lens, UV: mercury lamp, I: iris, S: micrometer screw, CCD: Charge Coupled Device, QA: Quadrant Anode, DL: Delay Line, Amp: Amplifier, CFD: Constant Fraction Discriminator, TAC: Time to Amplitude Converter, ADC: Analog to Digital Converter, PC: Personal Computer.*

2.2.2.3 Electronics

Components

QA- Quadrant Anode detector (Europhoton GmbH)
DL-Delay Line detector (Europhoton GmbH)

Amp- Amplifiers (10V)
CFD- Constant Fraction Discriminator (Tennelec)
TAC- Time to Amplitude Converter (Tennelec)
TAC1- Time TAC for Delay Line Detector
TAC2- Space TAC for Delay Line Detector
ADC- Analog to Digital Converter (Tennelec)
PC- Personal Computer

The Delay Line (DL) and Quadrant Anode (QA) detectors (Kemnitz et al., 1997), based on Time and Space Correlated Single Photon Counting (TSCSPC) were used to study the interaction between tagged flourophores by simultaneous acquisition of time and space information at picosecond scale. Here statistical averaging of the acquired single photons in time is done.

One dimensional imaging by the DL or point detector was used to statistically analyse a very small area of the sample (5-10 μm) and to resolve spectrally the corresponding fluorescent decays using a polychromator placed in front of the point detector. The spectrally resolved decays were collected by the detector as an electron cloud generated by a photocathode and amplified by two multi-channel plates. The amplified electron cloud fell on a Delay Line disc producing current pulses in mutually opposite direction. The position of the single photon was traced one dimensionally from the travel time difference of the foresaid current pulses generated by the electron cloud falling on the detector. Time correlation was done by measuring the time difference between the current pulses generated from the second multi-channel plate and the signal from the OCFD triggered by the excitation laser beam (O'Connor and Phillips., 1984). The electronic read-out consisted of standard NIM (Nuclear Instrument Modules) or alternatively, an integrated system incorporating CFDs, TACs and 2D-MCA on a single PC board. The functions of individual components have already been discussed in Section 2.2.1. The multi-parameter data acquisition translated time and space coordinates into intensity dependent colour contour with 256 space channels and 1024 time channels.

The two dimensional QA or imaging detector was used to image the fluorescence decays within the whole illuminated region simultaneously. An incident single photon was converted into a cone shaped cloud of electrons by a photocathode and two microchannel plates in series. The electron cloud fell on four independent detector areas and from the ratio of charges developed in each of these single areas, initial (x-y) position of the photon was traced back into two dimensional spaces. For time correlation, a time to amplitude converter was used between the signal coming from the second MCP and signal from the OCFD triggered by the excitation pulse to give the start and stop pulses, respectively. Space and time correlated data were recorded as a 3D matrix of 512 x 512 space channels and 4096 time

channels. The QA capture software (Europhoton GmbH) was used to control the data acquisition of the imaging detector. Measurements were performed by continuously acquiring the photons for a certain time to achieve a good signal to noise ratio. The imaging detector was cooled throughout the measurements between 14°C - 16°C to avoid over heating. The dynamic range of the cooled detector was $>10^6$ with the quantum efficiency of the photodiode being 30%.

Though an initial system had been constructed, such an open system with free calibration of the optical system with mirrors posed the difficulty of daily major adjustments depending on the laser output. The Titanium Sapphire laser with manual modelocking system gave unpredictable laser output positioning and required the adjustment of the whole system, which was highly time-consuming for daily measurements. Therefore, it was essential to modify the optical system to make it more stable i.e. to make the input beam on the sample more independent from the laser output. The current experimental system was made for this purpose. Though a daily calibration of the optic fibre input was essential, the independence of the beam positioning inside the microsope from the laser output made the calibrations much easier and less stressfull.

2.2.3 Calibration of the set up

The pulse width of the instrument response function in the point detector was reduced to a minimum of 150±25 ps, measured at full width half maximum by adjusting the threshold and zero control of the OCFD. A further reduction of the pulse width was not possible due to the rapid fall of counts caused by very low excitation intensity. Optimal excitation intensities at the sample less than 100 μW/cm^2 (measured by a laser powermeter, PD-300-3W, Ophir Optronics GmbH) was chosen to avoid phototoxicity of cells during measurement.

The wavelength calibration of the point detector was performed using a Xenon lamp (6025 Hg (Ar), Oriel Instruments) and the illumination intensity was controlled using neutral density filters. The defined emitted lines of the lamp were compared to the lines observed in the spectral window of the detector, and thereby the wavelength channels optimised. The wavelength sensitivity of the system was characterised to be 1.02 nm/channel. White light calibration was also done to study the efficiency of detection over the entire spectra. The time calibration of the point detector was performed by measuring the instrument response function at different known delays and thereby optimising the time channels from the shift in the decay along the time channels for the corresponding delays. The time channel resolution of the point detector was calculated to be 24.81 ps/channel.

The pulse width of the instrument response function of the imaging detector was reduced to a minimum of 200±20 ps at full width half maximum. The space calibration of the imaging detector was performed using fluorescent beads of 1 μm and 0.17 μm diameters (ex: 490 nm / em: 515 nm, Ps-Speck™, Molecular Probes Inc.). The detector was optimised to result in the best focussed image of the bead in the image plane with the minimum diameter. Time calibration of the imaging detector was performed similar to the calibration of the point detector by changing the delay and calculating the shift along the time channels. The time channel resolution of the imaging detector was calculated to be 9.72 ps/channel.

Independent control measurements of the monoexponential dye coumarin6 (Sigma) in ethylene glycol at magic angle, excited at 420 nm and observed in a band of 515±15 nm (HQ 515/30), were performed with both the point and imaging detectors.

2.2.4 Data analysis

The fluorescence emission spectra obtained from the point detector were normalised to the emission peak of the donor and the R values were calculated as the ratio of intensities at the emission maxima of acceptor to donor. The fluorescence decays were analysed by Levenberg-Marquardt non-linear least-squares algorithm using the Globals Unlimited software package (Version 1.20, (Beechem and Haas, 1989)) developed at the Laboratory for Fluorescence Dynamics at the University of Illinois at Urbana-Champaign. The decays were modelled by the convolution product of a multi-exponential theoretical model with the instrument response function (IRF): $i(t) = IRF(t) \otimes \Sigma \alpha_i e^{-t/\tau_i}$, where α_i is the relative contribution of fluorescent species characterised by the fluorescence lifetime τ_i, and IRF is the pulsed excitation obtained by acquiring the reflection of the laser beam to the detector. The quality criterion for global fit was defined as $\chi^2 < 1.3$ for all analysed decays. The criterion for improvement of χ^2 on addition of multi-exponential components were set to a value of $\Delta\chi^2$, the ratio between the χ^2s of the previous model and the current model on addition of a single lifetime component, where $\Delta\chi^2 > 1.05$. χ^2 was checked using the linked multi-exponential model and the unlinked model and the data set was discarded if the ratio of χ^2s was greater than 1.05, indicating a random error originating from the data acquisition.

Data obtained from the point detector were fit with linked lifetimes along different decays corresponding to different emission wavelengths. The individual decays were obtained by binning data over a fixed number of continuous wavelength channels, resulting in a net resolution of 6.12 nm or 7.14 nm per decay. The contributions of the multiple lifetimes in the intensity decays were obtained as pre-exponential factors α_i. The pre-exponential factors of lifetimes were positive except in the case of excited state reactions, where they change to

negative (Lakowicz, 1999). α_is obtained from the individual decays were plotted as a function of wavelength to obtain the DAS. The comparison of DAS of different multi-exponential components allowed to discriminate fluorescent species involved in different excited state processes. DAS was also used to deduce the fractional contributions of the different lifetimes along the wavelength from the pre-exponential factors as $|\alpha_i| / |\sum\alpha_i|$. The mean lifetime of a multi-exponential fluorophore was calculated as $\tau_{mean} = |\sum\alpha_i\tau_i| / |\sum\alpha_i|$, where τ_i is the lifetime and α_i is the corresponding pre-exponential factor. The individual counts at the peak for each analysis was maintained between 6000 and 7000.

Data obtained by the imaging detector were analysed by selecting corresponding regions of interests (ROIs) for the donor and acceptor channels as defined by the filter settings of the Dual Image. The data sets of individual channels were exported in the Globals Unlimited software format. The donor and acceptor decays were analysed with linked lifetimes. For comparing the decay differences at different intracellular compartments of cells, the peak counts were always ensured to be >10,000.

FRET efficiencies were calculated as $E = 1 - \tau_{DA} / \tau_D$, where τ_D is the unperturbed lifetime of the donor and τ_{DA} is the lifetime of the donor in the presence of an acceptor. The distance between the donor and acceptor fluorophores was calculated as $r = R_0(1/E-1)^{1/6}$, where R_0 is 4.92 nm for CFP-YFP pairs (Patterson et al., 2000). The distance calculations were done assuming a random orientation of the dipole moments with $\kappa^2 = 2/3$.

Rigorous error analysis using the global analysis program was performed to obtain a realistic estimation of the variation of χ^2 associated with each lifetime. The global analysis program employed a completely rigorous error estimation procedure. Within the error analysis segment, a set of intervals was defined for each lifetime in the model performing a complete set of analysis. The examined parameter was fixed at the current trial value, but all other parameters were allowed to vary to minimize the value of χ^2. A plot of the change of χ^2 with the change in lifetimes was obtained. Comparison of these results with the obtained multi-exponential model was used to judge the quality of lifetimes in the fit. The intensity decays of coumarin6 at magic angle were observed to be monoexponential with lifetimes of 2.30 ns for the point detector and 2.29 ns for the imaging detector, which was comparable to the published value of 2.30 ns (Kapusta et al., 2003). This was done to ensure that the effects observed were purely cellular.

3 MATERIALS AND METHODS

3.1 MATERIALS

All chemicals used were of analytical grade and from the companies Calbiochem, Invitrogen, Merck, Roche, Roth, Serva and Sigma-Aldrich. Special chemicals and solutions utilised are detailed in the corresponding method descriptions. Solutions were prepared with water purified on a Milli-Q® System, Millipore, unless for mammalian cell culturing where special distilled water for tissue culture (Invitrogen) was used.

3.1.1 Media and supplements for different cell types including Bacteria, COS-7, and hippocampal neurons

Name	Composition / Company
LB medium	20 g LB broth base powder (Invitrogen) in 1 l H_2O.
2-YT medium	31 g 2-YT broth powder (Invitrogen) in 1 l H_2O.
S.O.C. medium	20 g/l SELECT peptone 140 (Invitrogen), 5 g/l SELECT yeast extract (Invitrogen), 10mM NaCl, 2.5mM KCl, 10mM $MgCl_2$, 10mM $MgSO_4$, 20mM glucose.
LB agar	15 g select agar (Invitrogen) in 1 l LB medium.
DMEM	Dulbecco's Modified Eagle's medium (Invitrogen)
Neurobasal medium	without phenol red (Invitrogen)
Optimem	without phenol red (Invitrogen)
Kanamycin	25 mg/ml Kanamycin disodium salt in H_2O. Final concentration: 25 µg/ml in LB medium.
Ampicillin	50 mg/ml Ampicillin natrium salt in H_2O. Final concentration: 100 µg/ml in LB medium.
Chloramphenicol	12.5 mg/ml Chloramphenicol in ethanol. Final concentration: 30 µg/ml in LB medium.
IPTG	238 mg/10ml. Final concentration: 5% in LB medium.
X-Gal	Final concentration: 2% in LB medium.

Media and antibiotics used for growth of bacteria, COS-7 or primary cultures of hippocampal neurons. Unless provided from the Company, all media were autoclaved at 121ºC for 15 min.

3.1.2 Buffers

Buffer	Composition
HBSS	Hank's Balanced Salt Solution (Invitrogen)
Gluconate Buffer	147mM Na^+ gluconate, 10mM Hepes, 0.1% Tween 20, 0.025% Na Azide, pH 7.4 osmolarity adjusted to 305 mOsm/l with K^+ gluconate
Buffer A	150mM Na^+ gluconate, 50mM MES, pH 5.9
Buffer B	150mM Na^+ gluconate, 50mM MES, pH 6.4
Buffer C	150mM Na^+ gluconate, 50mM MOPS, pH 6.9
Buffer D	150mM Na^+ gluconate, 10mM Hepes, 10mM K^+ gluconate, pH 7.6
Buffer E	150mM Na^+ gluconate, 50mM Bicine, pH 8.2
Chloride calibration buffers	10mM Na^+ gluconate, 10mM Hepes, pH 7.4 Concentrations of KCl varying between 0mM-1M, with corresponding decrease in concentrations of K^+ gluconate from 150mM-0mM.
1xKD	129mM NaCl, 5mM KCl, 2mM $CaCl_2$ $2H_2O$, 1mM $MgCl_2$ $6H_2O$, 20mM Hepes, 30mM Glucose, pH 7.4
Buffer 1	10mM EDTA, 50mM Tris/HCl, pH 8.0, 100 µg/ml RNAse

Buffer 2	0.2M NaOH, 1% (wt/vol) SDS
Buffer 3	3M potassium acetate, pH 5.5
PBS	2.7mM KCl, 1.5mM KH_2PO_4, 137mM NaCl, 8mM Na_2HPO_4, pH 7.4
PBS / T	0.05% (vol/vol) Tween 20 in PBS, pH 7.4
Elution buffer	150mM imidazol in 2xPBS, pH 7.0
4xSDS buffer	250mM Tris/HCl, pH 6.8, 4% (wt/vol) SDS, 40% (vol/vol) glycerol, 4% β-mercaptoethanol, 0.02% bromphenol blue
Electrophoresis buffer for SDS-PAGE	250mM Tris, 1.92mM glycine, 1% (wt/vol) SDS
Western blot buffer	25mM Tris, 192mM glycine, 0.02% (wt/vol) SDS, 18% (vol/vol) methanol
6xloading buffer	30% (vol/vol) glycerol, 50mM EDTA, 0.25% (wt/vol) bromphenol blue, 0.25% (wt/vol) xylene cyanol
1xTBE	89mM Tris, 89mM boric acid, 2mM EDTA, pH 7.6
1xTAE	40mM Tris, 0.2mM acetic acid, 1mM EDTA, pH 7.6

Frequently used buffers and their compositions. Unless provided from the Company, all buffers were sterile filtered when using for cell culture or protein purification.

3.1.3 Iontophoretic drugs

Drug	Concentrations/Company
Nigericin	10mM Stock (10 mg / 1.45 ml) in methanol (Sigma)
Tributyltin chloride	10mM stock (13.54 µl TBTC / 5 ml) in DMSO (Sigma)

Iontophoretic drugs with their stock concentrations.

3.1.4 Cell strains

Cell type	Strains/Company
Bacteria	*E. coli DH5α* (Invitrogen)
	E. coli Top 10F' (Invitrogen)
	E. coli XL1-Blue electrocompetent cells (Stratagene)
	E. coli XL1-Blue Supercompetent cells (Stratagene)
	E. coli XL10-Gold (Stratagene)
	E. coli BL21-CodonPlus® DE3-RIPL (Stratagene)
Mammalian cells	African green monkey (COS-7)

Cell strains used for the studies

3.1.5 Animals

Rats (*Rattus Rattus norvegicus*) from the strain Wistar, bred at the animal facility of Leibniz Institute for Neurobiology, were used for the preparation of primary neuronal cultures.

3.1.6 Antibodies

Primary antibodies	Company / Reference	Dilution	
		IF	WB
mouse-anti-Bassoon[1]	mab7f (Stressgen)*	1:1000	
mouse-anti-CtBP1[2]	BD Transduction Laboratories	1:1000	
mouse-anti-syntaxin6	BD Transduction Laboratories	1:500	
mouse-anti-GFP	Synaptic systems	1:200	1:10,000
rabbit-anti-Bassoon[1]	sap7f*	1:500	
rabbit-anti-SAP90/PSD95	Synaptic systems	1:200	
rabbit-anti-KCC2	Upstate	1:800	
rabbit-anti-GFP	Synaptic systems	1:200	

Primary antibodies used. IF: immunofluorescence assays; WB: Western Blot. The antibodies marked as * were obtained from Dept. of Neurochemistry/Molecular Biology, IfN.

[1](tom Dieck et al., 1998), [2](tom Dieck et al., 2005)

Secondary antibodies	Company	Dilution
peroxidase-conjugated goat anti-mouse IgG	Dianova	1:10,000
Alexa Fluor® 488 goat anti-mouse/rabbit IgG F(ab')	Molecular Probes	1:200
Alexa Fluor® 568 goat anti-mouse/rabbit IgG F(ab')	Molecular Probes	1:200
Alexa Fluor® 594 goat anti-mouse /rabbit IgG F(ab')	Molecular Probes	1:200
Cy3 goat anti-mouse/rabbit IgG	Dianova	1:100
Cy5 goat anti-mouse/rabbit IgG	Dianova	1:100

Secondary antibodies used.

3.1.7 Expression constructs

Construct (Name)	Gene	Source
1-97Bsn-EGFP[1]	Bassoon	Thomas Dresbach, IfN
1-609Bsn-EGFP[1]	Bassoon	Thomas Dresbach
GFP-Bsn1692-3263[1]	Bassoon	Wilko Altrock, IfN
Cerulean-Bsn1692-3263	Bassoon	Wilko Altrock
Citrine-Bsn1692-3263	Bassoon	Wilko Altrock
EGFP-Bassoon[1]	Bassoon	Thomas Dresbach
Cerulean-CtBP1	CtBP1	Wilko Altrock
Cerulean-CtBP1 mut	CTBP1 mutant	Wilko Altrock
Citrine-CtBP1	CtBP1	Wilko Altrock
EGFP-CAST	CAST/ELKS2	Thomas Dresbach
Cerulean-CAST	CAST/ELKS2	Self cloned
Citrine-CAST	CAST/ELKS2	Self cloned
EGFP-VAMP2	VAMP2/Synaptobrevin	Thomas Dresbach
mRFP-VAMP2	VAMP2/Synaptobrevin	Thomas Dresbach
Cerulean-VAMP2	VAMP2/Synaptobrevin	Self cloned
Citrine-VAMP2	VAMP2/Synaptobrevin	Self cloned
Cameleon[2]	Cameleon	R.Y.Tsien, California
Clomeleon[3]	Clomeleon	Thomas Kuner, Heidelberg
pEGFP	EGFP	Clontech
pECFP	ECFP	Clontech
pEYFP	EYFP	Clontech
PCerulean[4]	Cerulean	David Piston, Tenessee
pCitrine[5]	Citrine	R.Y.Tsien
pQE30-Clomeleon[3]	Bacterial vector of Clomeleon	Thomas Kuner, Heidelberg
pQE30-Cyan	Bacterial vector of CFP	Thomas Kuner, Heidelberg

The different expression constructs used for the present work. cDNAs noted as *-tag and tag-* denote the tags located at the C-terminus and N-terminus of the constructs respectively. All constructs were cloned into GFP vectors. Cloning works were done with the help of Dr. Ulrich Thomas, IfN.

[1](Dresbach et al., 2003), [2](Miyawaki et al., 1997), [3](Kuner and Augustine, 2000), [4](Rizzo et al., 2004), [5](Griesbeck et al., 2001).

3.1.8 Primers

Name	Primer sense	Sequence (5'→ 3')
M13_fw	F	GTAAAACGACGGCCAG
M13_rev	R	CAGGAAACAGCTATGAC

Primers used for sequencing the cloned constructs. F = Forward; R = Reverse. All primers were from Invitrogen.

3.2 METHODS

3.2.1 Molecular Biological Techniques

3.2.1.1 Transformation of electrocompetent cells

0.4 μg DNA was mixed with bacterial cells thawed on ice and this mixture was transferred into an electroporation cuvette to which an electroshock was applied (C = 25 μF, R = 200 Ω and U = 2.5 kV) using a Gene Pulser (BioRad). Cells were immediately resuspended in S.O.C. medium, incubated for 1 h at 37ºC and plated on LB agar plates containing the appropriate antibiotics.

3.2.1.2 Transformation of heat-shock competent cells

0.4 μg DNA was mixed with bacterial cells thawed on ice and incubated for 15 min. Heat shock was given for 45 s at 37ºC for DH5α, 30 s at 42°C for Top10F' and 45 s at 42°C for XL10 and supercompetent cells (Section 3.1.4). The mixture was again incubated for 2 min on ice, during which S.O.C medium was added and incubated for 1 h at 37°C. The transformed cells were plated on LB agar plates containing the appropriate antibiotics.

3.2.1.3 Preparation of plasmid DNA from *E. coli*

Alkaline lysis was adopted for plasmid purification. 2-4 ml of overnight culture was spun down and the pellet resuspended in 0.2 ml of Buffer 1 (Section 3.1.2). 0.2 ml of Buffer 2 (Section 3.1.2) was added to disrupt the cell membrane, denature proteins and DNA, and hydrolyse RNA. The suspension was neutralised with 0.2 ml of Buffer 3 (Section 3.1.2), allowing precipitation of the denatured proteins along with the chromosomal DNA and most of the SDS detergent. The precipitates were removed by centrifugation and the plasmid-containing supernatant was further purified via isopropanol precipitation. 0.35 ml isopropanol was added to the plasmid-containing supernatant; the mixture was incubated for 10 min on ice and finally the DNA was pelleted at 20×10^3 g for 10 min. Pelleted DNA was washed twice with 70% (vol/vol) ethanol, resuspended in H_2O and stored at -20ºC. To transfect mammalian cells, plasmids were prepared using endofree-Plasmid Purification Midiprep/Maxiprep Kit (Qiagen).

3.2.1.4 Restriction reactions of plasmid DNA

Restriction endonucleases cleave the plasmid DNA strands after recognising specific nucleotide sequences. To clone or subclone a cDNA fragment into a vector, both the insert and the vector were submitted to a restriction reaction using the appropriate restriction endonucleases, buffers, reaction temperatures and time conditions (normally 1 h - 1.5 h at 37ºC) recommended by the manufacturer (New England Biolabs or Fermentas). Since double

digestions were rarely 100% efficient, sequential digestion was chosen in most of the cases. The vectors were heat inactivated after digestion and dephosphorylated with antarctic phosphatase (Roche) to prevent re-ligation of the cohesive ends.

3.2.1.5 Agarose gel electrophoresis

DNA fragments obtained after a restriction reaction were separated according to their size by agarose gel electrophoresis. 0.5-1.5% (wt/vol) agarose was melted in TBE/TAE buffer (Section 3.1.2). The latter was used only in cases where DNA purification from the gel was required. 0.1 µg/ml ethidium bromide was added to the agarose gel solution for ultraviolet imaging and poured into a chamber. After adding 6x loading buffer (Section 3.1.2) to the samples, they were loaded onto the solidified agarose gel. Smart Ladder (Eurogentec) was used as a reference standard. The gels were run at 120 V in TBE/TAE buffer and were documented with the gel documentation system Gel Doc (BioRad). For DNA purification, the bands of interest were cut out by viewing with a Transilluminator (Stratagene) and purified using the UltraClean^{TM} 15 purification kit (MoBio Laboratories Inc) following the instructions of the manufacturer.

3.2.1.6 Polymerase chain reaction (PCR)

The polymerase chain reaction is a common method used to amplify a sequence of DNA, where a pair of oligonucleotide primers, each complementary to one end of the DNA target sequence, are employed. The primers are extended by a thermostable DNA polymerase in a reaction cycle of three steps: denaturation of double stranded DNA, primer annealing and polymerisation of new nucleotides at the 3' end of the primer following the sequence of the template DNA. PCR reactions were performed using 125 ng of both forward and reverse primers (Section 3.1.8), 200µM of deoxynucleoside triphosphate (Stratagene), 2.5 units of DNA polymerase (Stratagene/Invitrogen), 5µl of 10x reaction buffer and 20-50 ng of template DNA. The PCR products were normally cloned into TOPO-TA vector (Invitrogen). For the purpose, 0.5-4 µl of the PCR product was incubated with TOPO vector along with diluted salt solution for 5 min at RT. The ligation products were transformed into *Ecoli Top10F'* and plated on Ampicillin/XGal/IPTG agar plates.

3.2.1.7 Site-directed mutagenesis

Mutagenesis was done to introduce point mutations for single or multiple amino acid exchanges into cDNAs. It was efficiently done using Quick-change site-directed mutagenesis kit (Stratagene). DpnI restriction enzyme was added to the mutated amplification products and the mixture was incubated at 37°C for 1 h to digest the parental supercoiled (non-

mutated) dsDNA. The mixture was transformed into *Ecoli XL1-Blue Supercompetent cells* (Section 3.1.4).

3.2.1.8 Cloning of DNA fragments into vectors

To introduce a DNA fragment into an expression vector, the T4 DNA ligase (Fermentas) was used. The ligation reactions were performed overnight at 18ºC. The reaction product was transformed into *Ecoli DH5α* (Section 3.1.4). Plasmids were prepared from single colonies and were sequenced (Section 3.1.8, SEQLAB Sequence Laboratories Göttingen GmbH) or submitted to restriction analysis to confirm the correct insertion of the cloned or subcloned DNA.

3.2.1.9 Generation of Cerulean and Citrine fused constructs of Bsn1692-3263, CtBP1, CAST and VAMP2

A central fragment of Bassoon cDNA encoding amino acid residues 1692-3263 (Bsn1692-3263) was cloned into frame shifted variants of p-Cerulean and p-Citrine cDNAs (Section 3.1.7) using BamHI/BamHI restriction sites. CtBP1 cDNA was cloned into frame shifted variants of p-Cerulean and p-Citrine cDNAs using EcoRI/XhoI restriction sites introduced via linkers. The frame shifted variants of p-Cerulean and p-Citrine were generated using standard molecular biological techniques. For cloning of CAST/ELKS2 and VAMP2/Synaptobrevin into p-Cerulean and p-Citrine cDNAs, the original GFP fusion constructs (Section 3.1.7) were sequentially digested with BamHI and SacI endonucleases and purified from a TAE gel. The fragments were ligated with Cerulean and Citrine vectors which were also digested with BamHI/SacI, heat inactivated and precipitated using isopropanol. The insertions were confirmed using BglII/BamHI digestions and finally sequenced (Section 3.1.8).

3.2.2 Protein Biochemistry

3.2.2.1 Expression and affinity purification of proteins

Clomeleon and CFP were purified via Metal Affinity Chromatography. The bacterial expression vectors, pQE30-Clomeleon and pQE30-Cyan, were expressed in *E. coli XL1 blue* (Section 3.1.4). 2xYT medium prepared from an overnight pre-culture was inoculated at 37°C for the O.D. to reach 0.5-0.6, which was induced with 100mM IPTG and incubated for 8-12h at 20°C. The cells were harvested and resuspended in 2xPBS containing EDTA-free complete tablet, DNAse I (5 µg/ml) and RNAse A (10 µg/ml). The cells were lysed and treated with Triton X-100 (0.1%), and then centrifuged. The supernatant was added onto equilibrated Talon Metal Affinity Resin (BD/Clontech), which recognised the hexahistidine tags of the

proteins. The proteins were eluted using a suitable elution buffer (Section 3.1.2). Aliquotes were collected throughout the procedure to confirm using SDS-PAGE.

3.2.2.2 SDS-PAGE

Sodium dodecyl sulfate polyacrylamide gel electrophoresis (SDS-PAGE) is a method to separate proteins loaded on an acrylamide gel under denaturing conditions (Schagger and von Jagow, 1987). The stacking gel was poured on a separating gel (resolving gel). Depending on the size of the proteins to analyse, 5-15% acrylamide resolving gels were prepared. Samples were incubated for 5 min with 4x SDS-sample buffer (Section 3.1.2) at 96ºC. 'Protein Ladder' (Page Ruler^{TM}, Fermentas) was used as a reference standard. Gels were run at 8 mA in an electrophoresis chamber (Hoefer Mighty Small System SE250, Amersham Biosciences) filled with electrophoresis buffer (Section 3.1.2) and were developed using Coomassie staining or were immunoblotted.

3.2.2.3 Coomassie staining of SDS-polyacrylamide gels

Polyacrylamide gels were stained with Coomassie solution (1 mg/l Coomassie Brilliant Blue R250, 60% (vol/vol) methanol, 10% (vol/vol) acetic acid), and destained with 5% (vol/vol) methanol, 7% (vol/vol) acetic acid until the protein bands were distinguishable. The gels were incubated in 50% (vol/vol) methanol and 5% (vol/vol) glycerol for long term storage.

3.2.2.4 Fast Performance Liquid Chromatography

FPLC was done using a Superdex 200 column (GE Healthcare Life Sciences) to separate the purified protein components depending on their size, so as to select suitable fractions among them. This was essential for purified Clomeleon since the contribution of cleaved single CFP and Topaz molecules were significant, as revealed from Coomassie staining of SDS gels. Gluconate buffers (Section 3.1.2) containing 0mM Cl$^-$ were used for the purpose.

3.2.2.5 Determination of protein concentrations

Micro Amidoblack Protein assay is an efficient calorimetric method to determine purified protein concentrations (Stoscheck, 1990). 0-20 µg BSA (in PBS) as well as doublets or triplets of 40 µl and 60 µl protein samples adjusted to 100 µl with water, were mixed with 200 µl amidoblack solution (14.4 g amidoblack in 1 l methanol-acteic acid (9:1), filtered) and incubated for 20 min at RT. The mixture was centrifuged and the protein pellet was washed twice with methanol-acetic acid, after which it was dried and resuspended in 0.1 N NaOH. The O.D. was measured at 620 nm to yield a calibration curve of BSA, from which the protein concentrations of the samples were calculated. Micro Amidoblack protein assays showed the protein concentrations to be >20 ng/µl for the fractions selected using FPLC for the optical measurements.

3.2.2.6 Protease digestion

Purified Clomeleon was digested with rTEV protease (Invitrogen) in presence of 0.1M DTT, which recognised the ENLYFQG cleavage site. The temperatures and reaction times were varied according to the recommendations of the manufacturer to yield >90% of cleaved protein, as determined by Western Blots.

3.2.2.7 Western blotting and immunodetection

Western blotting was done to transfer proteins from a polyacrylamide gel to a nitrocellulose membrane. Proteins were transferred at 200 mA for 1 h 30 min in a transfer tank (Hoefer TE 22 Mini Tank Transphor Unit-System, Amersham Biosciences) filled with Western blot buffer (Section 3.1.2). The nitrocellulose membranes were stained with 0.5% (wt/vol) Ponceau solution containing 1% (vol/vol) acetic acid and blocked for 1 h at RT with Blotto* (5% (wt/vol) skimmed milk powder, 1% (wt/vol) BSA, in PBS/T). Membranes were incubated overnight at 4ºC with the primary antibodies and after washing with PBS/T, further incubated with HRP-coupled secondary antibodies for 1 h at RT. The membranes were incubated with ECL-detection system (Amersham Biosciences) according to the manufacturer's protocol and the light emitted was collected on a chemiluminescence-sensitive film (HyperFilm, Amersham Biosciences), which was developed in an Agfa-Curix-60 developing machine.

3.2.3 Cell Culture Techniques

3.2.3.1 Mammalian cell cultures (COS-7 and primary hippocampal neurons)

COS-7 cells were grown in DMEM (Section 3.1.1) containing 10% FCS, antibiotics (100 U/ml penicillin, 100 μg/ml streptomycin) and 2mM glutamine at 37°C, 5% CO_2 environment. They were plated at a density of 10^5 cells per well (0.5 ml) in 24 well plates for transfections. Primary hippocampal cultures were prepared according to the method of Goslin et al (Goslin et al., 1998) with some modifications. The hippocampal cells from E18-E19 rat embryos were plated in DMEM including 10% Fetal Calf Serum (FCS), antibiotics (100 U/ml penicillin, 100 μg/ml streptomycin) and 2mM glutamine at a density of 40×10^3-60×10^3 cells per well (0.5 ml) for transfection, and at 20×10^3 cells per well for immunostainings in 24 well plates. Medium density neuronal cultures were optimal for imaging at mature stages. 24 hours after plating, the medium was exchanged for Neurobasal medium (Section 3.1.1) containing 2% B27, 1% antibiotics and 0.5mM glutamine and incubated at 37°C, 5% CO_2 environment. Neuronal transfections were done in Neurobasal medium without antibiotics, but containing other supplements.

3.2.3.2 Transfection and immunocytochemistry

COS-7 cells and hippocampal neurons were transfected using PolyFect Transfection Reagent (Qiagen) and Lipofectamine 2000 (Invitrogen), respectively, according to the manufacturer's protocols. Unless used for live imaging or after FLIM measurements, the cells were fixed with 4% PFA in PBS for 10 min and washed with PBS. They were permeabilised (except for imaging of membrane associated proteins) with 0.2% Triton X-100 for 5 min and blocked with 1% BSA in PBS for 10 min at RT. Primary antibody incubation was done overnight at 4°C (Section 3.1.6). After blocking with BSA, secondary antibody incubation was done for 1 h at RT (Section 3.1.6). Finally the immunostained cultures were washed with PBS and water and embedded with Vectashield (Vector Laboratories Inc.). Immunostainings against endogenous proteins were also done in a similar manner.

3.2.4 Fluorescence Techniques

3.2.4.1 Time-resolved imaging

FRET-FLIM measurements on transfected cultures were done with the experimental set up described in Section 2.2.2. The living cells were imaged in the buffer 1xKD (Section 3.1.2). The measured cells were marked and reidentified after immunocytochemistry, if needed.

3.2.4.2 Steady-state and time-lapse imaging

To perform steady-state imaging, the microscope was equipped with a CCD camera (F View). Mercury lamp excitation was used for imaging the living cells expressing the different proteins of interest, and the CFP/Cerulean and YFP/Citrine/Topaz signals were collected by filter settings (excitation, dichroic, emission); D436/20, 455 DCLP, and D480/40 and HQ 500/20, Q515 LP and HQ 535/30, respectively. Only the cells showing moderate expression levels of the transfected constructs were used for steady-state imaging and FLIM. The captured images gave an account of the morphology of the cells which were measured. Confocal fluorescence images and DIC images were taken with Leica-TCS-SP2-AOBS (Leica Microsystems). Time-lapse studies were carried out with confocal Leica-TCS-SP2-AOBS as well as with wide field video microscopy at 37°C, optimal for viewing transport of vesicles. The images were processed with Adobe Photoshop CS. The particle tracking in neurons were done with Image J.

3.2.4.3 Chloride and pH calibration studies

To regulate the intracellular chloride concentrations, COS-7 cells were incubated with gluconate buffers containing varying amounts of chloride (Section 3.1.2) along with 100μM Nigericin and 50μM Tributyltin chloride (TBTC) for 13-17 min. The buffers were changed in

between to ensure stabilisation of intracellular ionic concentrations. Similar studies were done by mixing purified Clomeleon and CFP with varying concentrations of KCl to yield 0-50mM, 100mM, 250mM and 500mM Cl⁻. Equal amounts of proteins were used in all the cases to avoid differences in excitation conditions. pH studies of purified proteins were done using suitable buffering conditions from pH 6.0-8.0 at 0mM Cl⁻ (Buffers A-E, Section 3.1.2). The final pH values after mixing with the proteins were reconfirmed using pH indicators.

3.2.5 Computational Techniques

3.2.5.1 Modelling

The structure of Clomeleon and of its fluorescent N- and C-terminal domains is not known. Therefore, the structure of Clomeleon was built by homology modelling. Each domain and linker sequence were analysed by a NCBI BLASTp search against structures from the protein data bank PDB (http://www.rcsb.org, (Berman et al., 2000)). The resulting aligned sequence fragments were modelled by blast2model (Sauder, 1999). Finally, the structure of Clomeleon was constructed using PDB entries 1QA, 1PGY and 1GFP as templates for CFP, the rTEV site and YFP, respectively. The two fluorescent domains of Clomeleon are likely to build a close heterodimeric arrangement. Currently, 12 dimeric structures of fluorescent proteins are listed in the PDB. To increase the number, a library of template dimer structures was built by selecting potential dimer pairs from a data set of crystal symmetry related molecules calculated for 50 different crystal structures of fluorescent proteins, all members of the GFP beta barrel folding class. For each template, the pre-modelled domains were arranged accordingly and the glycine-serine linker was fit using a PDB loop database (Berman et al., 2000). The interface was positionally refined (Brunger, 1988; Guex and Peitsch, 1997) and validated by programs WHAT IF (Vriend, 1990) and PROCHECK (Laskowski et al., 1996). The aim of the modelling was to restrain the coordinates of the fluorescent domains, but build the most compact structural complex. Experimental dimers of fluorescent proteins are in anti-parallel or cross-like orientation. For comparison, a parallel oriented heterodimer was arranged manually and the interface refined. The model allowed an estimation of the inter-chromophore distance between CFP and Topaz in Clomeleon. 3D structure predictions were also done for the presynaptic protein Bassoon.

All computational modelling works were done by Carsten Reissner, IfN.

4 RESULTS

4.1 PHOTOPHYSICS OF CLOMELEON BY FLIM: DISCRIMINATING EXCITED STATE REACTIONS ALONG NEURONAL DEVELOPMENT

4.1.1 Discrimination of FRET from other excited state reactions

One of the major challenges addressed in this work was to discriminate FRET from other excited state reactions along neuronal development. In order to do so, it was essential to understand the perturbation of donor lifetimes to the different photophysical processes to discriminate it from FRET. Therefore, the fluorescence dynamics of purified CFP was studied under different pH and chloride conditions. The effects were compared with ECFP expressed at different stages of neuronal maturation.
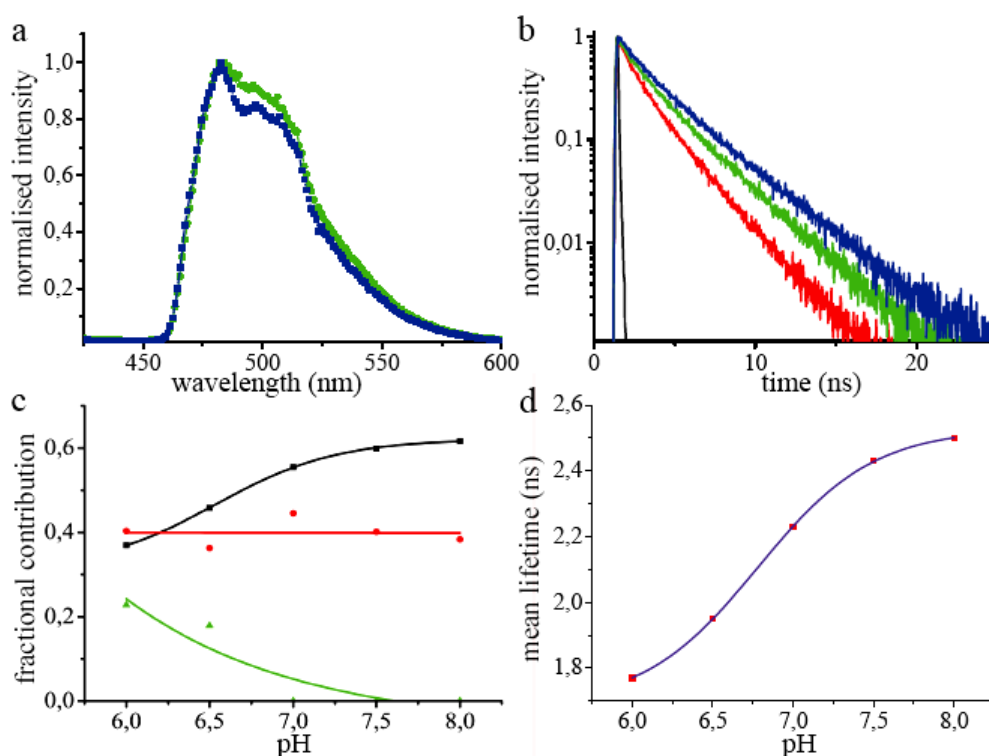
Fig. 4.1.1 *The fluorescence characteristics of purified CFP in solution at 420 nm excitation under varying pH conditions (6.0-8.0 at 0mM Cl⁻). a) Comparison of fluorescence emission spectra of CFP at pH 6.5 (green) and at pH 7.5 (blue). The emission maxima were observed at 486 nm irrespective of the pH levels, though a difference in the contribution of the 2nd emission peak at 505 nm was observed. b) The fluorescence decays of CFP at pH 6.0 (red), 6.5 (green) and 8.0 (blue). IRF is shown in black. c) The contributions of the lifetimes, τ_1 (black), τ_2 (red) and τ_3 (green) at the CFP emission maximum were calculated from the pre-exponential factors and plotted as normalised fractional contributions as a function of pH. d) Mean lifetimes at the donor emission maximum were plotted as a function of pH.*

4.1.1.1 Fluorescence dynamics of CFP in solution

The fluorescence emission maximum of purified CFP was observed at 486 nm, which was stable under varying pH (6.0-8.0) and chloride conditions (0-500mM) (Fig. 4.1.1a). The pH levels were varied in the absence of chloride. With lowering of pH levels, the contribution

of the red shifted shoulder of CFP at 505 nm was found to increase. The fluorescence decay of CFP was biexponential at pH levels >7.0, with lifetimes of 3.26±0.10 ns (τ_1) and 1.12±0.03 ns (τ_2). The multiple lifetimes of CFP at pH 7.4 (0mM Cl⁻) were 3.21 ns (τ_1) and 1.04 ns (τ_2). The presence of a third short lifetime component of 0.28±0.06 ns (τ_3) was observed at acidic pH levels with τ_1 and τ_2 changed to 3.09±0.09 ns and 1.38±0.08 ns, respectively. These differences significantly affected the overall fluorescence decay of CFP (Fig. 4.1.1b). The DAS of CFP confirmed the source of the third lifetime to be the CFP chromophore, with the spectral spread of the pre-exponential factors of all the lifetimes being similar. The plot of fractional contributions of CFP revealed significant quenching of τ_1 at acidic pH levels, whereas τ_2 remained unaffected (Fig. 4.1.1c). This resulted in an overall increase in the mean lifetime of CFP with increasing pH (Fig. 4.1.1d). The relatively chloride insensitive CFP showed only minimal effects on increasing the chloride in solution. A small increase in the donor mean lifetime from 2.36 ns to 2.49 ns was observed on increasing the chloride levels from 0mM to 500mM, which could be explained by the minor variations in the buffer pH levels. The results showed that the fluorescence dynamics of CFP was significantly affected by pH, in contrast to chloride.

4.1.1.2 Fluorescence dynamics of ECFP in hippocampal neurons

To determine the suitability of ECFP as donor at different maturational stages, living hippocampal neurons expressing the construct were measured at three different stages, namely DIV 7, 10 and 15. ECFP showed the emission maximum at 486 nm (Fig. 4.1.2a) irrespective of the developmental stage of cells, though a difference in the contribution of its second emission peak at 505 nm was observed with development.

The fluorescence decay of ECFP measured at DIV 7 was fit with three lifetime components of 3.39±0.04 ns (τ_1), 1.4±0.13 ns (τ_2) and 0.29±0.04 ns (τ_3) showing comparable contributions (n=3, Table 4.1.1, Fig. 4.1.2b). The DAS revealed a similar spectral spread for all the three lifetimes (Fig. 4.1.2c). The fractional contributions of the lifetimes showed minor changes along the spectra (Fig. 4.1.2e). The mean lifetime of ECFP at its emission maximum was 1.76±0.13 ns, which remained constant along the spectra.

At DIV 10, ECFP still displayed a three exponential decay, though with a slight difference in the individual lifetimes as well as their contributions (n=5, Table 4.1.1). The contribution of τ_1 was increased with a simultaneous reduction for τ_3, compared to DIV 7. The contribution of τ_2 remained unchanged. DAS was also similar for the two stages. The mean lifetime of ECFP at DIV 10 was increased to 1.97±0.10 ns (Table 4.1.1), though its spectral spread was similar to that observed at DIV 7.

At DIV 15, the total cell population was split up into two categories based on their intensity decays, group I (n=4) displaying a three exponential decay similar to DIV 7 and DIV 10, whereas group II (n=6) showed a typical biexponential fit of ECFP (Fig. 4.1.2b) with lifetime components of 3.30±0.02 ns (τ_1) and 1.08±0.04 ns (τ_2) (Table 4.1.1). DAS was also similar for both the categories compared to the previous stages, with the exception of the absence of τ_3 for the neurons belonging to group II (Fig. 4.1.2d). The fractional contribution of τ_1 reduced along the spectra with a simultaneous increase for τ_2 (Fig. 4.1.2f). The mean lifetimes of ECFP at the emission maximum were 1.96±0.15 ns and 2.38±0.03 ns for the first and second categories, respectively, with their spectral spread similar to those at younger stages (Table 4.1.1). Comparison of mean lifetimes of CFP for the two groups of cells with those of purified protein at different pH levels revealed the pH levels for group I to be 6.5 and that of group II to be 7.3, consistent with the previous reports (Bevensee et al., 1996). DAS of ECFP at all stages of neuronal development showed only positive values for the pre-exponential factors of the multiple lifetimes (Figs. 4.1.2c, d).

Table 4.1.1 Fluorescence emission dynamics of ECFP at different maturational stages of hippocampal neurons

Cell	DIV	group	n	τ_1(ns)	τ_1 (%)	τ_2(ns)	τ_2 (%)	τ_3(ns)	τ_3 (%)	τ_{mean}(ns)
Neurons	7	-	3	3.39 ±0.04	35 ±3	1.4 ±0.13	35 ±1	0.29 ±0.04	30 ±4	1.76 ±0.13
	10	-	5	3.36 ±0.05	44 ±3	1.36 ±0.07	33 ±1	0.19 ±0.03	23 ±3	1.97 ±0.10
	15	I	4	3.45 ±0.14	37 ±2	1.50 ±0.26	34 ±5	0.23 ±0.14	28 ±3	1.96 ±0.15
	15	II	6	3.30 ±0.02	59 ±1	1.08 ±0.04	41 ±1	-	-	2.38 ±0.03
COS-7	-	-	5	3.26 ±0.05	57 ±1	1.06 ±0.03	43 ±1	-	-	2.31 ±0.05

The multiple lifetimes and individual contributions of ECFP are shown at different stages of neuronal development. The percentage of contributions of τ_1, τ_2 and τ_3 are denoted as τ_1%, τ_2% and τ_3%, respectively. n denotes the number of measured cells. A significant fraction of cells at DIV 15 (group II) displayed biexponential fluorescence decay for ECFP in contrast to young stages. COS-7 cells showed lifetimes and contributions similar to those of group II at DIV 15.
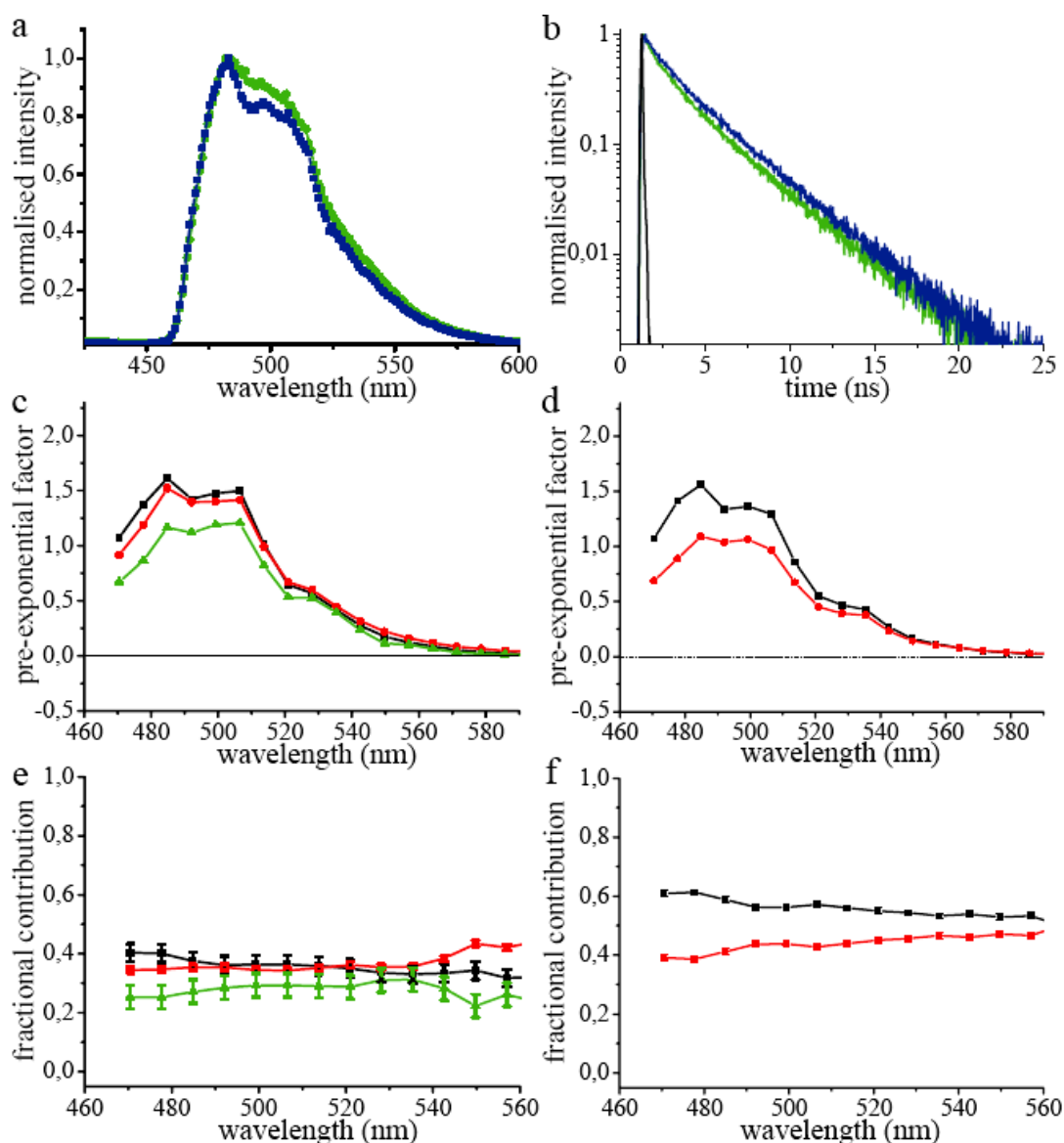
Fig. 4.1.2 *The fluorescence emission dynamics of ECFP at 420 nm excitation in hippocampal neurons. a) Comparison of fluorescence emission spectra of ECFP at DIV 7 (green) with DIV 15 (blue). The fluorescence maxima were observed at 486 nm, though a difference in the contribution of the 2nd peak at 505 nm was observed. b) Comparison of fluorescence decays of ECFP at DIV 7 (green) with DIV 15 (blue). The former was fit by a three exponential model, whereas the majority of cells at DIV 15 displayed only two lifetimes (Table 4.1.1). IRF is shown in black. c) DAS of ECFP at DIV 7. Intensity decays were analysed in 18 emission bands from 470 nm to 590 nm and the pre-exponential factors of lifetimes, τ_1 (black), τ_2 (red) and τ_3 (green) were plotted along the wavelength. d) DAS of biexponential ECFP at DIV 15. The pre-exponential factors of lifetimes, τ_1 (black) and τ_2 (red) were plotted along the wavelength. The normalised fractional contributions of lifetimes, τ_1 (black), τ_2 (red) and τ_3 (green) were plotted along the wavelength for DIV 7 (e) and DIV 15 (f).*

The decay kinetics of ECFP was measured in COS-7 cells to check for cell to cell variability of lifetimes. In this case, the decays were fit using a two exponential model of 3.26 ± 0.05 ns and 1.06 ± 0.03 ns, yielding mean lifetime of 2.31 ± 0.05 ns at its emission peak (n=5, Table 4.1.1). The fluorescence dynamics of the popular donor probe ECFP, previously assumed to be insensitive to developmental changes, was altered with maturation of hippocampal neurons.

4.1.2 Investigation of photophysics of Clomeleon along neuronal development

Clomeleon is a ratiometric indicator for chloride with CFP and Topaz separated by 24 amino acids. Since the donor CFP was observed to be significantly affected by pH, a detailed comparison of the fluorescence emission dynamics of the donor alone (CFP) and of the FRET sample (Clomeleon) individually under varying chloride and pH conditions was essential for a clear understanding of its photophysics. Clomeleon was digested with a protease capable of efficiently cleaving it into individual CFP and Topaz molecules. The study of the digested sample under the varying foresaid conditions allowed a better understanding of the effects on single CFP and Topaz fluorophores making the construct. The reliability of the measurements was verified by molecular modelling. The observations were compared with the calcium indicator Cameleon, containing a chloride insensitive acceptor with a similar donor, at different stages of maturation of hippocampal neurons.

4.1.2.1 Fluorescence characteristics of Clomeleon in solution

a) **Varying chloride levels**

Purified Clomeleon was measured by varying the chloride concentrations from 0-50mM, 100mM, 250mM and 500mM, at pH 7.4. The fluorescence emission spectra revealed emission maxima for CFP and Topaz at 486 nm and 527 nm, respectively. The intensity ratios of Topaz to CFP at their emission peaks, measured as R, were plotted for the corresponding chloride concentrations (Fig. 4.1.3a) with values ranging from 1.7 for 0mM down to 0.8 and 0.5 for 50mM and 500mM Cl$^-$, respectively. R values reduced exponentially with increasing chloride concentrations, which saturated above 100mM (Fig. 4.1.3a). The fluorescence decay of Clomeleon at varying chloride concentrations in solution was fit by a three exponential model with lifetimes of 3.37±0.02 ns (τ_1), 1.33±0.03 ns (τ_2) and 0.21±0.02 ns (τ_3), except for 0mM Cl$^-$ which showed 2.82 ns (τ_1), 0.97 ns (τ_2) and 0.21 ns (τ_3). Though the lifetimes of Clomeleon were not changed on varying the chloride concentrations (>0mM), differences in the fractional contributions of the individual lifetimes were observed. The contribution of τ_1 increased with increasing chloride concentrations from 18% to 41% at the donor emission maximum, whereas that of τ_3 decreased from 43% to 25% at the same. τ_2 showed a slight change in its contribution from 39% to 34%. The plots of all the three lifetime contributions on varying the chloride concentrations were fit with single exponential functions ($y_0+A_1e^{(x/t_1)}$) (Fig. 4.1.3c). Consequently, the Stern-Volmer plot displayed a drastic increase in the donor mean lifetimes on increasing the chloride levels (Fig. 4.1.3e). At the acceptor emission maximum, a reverse effect was observed where the contribution of τ_1 decreased from 89% to 66% with a simultaneous increase in contributions of τ_2 and τ_3 from 9% and 2% to 22% and

12%, respectively. This resulted in an exponential decrease in the acceptor mean lifetime of Clomeleon from 3.15 ns to 2.54 ns on increasing the chloride concentrations.

b) Varying pH levels

Purified Clomeleon was measured at different pH levels in the physiological range from 6.0-8.0.
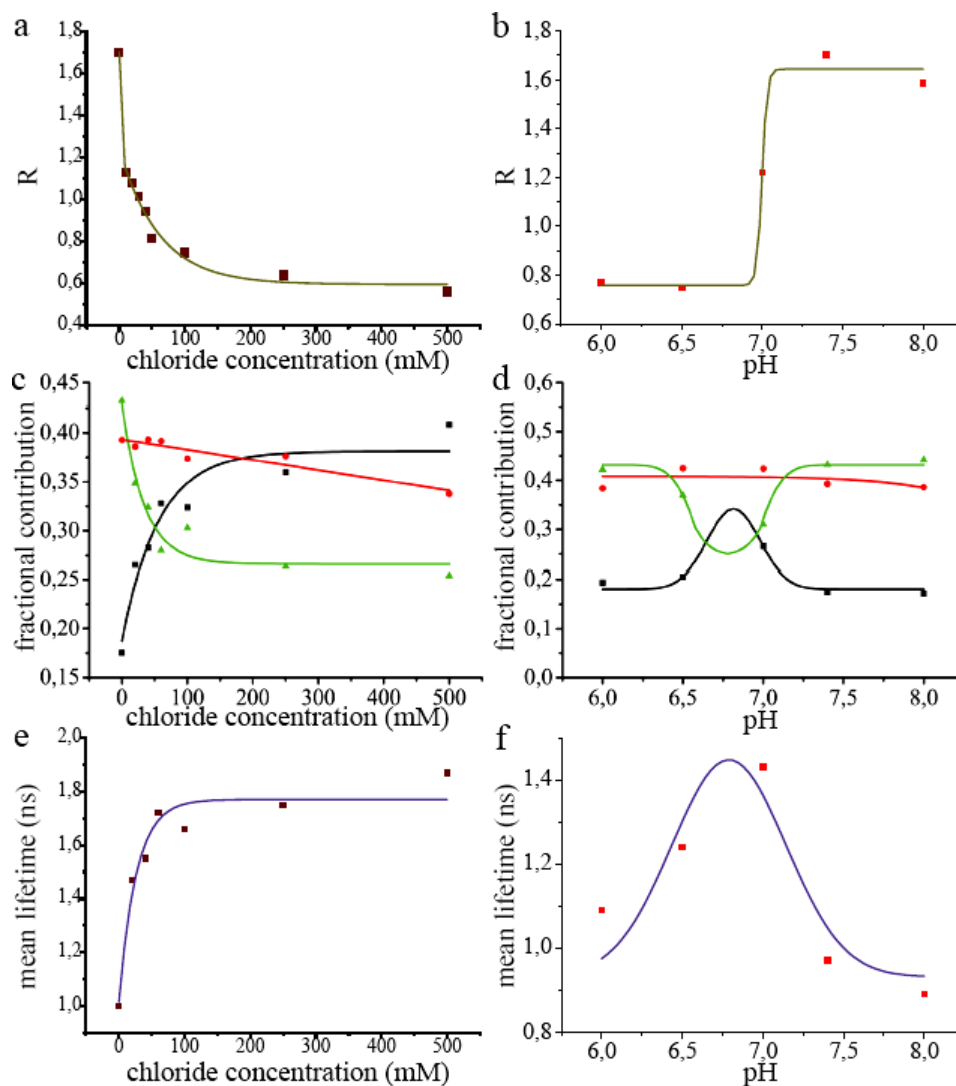
Fig. 4.1.3 *Fluorescence properties of purified Clomeleon in solution under varying chloride and pH conditions. a) R values (intensity ratios of Topaz to CFP emission maxima) of purified Clomeleon at different chloride concentrations (pH 7.4). R values reduced exponentially on increasing the chloride concentrations. b) R values of purified Clomeleon at different pH levels (0mM Cl$^-$). R values reduced drastically at acidic pH levels. c-d) The normalised fractional contributions of lifetimes, τ_1 (black), τ_2 (red) and τ_3 (green) at the donor emission maximum were plotted with increasing chloride concentrations (c) and as a function of pH (d). The contributions of τ_1 and τ_3 were highly affected in contrast to τ_2, in both the cases. e) The mean lifetimes of Clomeleon at the donor emission maximum increased exponentially with increasing chloride concentrations, yielding the Stern-Volmer plot. f) The donor mean lifetimes of Clomeleon were significantly reduced due to high quenching effects at acidic pH levels (<7.0) as well as due to FRET at higher pH levels (>7.0), resulting in a Gaussian distribution with a mean value of 6.9.*

At 0mM Cl$^-$, *R* values significantly decreased from 1.64±0.08 (pH>7.0) to 0.76±0.01 on lowering the pH levels (pH<7.0) (Fig. 4.1.3b). The fluorescence decay of Clomeleon was fit with three lifetimes at all pH conditions. Lifetimes of 3.09±0.07 ns (τ_1), 1.20±0.08 ns (τ_2)

and 0.19±0.06 ns (τ_3) were observed at pH<7.0, which changed to 2.84 ±0.03 ns (τ_1), 0.93±0.06 ns (τ_2) and 0.17±0.06 ns (τ_3) at higher pH levels (>7.0). The contributions of the individual lifetimes were affected on varying the pH, with τ_1 decreasing significantly at acidic pH levels (<7.0) as well as at higher pH conditions (>7.0) with a simultaneous increase of τ_3 for the same, whereas minor deviations were observed for τ_2 (Fig. 4.1.3d). Consequently, the donor mean lifetimes showed a Gaussian distribution with a mean value of 6.9, on varying the pH conditions (Fig. 4.1.3f). A reverse effect for the fractional contributions of the acceptor lifetimes was observed on varying the pH levels. The contributions of τ_1 increased around pH 6.9 with a simultaneous decrease for τ_2 and τ_3 at the same, resulting in an increase in the acceptor mean lifetime from 1.80 ns to 2.94 ns. The fluorescence dynamics of Clomelon was drastically affected by pH and chloride, with FRET decreasing both at high chloride concentrations and low pH levels.

4.1.2.2 Clomeleon in the presence and absence of rTEV protease

Purified Clomeleon was digested with rTEV protease which recognised the ENLYFQG sequence at the centre of the linker connecting the CFP and Topaz fluorophores. This yielded the double band at ~28 kDa instead of the 57 kDa band of undigested Clomeleon, in the Western Blot (Fig. 4.1.4c). A cleavage of >90% for Clomeleon was observed after digestion. The fluorescence spectra as well as decay of Clomeleon were altered on protease digestion (Figs. 4.1.4a, b). There was no Topaz enhancement due to lack of FRET and very low direct excitation (Fig. 4.1.4a). The R value of purified Clomeleon at 0mM Cl⁻ (pH 7.4) was measured to be 1.7, which reduced to 0.42 in presence of the protease.

The change in the resulting fluorescence decay from three to two exponentials with similar lifetimes of CFP (pH 7.4) confirmed the absence of any undigested sample (Figs. 4.1.4b, d, e). The fluorescence decay of Clomeleon after protease digestion was fit with lifetime components of 3.43±0.02 ns (τ_1) and 1.02±0.02 ns (τ_2), irrespective of the chloride concentration used. The slight increase in the individual lifetimes compared to CFP can be explained by the direct excitation of Topaz. Compared to the undigested Clomeleon at 0mM Cl⁻ and pH 7.4, at the donor emission maxima, the contribution of τ_1 was increased to 64% from 18% whereas that of τ_2 slightly reduced to 36% from 39% on digestion. Consequently, the overall donor fluorescence decay of the digested sample was longer compared to the undigested control (Fig. 4.1.4b). At 0mM Cl⁻, DAS of undigested Clomeleon displayed negative pre-exponential factors of τ_3 (Fig. 4.1.4d) in contrast to the positive amplitudes observed for all the lifetimes after digestion (Fig. 4.1.4e), similar to CFP, indicating the

absence of energy transfer in presence of single CFP and Topaz molecules in the same stoichiometry.
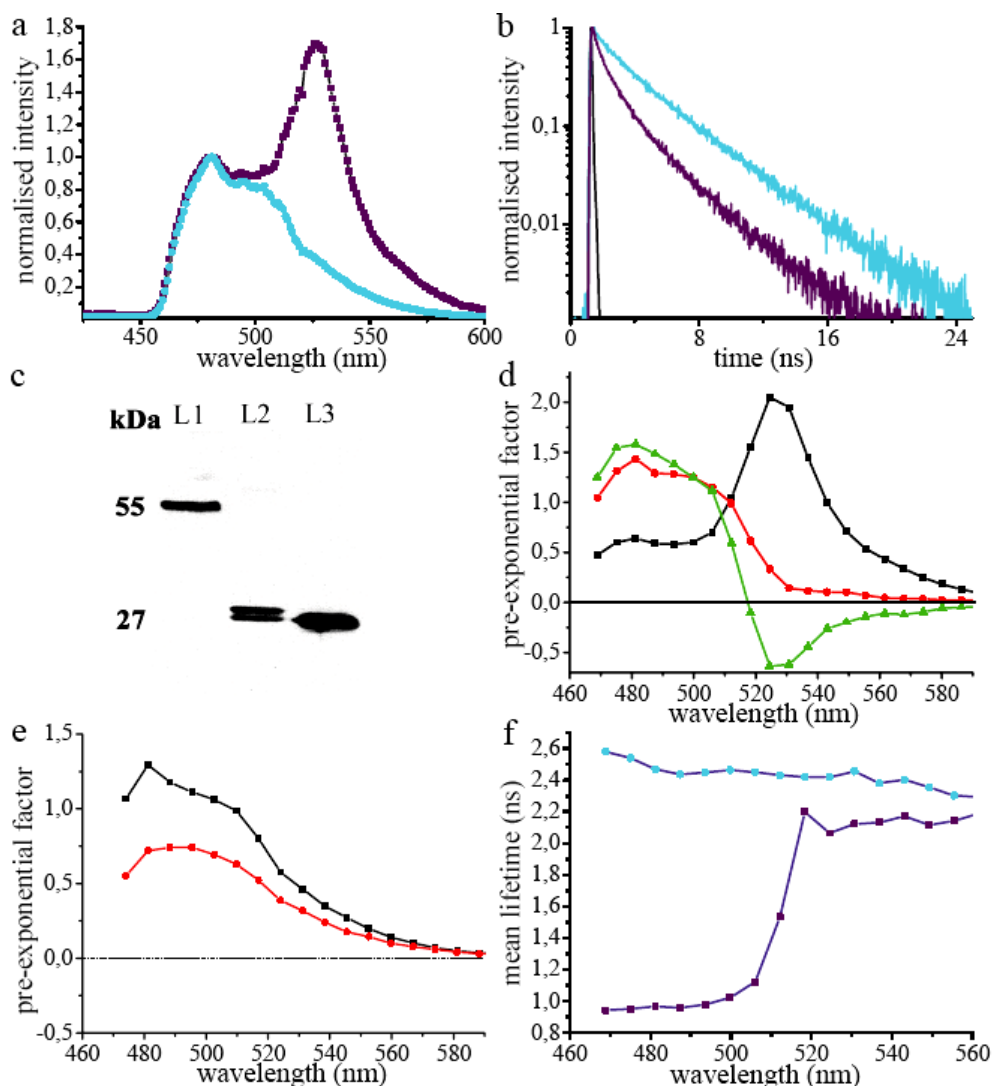
Fig. 4.1.4 *The fluorescence emission dynamics of purified Clomeleon before and after protease digestion. a) Comparison of fluorescence emission spectra of Clomeleon before (purple) and after (cyan) protease digestion. The R value of Clomeleon at 0mM Cl⁻ and pH 7.4 was reduced from 1.7 to 0.42 on digestion. b) Comparison of the donor fluorescence decay of digested Clomeleon (cyan) with the undigested protein (purple). Decay of the digested sample was observed to be longer compared to the latter. c) Western blot showing the digested protein bands of 28 kDa (L2) compared to the undigested Clomeleon of 57 kDa (L1). Control GFP protein is shown in L3. d) DAS of undigested Clomeleon. The pre-exponential factors of τ_3 (green) displayed negative values at the acceptor emission maximum. e) DAS of Clomeleon after protease digestion. The pre-exponential factors of τ_1 (black) and τ_2 (red) were positive, similar to CFP. f) Mean lifetimes of undigested (purple spots) and digested Clomeleon (cyan spots).*

The contributions of the individual lifetimes also exhibited differences in their spectral spread. For the undigested FRET sample, τ_1 showed a significant increase in its contribution along the spectra with a simultaneous decrease for τ_2 and τ_3. This was in contrast to the digested Clomeleon, which revealed no changes along the spectra. Consequently, after protease digestion the mean lifetime at the donor emission maximum increased from 0.97 ns to 2.54 ns similar to CFP (Fig. 4.1.4f). Only a minor increase in the donor mean lifetime from 2.54 ns to 2.63 ns was observed on increasing the chloride concentrations from 0mM to

500mM for the digested sample. On varying the pH levels for the digested sample, similar changes as that observed for CFP alone were observed with no additional contributions in the acceptor channels. FRET was completely absent for the protease digested Clomeleon, with its fluorescence dynamics similar to CFP on varying the chloride and pH levels.

4.1.2.3 Modelling of Clomeleon

Using τ_1 of purified CFP (0mM Cl⁻, pH 7.4) of 3.21 ns, which is most affected by quenching, as the unperturbed donor lifetime in the absence of acceptor (τ_D) and τ_3 of purified Clomeleon of 0.21 ns (0mM Cl⁻, pH 7.4) as the perturbed lifetime of donor in presence of the acceptor or the FRET lifetime (τ_{DA}), the intramolecular distance between the CFP-Topaz chromophores in Clomeleon was calculated. R_0 was fixed to be 4.92 nm for CFP-YFP pairs (Patterson et al., 2000) and a random orientation of dipole moments with $\kappa^2=2/3$ was assumed. This yielded a FRET efficiency of 94%, which resulted in the inter-chromophore distance r to be 3.2 nm.
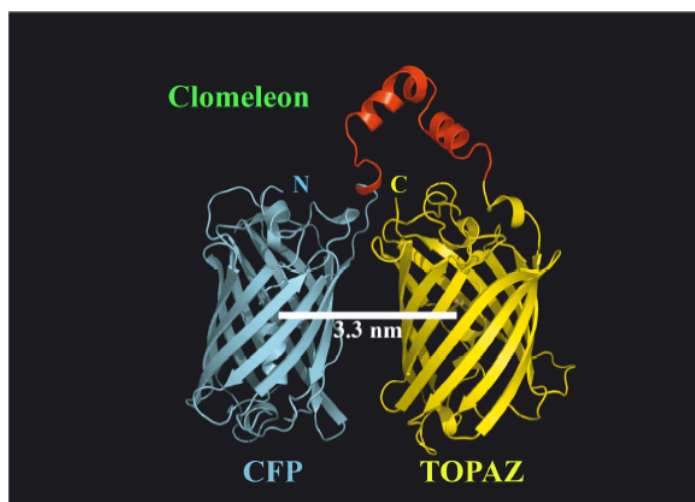
Fig. 4.1.5 *Molecular modelling of Clomeleon. The fluorescent domains, CFP (cyan) and Topaz (yellow) were set in parallel orientation since N- and C-terminal ends of either domain were on the same site. The intramolecular distance between CFP and Topaz chromophores was calculated to be 3.3 nm. A more compact anti-parallel or cross-like orientation with distances close to 2.6 nm as found in homologue experimental structures sterically hindered the placement of the rTEV site containing linker without unfolding the adjacent helices of the fluorescent domains. Taken from (Jose et al., 2007b).*

Since there was equal probability for the FRET lifetime of 0.21 ns to be arising from the quenching of τ_2 of CFP (1.04 ns), such a calculation yielded the efficiency to be 80% and consequently the distance r to be 3.9 nm. Both the calculated distances were in agreement with the theoretically calculated values from molecular modelling of 3.3 nm (Fig. 4.1.5).

4.1.2.4 Fluorescence dynamics of Clomeleon at different developmental stages of
hippocampal neurons

To get an overall understanding of the changes in the intracellular chloride concentrations of neurons during maturation, the biophysical properties of the ratiometric

indicator Clomeleon were studied at three different developmental stages of neurons, namely DIV 7, 10 and 15 (Table 4.1.2). The fluorescence emission spectra of Clomeleon at all stages showed the CFP emission maximum at 486 nm and the corresponding Topaz emission at 527 nm (Figs. 4.1.6a, 4.1.7a). Neurons were classified based on individual Topaz to CFP intensity ratios at their emission peaks (R) into class I, class II and class III with R values of 0.4-0.8, 0.8-1.2 and 1.2-1.6, respectively.

Table 4.1.2 Fluorescence emission dynamics of Clomeleon at different stages of hippocampal neuronal development

Cell	DIV	n	Class	R	τ_1(ns)	τ_1(%)	τ_2(ns)	τ_2(%)	τ_3(ns)	τ_3(%)	τ_{mean}(ns)
Neurons	7	5	I	0.42 ±0.04	3.39 ±0.05	40 ±2	1.35 ±0.06	33 ±1	0.26 ±0.03	27 ±2	1.86 ±0.07
	10	7	I	0.47 ±0.06	3.35 ±0.08	45 ±3	1.38 ±0.16	32 ±3	0.24 ±0.13	23 ±2	2 ±0.10
	10	4	II	1.07 ±0.08	3.40 ±0.02	34 ±1	1.36 ±0.05	33 ±2	0.21 ±0.03	33 ±2	1.68 ±0.04
	15	4	I	0.62 ±0.08	3.46 ±0.07	39 ±4	1.33 ±0.09	32 ±2	0.21 ±0.08	29 ±5	1.84 ±0.15
	15	9	II	1.04 ±0.11	3.40 ±0.01	35 ±2	1.38 ±0.06	35 ±2	0.24 ±0.04	31 ±2	1.73 ±0.08
	15	6	III	1.32 ±0.09	3.39 ±0.03	30 ±1	1.37 ±0.01	34 ±2	0.19 ±0.03	35 ±2	1.57 ±0.01
COS-7	-	5	-	1.05 ±0.18	3.40 ±0.02	32 ±2	1.32 ±0.05	36 ±1	0.17 ±0.01	32 ±2	1.61 ±0.06

The multiple lifetimes of Clomeleon were consistent along development, though a difference in the contributions of the individual lifetimes was observed. The population of cells in each class is shown as n. The percentage of contributions of τ_1, τ_2 and τ_3 are denoted as τ_1%, τ_2% and τ_3%, respectively. The mean lifetimes for the respective classes at each stage are denoted as τ_{mean}. Comparison of lifetimes and contributions obtained from COS-7 cells showed that they were similar to class III at DIV 15.

The fluorescence spectra of Clomeleon at DIV 7 revealed a quenched Topaz emission relative to CFP (Fig. 4.1.6a), with cells falling into class I of R values in the range of 0.42±0.04 (n=10). A representative cell is shown in Fig. 4.1.6c. The fluorescence decay of Clomeleon at this stage was fit by a three exponential model with lifetimes of 3.39±0.05 ns (τ_1), 1.35±0.06 ns (τ_2) and 0.26±0.03 ns (τ_3), with the maximum contribution observed for τ_1

at the donor emission peak (n=5, Table 4.1.2). The overall donor fluorescence decay of Clomeleon at this stage did not show a considerable difference from that of control ECFP (Fig. 4.1.6b). DAS exhibited only positive values for the pre-exponential factors of all the lifetimes (Fig. 4.1.6d). The fractional contributions of the multiple lifetimes did not show a significant change along the wavelength axis from the donor to the acceptor (Fig. 4.1.6e). The lifetimes, τ_1, τ_2 and τ_3 displayed contributions of 46±3%, 31±2% and 24±1% at the acceptor emission maximum, similar to the donor. Consequently, the mean lifetime at the donor emission peak of 1.86±0.07 ns showed only minor changes up to 2.01±0.08 ns at the acceptor emission maxima (Fig. 4.1.6f).
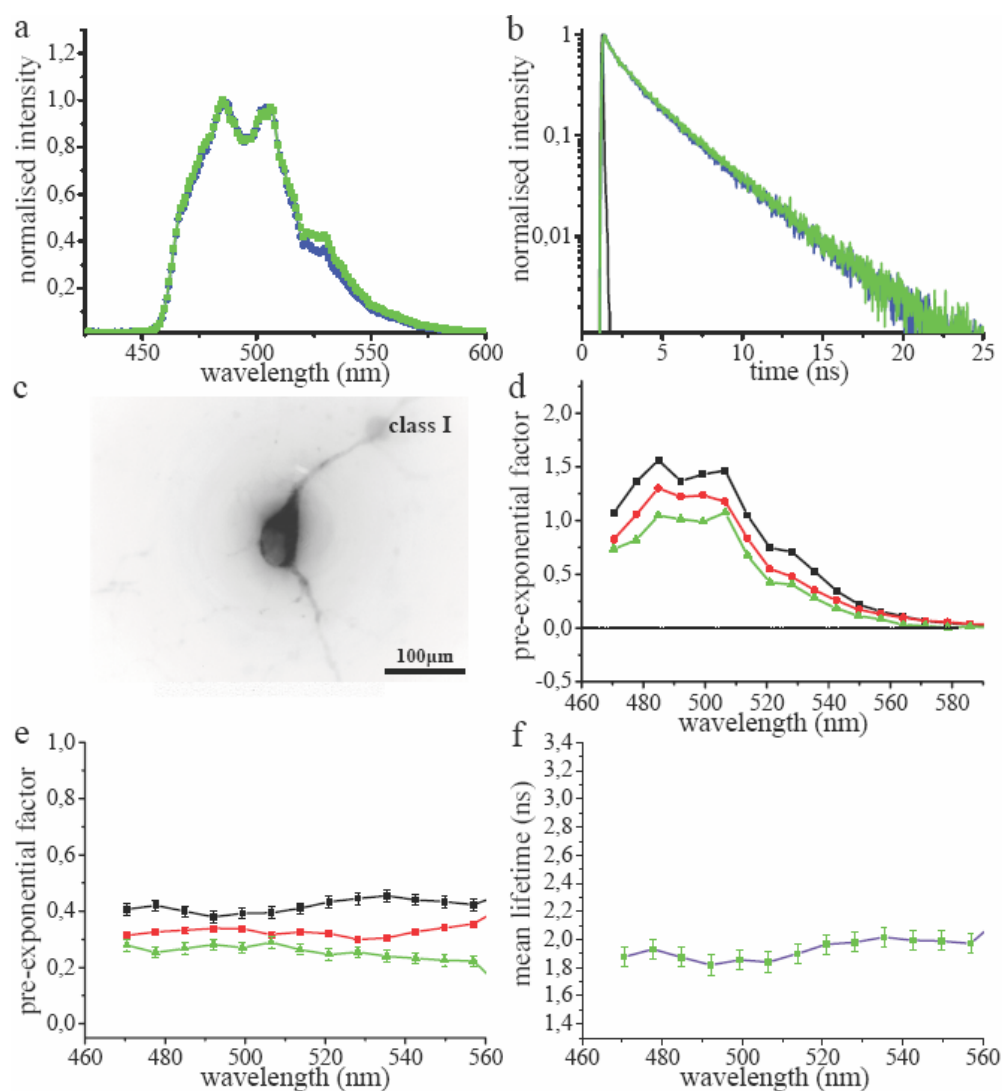
Fig. 4.1.6 *The fluorescence emission dynamics of Clomeleon at 420 nm excitation in hippocampal neurons at DIV 7. a) Comparison of fluorescence emission spectra of ECFP (blue) with Clomeleon (green) at DIV 7. b) Fluorescence decay of Clomeleon at the donor emission maximum at DIV 7 (green) compared to ECFP (blue). IRF is shown in black. The fluorescence decay of Clomeleon was fit by a three exponential model (Table 4.1.2). c) A representative image of a neuron at DIV 7. d) DAS of Clomeleon at DIV 7. The pre-exponential factors of τ_1 (black), τ_2 (red) and τ_3 (green) were positive similar to ECFP. e) The normalised fractional contributions of the lifetimes, τ_1 (black), τ_2 (red) and τ_3 (green) were plotted along the wavelength. f) The mean lifetime of each emission band was plotted along the wavelength. The variability between the cells is shown by error bars.*

At DIV 10, the majority of neurons were categorised into classes I (n=7) and II (n=4) with R values of 0.47±0.06 and 1.07±0.08, respectively (Table 4.1.2). Other classes with cells less than 10% of the total population were not considered in the classification. The fluorescence decay of Clomeleon at DIV 10 revealed similar lifetimes as DIV 7, but with the individual contributions of the lifetimes varying among the different classes (Table 4.1.2). At the donor emission maximum, τ_1 showed a significant decrease in its contribution from class I to II with a simultaneous increase of τ_3 for the same (Table 4.1.2). τ_2 displayed similar contributions for both the classes. Thus, the donor kinetics of Clomeleon in neurons belonging to class II revealed a shorter decay compared to control ECFP, in contrast to class I. DAS displayed negative values for the pre-exponential factors corresponding to τ_2 and τ_3 for class II, in contrast to the unaffected positive values of class I. A reverse effect was observed at the acceptor emission maximum for class II, where τ_1 showed the maximum contribution of 87±7% with the contributions of τ_2 and τ_3 being <10%. For class I, the contribution of τ_1 decreased to 67±8% with a corresponding increase in the contributions of τ_2 and τ_3 to 20±6% and 14±5%, at the acceptor emission peak, respectively. Thus, for class II, the fractional contributions of the individual lifetimes revealed a drastic increase for τ_1 along the spectra with a simultaneous decrease for τ_2 and τ_3. Such a significant change was not observed for class I. This resulted in donor mean lifetimes of 2.00±0.10 ns and 1.68±0.04 ns (Table 4.1.2) which increased to 2.54±0.21 ns and 3.08±0.20 ns at the acceptor emission maxima, for classes I and II respectively.

At DIV 15, neurons were divided into three classes, namely class I (n=4), class II (n=9) and class III (n=6) with R values of 0.62±0.08, 1.04±0.11 and 1.32±0.09, respectively (Table 4.1.2, Fig. 4.1.7a). The multiple lifetimes of Clomeleon in this case were similar to those at DIV 7 and DIV 10 (Table 4.1.2). The contributions of the individual lifetimes at the donor emission maximum were similar to DIV 10 for classes I and II, whereas class III showed lower and higher contributions of τ_1 and τ_3, respectively (Table 4.1.2). Consequently, the donor fluorescence decays of classes II and III were shorter compared to class I as well as to control ECFP (Fig. 4.1.7b, Table 4.1.2). DAS displayed negative values for the pre-exponential factors of τ_2 and τ_3 for classes II and III (Fig. 4.1.7g) at DIV 15, in contrast to class I (Fig. 4.1.7d). The fractional contributions of τ_2 and τ_3 showed drastic decrease over the spectra with a simultaneous increase of τ_1 for these two classes (Fig. 4.1.7h), in contrast to class I of the same maturation stage (Fig. 4.1.7e). For classes II and III, at the acceptor emission peak, the major contributions were observed for τ_1 of 89±5% and 92±2%, respectively, with τ_2 and τ_3 contributing less than 10%. This was in contrast to class I where

the corresponding contributions of τ_1, τ_2 and τ_3 were 64±7%, 21±3% and 15±5% at the acceptor emission maximum, respectively. As a result, the donor mean lifetimes for the classes I-III of 1.84±0.15 ns, 1.73±0.08 ns and 1.57±0.01 ns (Table 4.1.2) increased to 2.53±0.19 ns, 3.08±0.13 ns and 3.21±0.01 ns, respectively, at the acceptor emission peak (Figs. 4.1.7f, i).
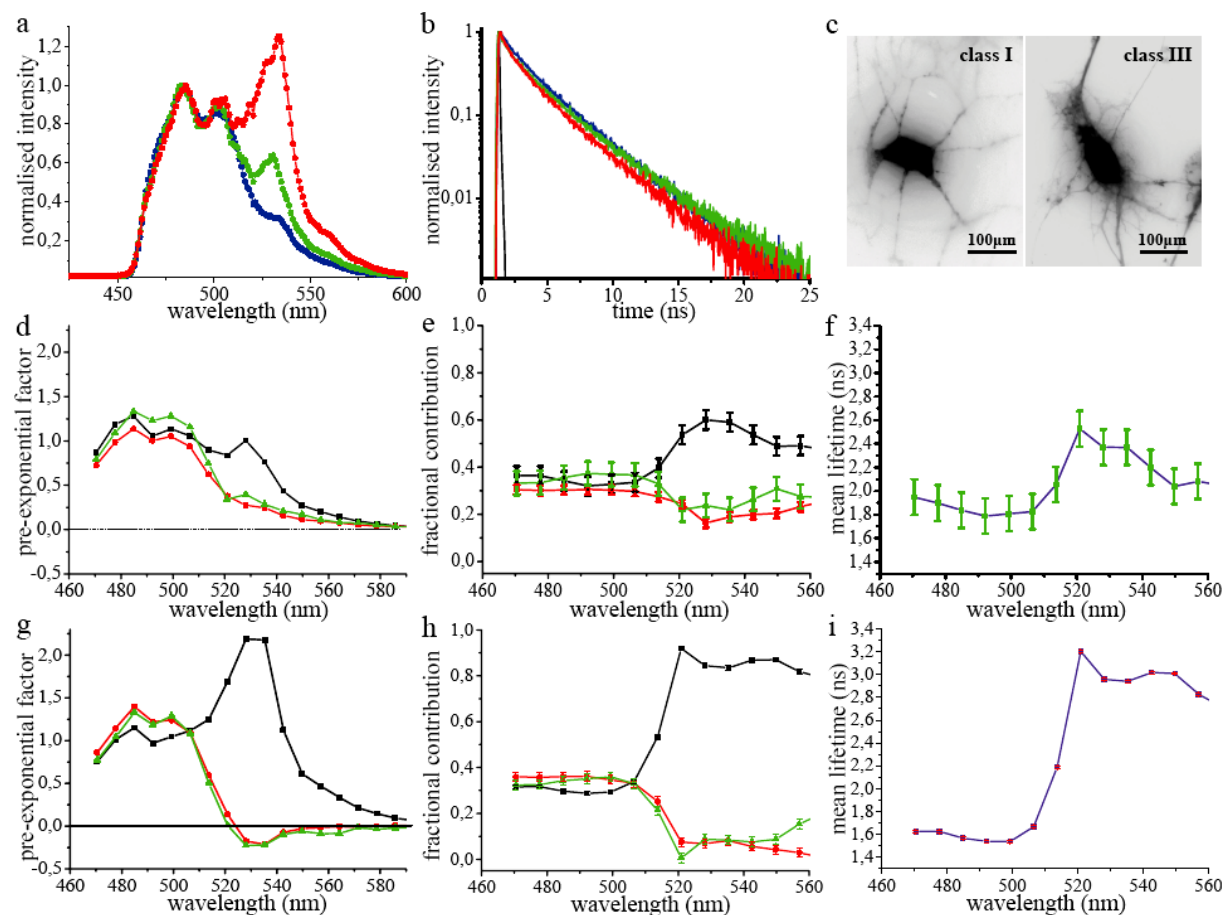
Fig. 4.1.7 *The fluorescence emission dynamics of Clomeleon at 420 nm excitation in hippocampal neurons at DIV 15. a) Comparison of fluorescence emission spectra of ECFP (blue) with Clomeleon of classes I (green) and III (red) with R values of 0.65±0.07 and 1.23±0.04, respectively. b) Fluorescence decays of Clomeleon at the donor emission maxima of classes I (green) and III (red) at DIV 15 compared to ECFP (blue). IRF is shown in black. c) Representative images of neurons belonging to classes I and III at DIV 15. The neurons of class III were more developed compared to those of class I. d, g) DAS of Clomeleon of classes I and III. The pre-exponential factors of τ_1 (black), τ_2 (red) and τ_3 (green) were positive, similar to ECFP, for class I (d) in contrast to the negative values displayed by τ_2 (red) and τ_3 (green) of class III (g). e, h) The normalised fractional contributions of the lifetimes, τ_1 (black), τ_2 (red) and τ_3 (green) were plotted along the wavelength for classes I (e) and III (h). f, i) Mean lifetimes of each emission band of classes I (f) and III (i) were plotted along the wavelength. The variability between the cells is shown by error bars. For class III (red spots), the variability was lower compared to class I (green spots).*

Classification of neurons based on their *R* values revealed a shift in their numbers from classes of low *R* values to higher values with neuronal maturation, thereby indicating that the majority of neurons expressing Clomeleon exhibited energy transfer when they were mature. At similar developmental stages of neurons, a reduction in the donor mean lifetimes was observed for the classes I-III, whereas the acceptor mean lifetimes showed a

corresponding increase for the same. An overall decrease in the donor mean lifetimes with a simultaneous increase in the acceptor mean lifetimes was also perceived with maturation.
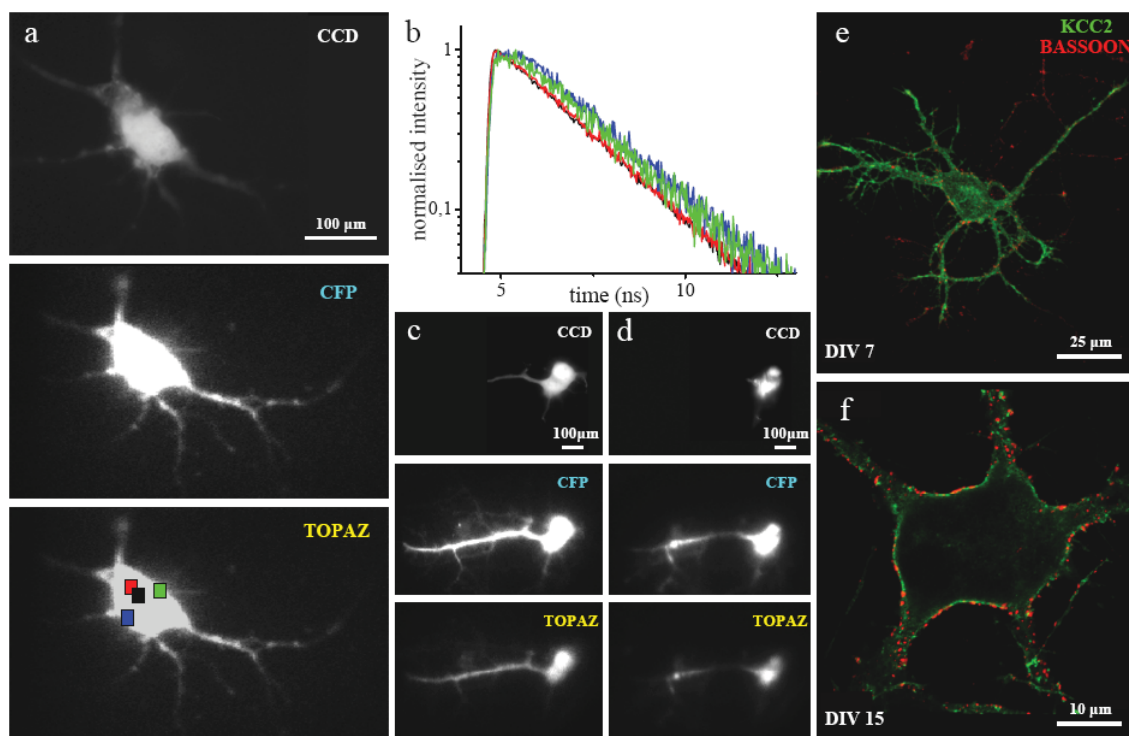
Fig. 4.1.8 *Mature neurons (DIV 15) expressing Clomeleon as observed using the imaging detector. a) The fluorescence emission was split up into CFP and Topaz emission bands as shown. A comparison with the corresponding fluorescence image from the CCD was done (top). Selected ROIs are shown as coloured squares. b) Analysis of the differential acceptor rise at different intracellular regions of a cell. A better rise in the acceptor dynamics was observed at the cell periphery (green, blue) compared to the cell centre (black, red). Comparison of cells in epifluorescence (c) and TIRF modes (d). Negative values for the pre-exponential factors of τ_3 were observed in the acceptor channel in the TIRF mode. Immunostainings against KCC2 (green) and Bassoon (red) were done to compare the maturity of cells at DIV 7 (e) and DIV 15 (f). At DIV 7, a higher intracellular staining of KCC2 was observed in contrast to that observed at DIV 15, where the majority of cells showed a clear enrichment of KCC2 at specific regions of the cell membrane. The synapses marked by Bassoon increased at DIV 15 (f) compared to DIV 7 (e).*

Along with studying the developmental changes in the intracellular chloride concentrations, the differences in the ionic concentrations at different intracellular compartments were compared at the level of single cells. In mature neurons (DIV 15) expressing Clomeleon, different regions of interest (ROIs) in the same cell displayed differences in the acceptor dynamics (Figs. 4.1.8a, b). A better rise was observed at ROIs close to the periphery of the cell compared to the cell centre, indicating better FRET for Clomeleon at the former. A confirmation of this was done using TIRF (Fig. 4.1.8d), which illuminated only the fluorophores close to the cell periphery. The lifetimes of Clomeleon by epifluorescence (Fig. 4.1.8c) and TIRF (Fig. 4.1.8d) excitations were 3.19 ± 0.01 ns (τ_1), 1.36 ± 0.03 ns (τ_2) and 0.34 ± 0.04 ns (τ_3). In the TIRF mode, τ_3 exhibited negative pre-exponential factors (<5%) in the acceptor channel. In the donor channel, τ_1, τ_2 and τ_3 displayed similar contributions in both the illumination modes of $31\pm2\%$, $37\pm1\%$ and $33\pm1\%$,

respectively. In the acceptor channel, similar to what was observed with the point detector, τ_1 showed the maximum contribution of 86% in the epifluorescence mode which increased to 94% in the TIRF mode. The contributions of τ_2 and τ_3 also decreased in the TIRF mode, though they were individually below 10%. Consequently, an increase in the acceptor mean lifetime from 2.88 ns to 3.10 ns was observed on changing from the epifluorescence to the TIRF mode (Figs. 4.1.8c, d).

The chloride transporter KCC2 shows an upregulation along neuronal development; the expression pattern of which has also been functionally linked with the shift of GABA mediated responses from depolarising to hyperpolarising (Ben-Ari, 2002). Immunostainings with antibodies against KCC2 and the presynaptic marker protein Bassoon were done for comparing the maturity of cells at individual stages (Figs. 4.1.8e, f). At DIV 7, a higher intracellular staining of KCC2 was observed (Fig. 4.1.8e). This was in contrast to those observed at DIV 15, where the majority of mature neurons showed a clear membrane staining with enrichment of KCC2 at specific regions of the cell membrane (Fig. 4.1.8f). The synapses marked by Bassoon also increased at DIV 15 compared to young neurons (Figs. 4.1.8e, f) and were observed between KCC2 enriched regions. This was in agreement with the previous reports where a higher expression of KCC2 was seen at the vicinity of excitatory inputs in the hippocampus, possibly in close association with the extrasynaptic GABA$_A$ receptors (Gulyas et al., 2001).

Overall changes in the fluorescence spectra, lifetimes, as well as in the contributions of individual lifetimes of Clomeleon were observed with development (Figs. 4.1.6-4.1.8). Mature neurons expressing Clomeleon revealed higher FRET efficiencies in contrast to young cells.

4.1.2.5 Effect of neuronal development on the fluorescence dynamics of the calcium indicator Cameleon

In order to study the effects of intracellular ionic concentrations on FRET for an independent construct with a less sensitive acceptor, Yellow Cameleon YC2.3 was monitored at different developmental stages (DIV 7, 10, 15) of hippocampal neurons. Cameleon consisted of tandem fusions of ECFP and a photostable YFP variant, Citrine. Binding of Ca^{2+} to Cameleon increased the efficiency of energy transfer between the flanking GFPs (Miyawaki et al., 1997). YC2.3 exhibited the fluorescence emission maximum for ECFP at 486 nm and for Citrine at 529 nm. At DIV 7, the total cell population was divided into two with R values of 1.04±0.12 and 1.55±0.27. The fluorescence decay was fit by a three exponential model with lifetime components of 3.26±0.1 ns (τ_1), 1.39±0.14 ns (τ_2) and

0.3±0.07 ns (τ_3) (n=9). The multiple lifetimes of Cameleon were in good agreement with the previous reports in solutions (Habuchi et al., 2002). DAS showed negative values for the pre-exponential factors of τ_2 and τ_3. τ_1 displayed a significant increase in its contribution with increasing wavelength, with a corresponding decrease for the short lifetime components. At DIV 10, R values similar to DIV 7 were observed (n=5). At DIV 15, R values of YC2.3 were reduced to 0.65±0.02. The fluorescence decay in this case was also fit by a three exponential model with lifetime components similar to the previous cases (n=5). No negative DAS was detected for any of the lifetimes at this stage. Cameleon showed FRET in young neurons where the intracellular calcium concentrations were high, in contrast to mature neurons.

4.1.3 Clomeleon as a ratiometric and lifetime indicator

The suitability of Clomeleon as a ratiometric and lifetime indicator along development of living neurons was ensured by independent methods. Ratiometric studies using chloride regulated COS-7 cells and lifetime measurements on purified solutions of Clomeleon were performed for the purpose.

4.1.3.1 Fluorescence dynamics of Clomeleon on regulating chloride concentrations

COS-7 cells expressing Clomeleon exhibited R values of 1.05±0.18. The fluorescence decay in this case was fit with three lifetimes of 3.40±0.02 ns, 1.32±0.05 ns and 0.17±0.01 ns showing comparable contributions at the donor emission maximum (n=5, Table 4.1.2). At the acceptor emission peak, the maximum contribution was observed for τ_1 of 88±2% with τ_2 and τ_3 contributing less than 10%. This resulted in an increase in the mean lifetime of Clomeleon from 1.61±0.06 ns to 3.10± 0.08 ns along the spectra, from the donor to the acceptor emission maxima.

COS-7 cells were clamped to three different chloride concentrations of 0mM, 30mM and 50mM maintaining the pH constant at 7.4, and the individual R values were calculated (Fig. 4.1.9a). Cells at 0mM Cl⁻ yielded R values of 1.59±0.18, which was reduced to 1.07±0.14 and 0.58±0.07 on increasing the chloride concentrations to 30mM and 50mM, respectively. Since the major influences on the Clomeleon fluorescence including chloride and pH were controlled using Tributyltin chloride (TBTC) and Nigericin, respectively, the changes in R values were concluded to be due to chloride changes. Comparing the R values from externally regulated COS-7 cells with those from hippocampal neurons, the intracellular chloride concentrations were calculated for the various fractions of neurons at different stages of maturation. A significant decrease in chloride concentrations along neuronal development was observed (Fig. 4.1.9b). The young neurons at DIV 7 showed intracellular chloride

concentrations of 58±3mM. At DIV 10, classes I and II revealed chloride concentrations of 56±3mM and 26±4mM, respectively, whereas classes I-III at DIV 15 exhibited chloride concentrations of 48±4mM, 28±6mM and 15±4mM, respectively. The calculated results were in agreement with the electrophysiological reports on overall changes of chloride during neuronal development (Kuner and Augustine, 2000).
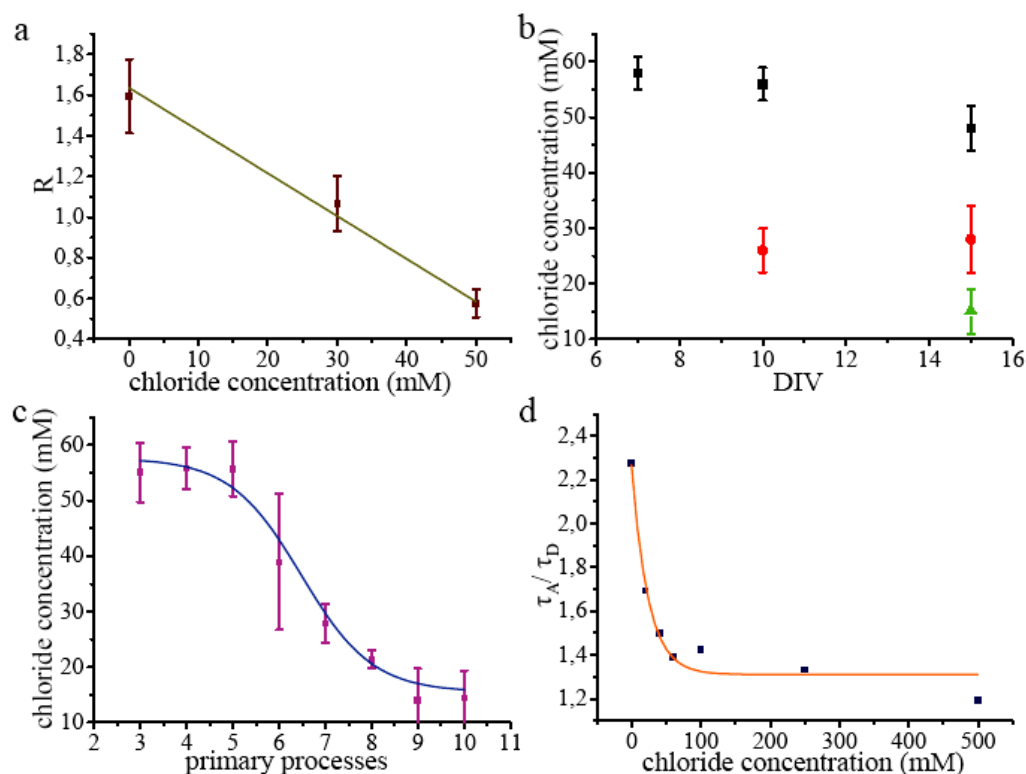
Fig. 4.1.9 *a) R values of COS-7 cells expressing Clomeleon clamped to 0mM, 30mM and 50mM chloride concentrations. R values decreased with increasing chloride concentrations from 1.59±0.18 (0mM) to 0.58±0.07 (50mM). b) Comparison of R values from COS-7 cells yielded the intracellular chloride concentrations in hippocampal neurons at different stages of maturation. A drastic decrease in chloride concentrations was found for all the classes along neuronal development. The minimum chloride concentration was observed for class III (green) at DIV 15 and the maximum for class I (black) at DIV 7. Class II showed intermediate values (red). c) A sigmoidal decrease in the intracellular chloride concentrations of neurons with increasing maturation was observed on comparing the individual R values with the number of primary processes they possess. d) The ratios of acceptor to donor mean lifetimes of Clomeleon in solution at varying chloride concentrations. A comparison of these ratios from solutions with those obtained from the different fractions of mature neurons allowed the determination of their intracellular chloride concentrations, similar to those obtained using R values of COS-7 cells.*

The dependence of the fluorescence properties of Clomeleon on maturation of neurons was further confirmed by comparing the *R* values of individual cells with the number of primary processes they possess. An overall increase in *R* values or higher FRET was observed for the cells showing higher number of processes and branching, or cells which were more developed. Comparison of the results with COS-7 cells revealed a sigmoidal decrease in the intracellular chloride concentration of individual neurons, with increasing degree of maturation (Fig. 4.1.9c). Similar number of processes (e.g. 6) gave higher and lower chloride

values at young and mature stages, respectively, thereby accounting for the high deviation observed.

The multi-exponential analysis of chloride clamped COS-7 cells could not be performed due to the presence of a short lifetime component (<10ps) arising from TBTC in gluconate buffer. Using the lifetimes obtained from purified Clomeleon on varying the chloride concentrations, the ratios of acceptor to donor mean lifetimes were calculated (Fig. 4.1.9d). Comparing these values with those from neurons at different stages of maturation, the individual chloride concentrations for the different fractions of mature neurons (DIV 15) were calculated to be 61±14mM, 18±5mM and 14±1mM for classes I-III, respectively. Since the majority of young neurons show low pH levels (Bevensee et al., 1996) which influence CFP and Topaz differentially (Llopis et al., 1998), comparable measurements could not be done in young stages.

Clomeleon was used successfully as a ratiometric and lifetime indicator, whose biophysical properties were used for studying the changes in the intracellular chloride concentrations during neuronal maturation.

4.2 IMAGING INTERACTIONS BETWEEN THE PRESYNAPTIC PROTEINS BASSOON AND CTBP1/BARS IN COS-7 CELLS BY FRET-FLIM

4.2.1 Colocalisation studies of Bassoon and its interaction partners in COS-7 cells

It has been proposed that the presynaptic protein Bassoon interacts with both CtBP1 (tom Dieck et al., 2005) and CAST (Takao-Rikitsu et al., 2004) and that these interactions contribute to the molecular organisation of the active zone of neurotransmitter release. To characterise these interactions in living cells, heterologous expression of these binding partners was used in COS-7 cells. As Bassoon forms macromolecular complexes in the cytoplasm when expressed in non-neuronal cells (Dresbach et al., 2006), we first tested whether Bassoon is functional within these complexes i.e. whether it can recruit its binding partners. Immunofluorescence studies with antibodies against CtBP1 showed a clear nuclear staining pattern (Figs. 4.2.1a-c), which changed significantly in presence of a Bassoon construct Bsn95-3938 that behaves similar to full length Bassoon when expressed in primary neuronal cultures (Dresbach et al., 2003) (Figs. 4.2.1d-f). In COS-7 cells, which endogenously do not express Bassoon, the protein showed the expected punctated pattern when expressed heterologously (Fig. 4.2.1d). In this case, the nuclear staining of CtBP1 was

significantly reduced and was seen to be enriched in Bassoon-containing macromolecular complexes in the cytosol (Fig. 4.2.1f).
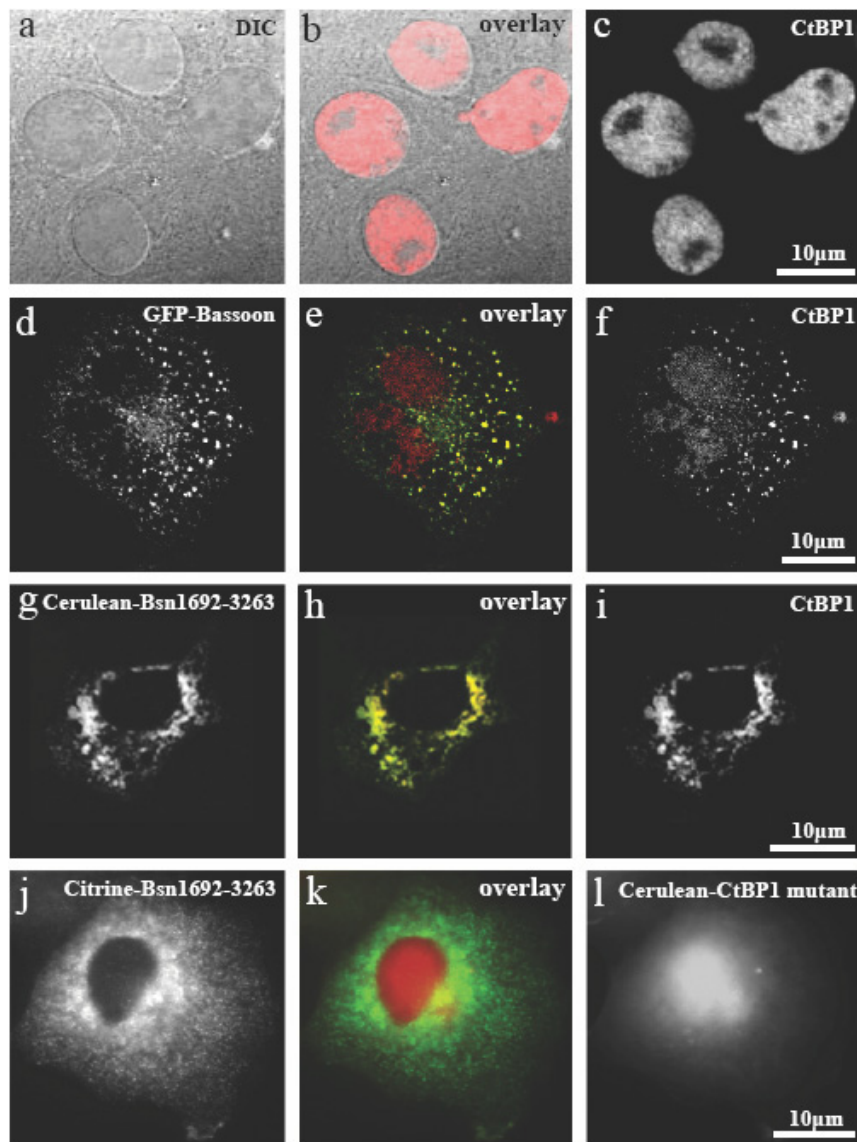
Fig. 4.2.1 *Immunofluorescence and protein overexpression studies in COS-7 cells. a-c) DIC images (a) together with immunofluorescence images of CtBP1 (c) of the same cells showed clear nuclear localisation of CtBP1. d-i) Disruption of the nuclear localisation of CtBP1 (f, i) in presence of a Bassoon construct similar to the full length (Bsn95-3938) (d) as well as in the presence of Bsn1692-3263 (g). In the overlay images (e, h), GFP-Bassoon and Cerulean-Bsn1692-3263 are shown in green, whereas CtBP1-Alexa 594 is shown in red. In both the cases, CtBP1 was enriched outside the nucleus in contrast to its original localisation pattern. No recruitment of CtBP1 mutant (l) to Bassoon containing complexes (j) was observed as shown in the overlay image (k), where Cerulean-CtBP1 mutant and Citrine-Bsn1692-3263 are shown in red and green, respectively.*

Using a fragment of Bassoon (Bsn1692-3263, Fig. 4.2.6c), which in neurons is still recruited to the presynapse, a similar change in the staining pattern of CtBP1 was observed with an increased staining in the cytosol compared to the nucleus (Figs. 4.2.1g-i). When expressing a mutant construct of CtBP1 which does not interact with Bassoon (Altrock et al., unpublished data), the nuclear localisation of the former was not influenced in presence of overexpressed Bassoon (4.2.1j-l). Thus a clear interference with the nuclear recruitment of

CtBP1 was observed in presence of Bsn95-3938 as well as Bsn1692-3263, which was not seen in the absence of an interaction between the proteins.
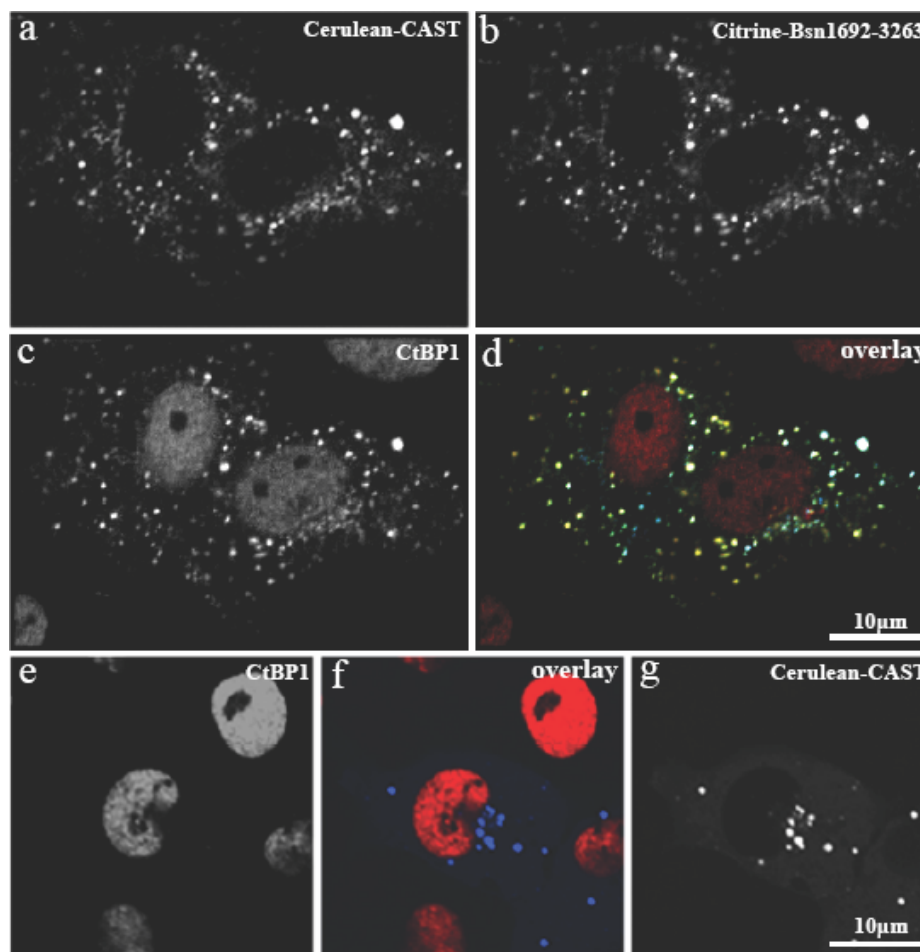
Fig. 4.2.2 *Co-recruitment of Bassoon, CtBP1 and CAST to the same intracellular complex in COS-7 cells (a-d). Cells were transfected with Cerulean-CAST (a) and Citrine-Bsn1692-3263 (b) and immunostained against CtBP1 (c). Overlay of the trimeric complex is given in (d), where Cerulean-CAST, Citrine Bsn1692-3263 and CtBP1-Alexa 594 are shown in blue, green and red, respectively. (e-g) In the absence of Bassoon, the expression of CAST (g) did not affect the nuclear localisation of endogenous CtBP1 (e). There was no extranuclear recruitment of CtBP1 to the cytosolic complexes of CAST in this case. In the overlay image (f), Cerulean-CAST and CtBP1-Alexa 594 are shown in blue and red, respectively.*

Co-expression of Bassoon (Bsn95-3938 or Bsn1692-3263) with CAST in COS-7 cells revealed a simultaneous co-recruitment of CtBP1 and CAST to the same Bassoon-containing molecular complexes (Figs. 4.2.2a-d). Thus the presence of both interaction partners of Bassoon in the same complex was observed not to hinder each other even in the case of the short fragment of Bassoon. No such extranuclear recruitment of endogenous CtBP1 was observed in the presence of CAST alone (Figs. 4.2.2e-g).

4.2.2 Photophysics of Cerulean and Citrine in COS-7 cells

Since the photophysical properties of the common fluorescent probes CFP and YFP were observed to be perturbed by cellular environments (Jose et al., 2007b), it was crucial to

check the same for their photostable variants, namely Cerulean and Citrine, used for the current FRET-FLIM studies. COS-7 cells expressing Cerulean alone showed emission maxima at 486 nm (Fig. 4.2.3a).
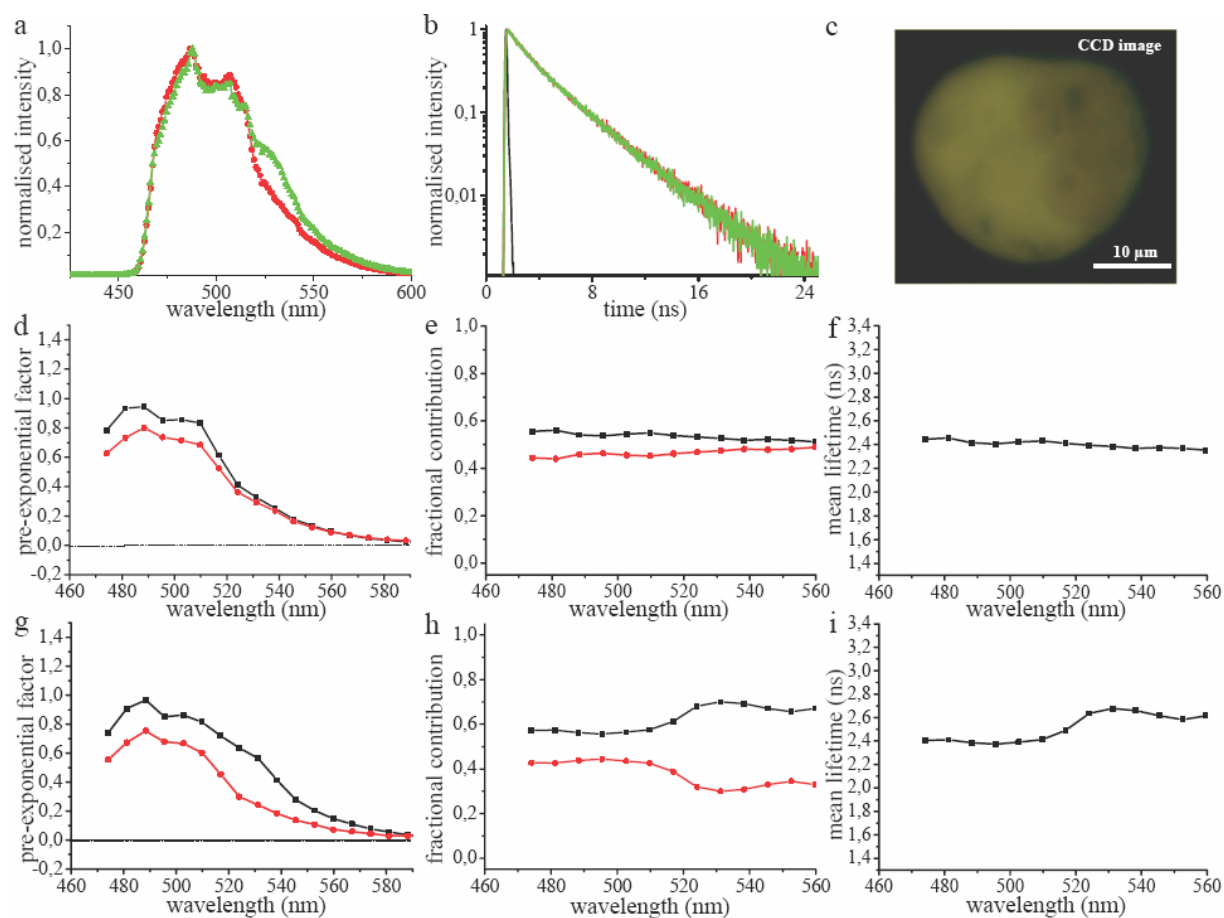
Fig. 4.2.3 *Fluorescence emission of Cerulean at 420 nm excitation in living COS-7 cells. a) Comparison of fluorescence emission spectra of Cerulean alone (red) with co-expression of Cerulean and Citrine (green). The fluorescence emission maximum for Cerulean was observed at 486 nm. A small Citrine component due to its high extinction coefficient was observed for the latter. b) Fluorescence decay of Cerulean (red) was unperturbed in presence of Citrine (green) outside the FRET radius. IRF is shown in black. c) COS-7 cells expressing a mixture of Cerulean and Citrine, which showed a homogenous distribution as expected. d, g) DAS of Cerulean alone (d) and in the presence of Citrine (g). Intensity decays were analysed in 17 emission bands from 470 nm to 590 nm and the pre-exponential factors of lifetimes, τ_1 (black) and τ_2 (red) (Table 4.2.1) were plotted along the wavelength. In both the cases, the pre-exponential factors showed only positive values. e, h) The normalised fractional contributions of the lifetimes, τ_1 (black) and τ_2 (red) were calculated from the pre-exponential factors and plotted along the wavelength for Cerulean alone (e) and in presence of Citrine (h). f, i) Mean lifetimes of each emission band were plotted along the wavelength for Cerulean alone (f) and in presence of Citrine (i). Error bars are not shown due to their very small variability (<2% for fractional contributions and <0.05 ns for mean lifetimes).*

In contrast to the monoexponential fluorescence decay previously reported in solutions (Rizzo et al., 2004), a biexponential character was observed for Cerulean in living COS-7 cells with lifetimes of 3.37±0.03 ns (τ_1) and 1.32±0.05 ns (τ_2) (Table 4.2.1). DAS revealed similar distributions for the lifetimes, confirming the source of both the lifetimes to be the Cerulean chromophore itself (Fig. 4.2.3d). The contributions of τ_1 and τ_2 were almost similar (Table 4.2.1) and a significant improvement in chisquare ($\Delta\chi^2$=2±0.1) was observed on increasing the number of exponentials from one to two. The differences in the quality of fits

were evident from the distributions of the corresponding residues and autocorrelation functions (Figs. 4.2.4a, b). The fractional contributions of the lifetimes as well as the mean lifetimes did not show any deviation along the wavelength axis (Figs. 4.2.3e, f). The mean lifetime at the donor emission maxima was measured to be 2.46±0.04 ns. The small deviations in the lifetimes from CFP could arise due to the mutations included in the construct as well.
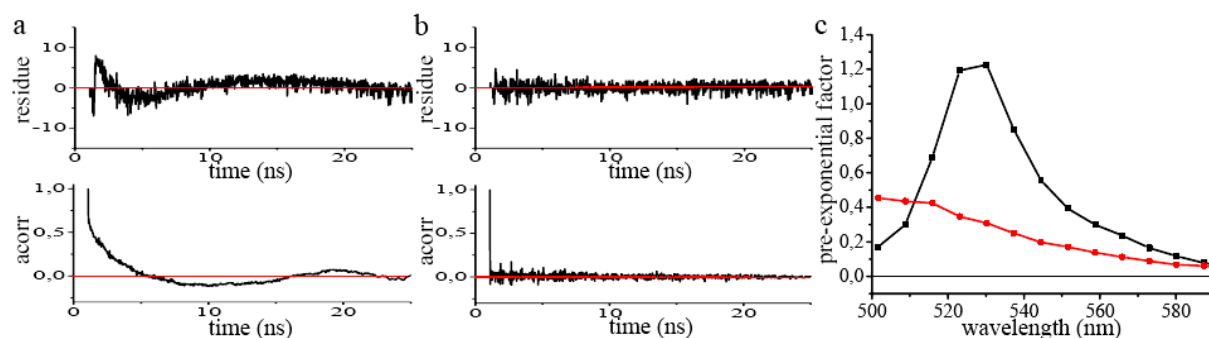
Fig. 4.2.4 *a) The fluorescence decay of Cerulean was fit by a single exponential model with lifetime of 2.77±0.02 ns. The corresponding residues (top) and autocorrelation fits (bottom) are shown. The deviations show the bad quality of the fit. b) A significant improvement in the quality of fit was observed on giving a biexponential model for Cerulean (Table 4.2.1). The corresponding residues (top) and autocorrelation fits (bottom) are shown. $\Delta\chi^2=2\pm0.1$ between the models. c) DAS of Citrine expressing cells at 420 nm excitation. Intensity decays were analysed in 13 emission bands from 500 nm to 590 nm and the pre-exponential factors of lifetimes, 3.20±0.03 ns (black) and 0.22±0.14 ns (red) were plotted along the wavelength. Deviations in the short lifetime component were expected due to the cellular variability of autofluorescence. No negative DAS was observed at the acceptor emission maxima due to the absence of energy transfer.*

Co-expression of Cerulean and Citrine in the same cell did not change the fluorescence emission spectra (Fig. 4.2.3a) or decay (Fig. 4.2.3b) compared to single expression of Cerulean, except for a small red-shifted emission near the Citrine maxima. The fluorescence lifetimes as well as their contributions (Fig. 4.2.3g) were also observed to be similar to Cerulean alone (Table 4.2.1). This in turn ensured the suitability of the excitation wavelength used (420 nm), which was optimal for >80% Cerulean excitation, whereas direct excitation of Citrine was very low (<5%). The Citrine emission observed with this low excitation would be accounted by the high molar extinction coefficient of the probe (Griesbeck et al., 2001). This in turn resulted in slight deviations in the fractional contributions (Fig. 4.2.3h) as well as in the distribution of mean lifetimes along the wavelength axis (Fig. 4.2.3i), compared to Cerulean alone. In this case, the donor mean lifetimes remained unchanged at 2.41±0.04 ns, whereas acceptor mean lifetimes showed slight increase up to 2.66±0.08 ns. Direct excitation of Citrine alone at 420 nm resulted in a single lifetime of 3.20±0.03 ns combined with a short lifetime contribution of 0.22±0.14 ns. The latter did not arise from the Citrine chromophore, but mostly from cell autofluorescence, as clearly observed from the DAS (Fig. 4.2.4c) which showed a completely different distribution compared to the 3.20 ns component.

4.2.3 FLIM studies on CtBP1 and CAST in COS-7 cells

COS-7 cells expressing CtBP1 and CAST were measured to check for interactions between the proteins in the absence of Bassoon. Cerulean-CtBP1 showed fluorescence dynamics very similar to Cerulean with lifetimes of 3.44±0.04 ns and 1.39±0.08 ns (Table 4.2.1, Figs. 4.2.5a, b). The contributions of the individual lifetimes also showed no deviations from Cerulean alone resulting in a mean lifetime of 2.57±0.07 ns at the donor emission maxima (Fig. 4.2.5f).
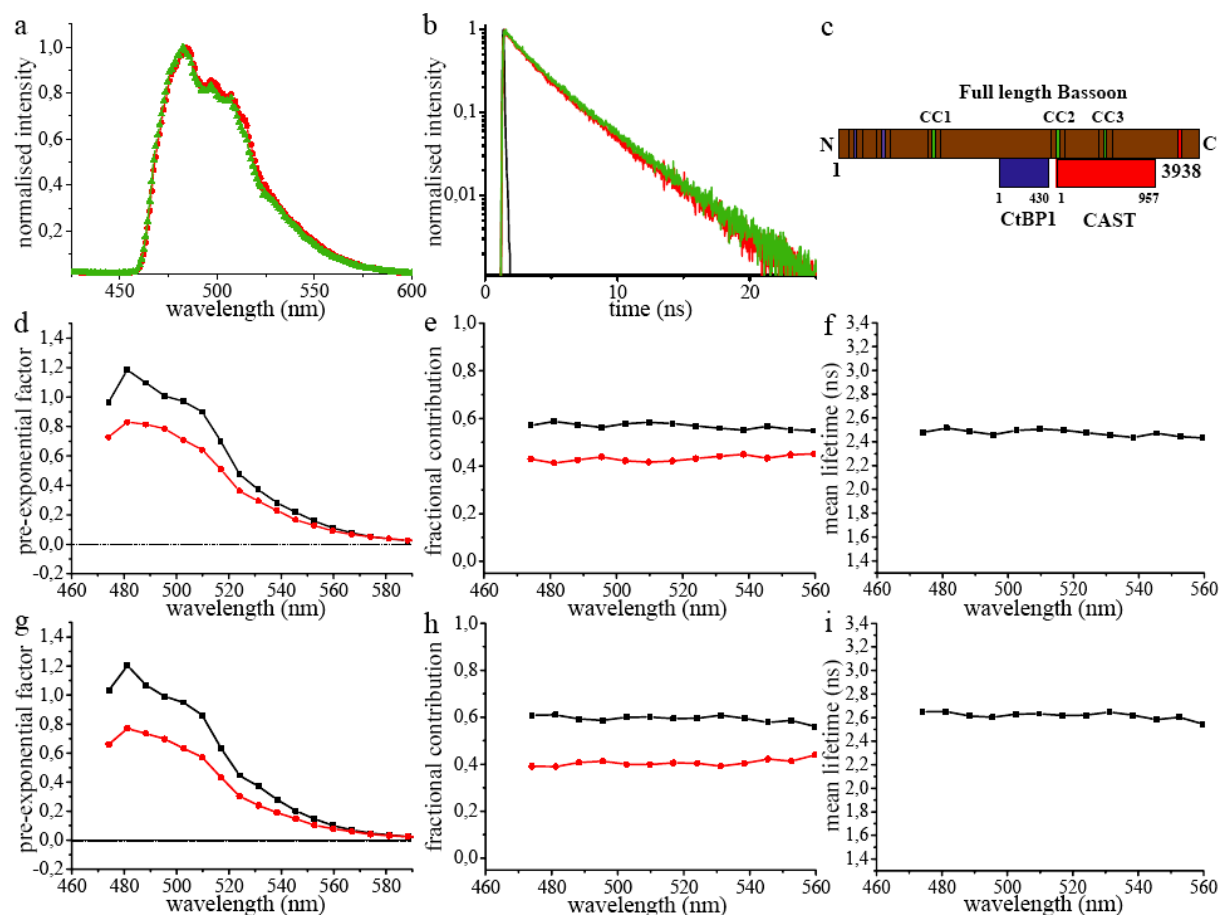
Fig. 4.2.5 *The fluorescence dynamics of Cerulean-CtBP1 in the absence and presence of Citrine-CAST in living COS-7 cells. a) Comparison of fluorescence emission spectra of Cerulean-CtBP1 alone (red) with the co-expression of Cerulean-CtBP1 and Citrine-CAST (green). The fluorescence emission maximum for Cerulean-CtBP1 was observed at 486 nm. No Citrine emission was observed in the absence of FRET. b) Fluorescence decay of Cerulean-CtBP1 (red) was unperturbed in presence of Citrine-CAST (green). IRF is shown in black. c) Scheme illustrating the proposed binding regions for CtBP1 and CAST on the full length Bassoon (Takao-Rikitsu et al., 2004; tom Dieck et al., 2005). Bassoon was essential for the formation of a trimeric complex of these proteins, without which there was no association between CtBP1 and CAST. d) DAS of Cerulean-CtBP1 alone and in presence of Citrine-CAST (g). The pre-exponential factors of lifetimes, τ₁ (black) and τ₂ (red) (Table 4.2.1) were plotted along the wavelength. In both the cases, the pre-exponential factors showed only positive values. e, h) The normalised fractional contributions of the lifetimes, τ₁ (black) and τ₂ (red) were plotted along the wavelength for Cerulean-CtBP1 alone (e) and in presence of Citrine-CAST (h). f, i) Mean lifetimes of each emission band were plotted along the wavelength for Cerulean-CtBP1 alone (f) and in presence of Citrine-CAST (i). No deviations along the spectra were observed in both the cases. Error bars are not visible due to their very small variability (<2% for fractional contributions and <0.08 ns for mean lifetimes).*

FLIM measurements in COS-7 cells co-expressing Cerulean-CtBP1 with Citrine-CAST revealed the fluorescence emission spectra as well as decay of the co-expressed cells to

be very similar to those of the donor alone (Figs. 4.2.5a, b). In this case also, no significant changes in lifetimes, their individual contributions or in the overall donor mean lifetimes were observed, confirming the absence of FRET between the two constructs (Table 4.2.1). In both cases, DAS revealed only positive amplitudes for all the lifetimes (Figs. 4.2.5d, g). Furthermore, the fractional contributions (Figs. 4.2.5e, h) and mean lifetimes (Figs. 4.2.5f, i) showed no significant deviations along the spectra. The results were corroborative with the observation of absence of changes in the endogenous localisation pattern of CtBP1 in presence of CAST (Figs. 4.2.2e-g).

Table 4.2.1 Comparison of decay kinetics of Cerulean in COS-7 cells with its fusion constructs

construct	n	τ_1 %	τ_1 (ns)	τ_2 %	τ_2 (ns)	τ_3 %	τ_3 (ns)	τ_{mean} (ns)
Cerulean	5	56±1	3.37±0.03	45±1	1.32±0.05	-	-	2.46±0.04
Cerulean + Citrine	5	57	3.32±0.02	43	1.23±0.06	-	-	2.41±0.04
Cerulean-CtBP1	7	58±1	3.44±0.04	42±1	1.39±0.08	-	-	2.57±0.07
Cerulean-CtBP1 + Citrine-CAST	8	60±1	3.41±0.05	41±1	1.29±0.07	-	-	2.55±0.07
Cerulean-Bsn1692-3263	5	44±5	3.35±0.12	38±2	1.56±0.12	19±5	0.23±0.07	2.09±0.17
Cerulean-Bsn1692-3263 + Citrine-CtBP1	5	24±2	3.39±0.06	45±2	1.42±0.11	31±2	0.20±0.10	1.51±0.10

The fluorescence lifetimes of Cerulean were not perturbed in presence of co-expressed Citrine in the same cell. But significant changes in its properties were observed depending on the protein to which it was fused as well as in presence of FRET. The lifetimes are denoted as τ_1, τ_2 and τ_3 and their corresponding contributions as τ_1%, τ_2% and τ_3%, respectively. Errors <1% for the contributions are not shown. The number of independent measurements is denoted as n. All data were recorded using the point detector.

4.2.4 Interaction studies of Bassoon and CtBP1 by FRET-FLIM

The colocalisation studies of Bassoon and CtBP1 were extended to live cell interaction studies by FRET and FLIM. Though the possibility for such an interaction has already been

indicated by biochemical techniques, a confirmation of this under real cell conditions was crucial to appreciate the physiological relevance of this interaction. Since full length Bassoon was too large for FRET studies, a shorter fragment of it namely Bsn1692-3263 encoding amino acid residues 1692-3263 was used for the purpose (Fig. 4.2.6c). This construct was shown to be functional similar to the full length construct, with presynaptic recruitment, when expressed in primary neuronal cultures. Cerulean and Citrine were used as donor-acceptor pairs fused to Bsn1692-3263 and CtBP1, respectively.
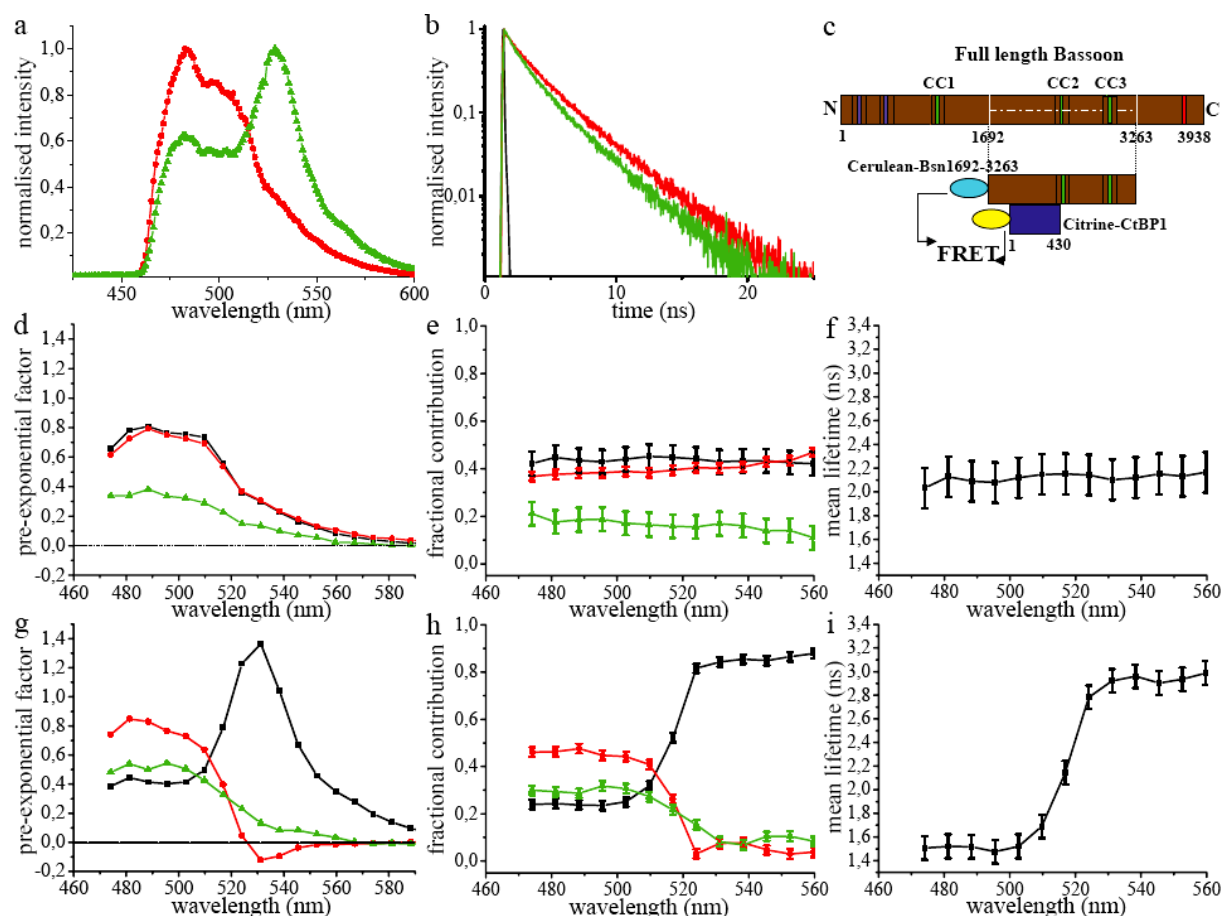
Fig. 4.2.6 Fluorescence dynamics of Cerulean-Bsn1692-3263 in the absence and presence of Citrine-CtBP1 in living COS-7 cells. a) Comparison of fluorescence emission spectra of Cerulean-Bsn1692-3263 (red) with the FRET sample (green). A significant Citrine enhancement was observed in presence of FRET. b) Fluorescence decay of Cerulean-Bsn1692-3263 in the FRET sample (green) was shorter compared to the control (red). IRF is shown in black. c) Bsn1692-3263 construct compared to the full length Bassoon. A scheme for the observed FRET between Bsn1692-3263 and CtBP1 is proposed. d) DAS of control Cerulean-Bsn1692-3263. The pre-exponential factors of lifetimes, τ_1 (black), τ_2 (red) and τ_3 (green) were plotted along the wavelength (Table 4.2.1). e) The normalised fractional contributions of lifetimes, τ_1 (black), τ_2 (red) and τ_3 (green) were plotted with error bars along the wavelength for Cerulean-Bsn1692-3263. f) Mean lifetimes of each emission band were plotted along the wavelength for Cerulean-Bsn1692-3263. The variability between the cells is represented by error bars, which shows deviation due to the aggregating nature of the construct. g) DAS of the FRET sample, Cerulean-Bsn1692-3263+Citrine-CtBP1. The pre-exponential factors of lifetimes, τ_1 (black), τ_2 (red) and τ_3 (green) (Table 4.2.1) were plotted along the wavelength. Negative amplitudes were observed for τ_2 at the acceptor emission maximum in presence of FRET. h) The normalised fractional contributions of lifetimes, τ_1 (black), τ_2 (red) and τ_3 (green) were plotted with error bars along the wavelength for the FRET sample, which showed an increase in τ_1 with a simultaneous decrease for τ_2 and τ_3 along the spectra. i) Mean lifetimes of each emission band were plotted with error bars along the wavelength for the FRET sample.

Bsn1692-3263, when expressed in COS-7 cells, was observed to show higher aggregating properties compared to full length Bassoon. As a result, though the fluorescence emission spectrum (Fig. 4.2.6a) was unaffected, the fluorescence decay of Cerulean-Bsn1692-3263 was deviated resulting in a third short lifetime component of 0.23 ± 0.07 ns (τ_3) (Table 4.2.1, Fig. 4.2.6b). A cellular variability of this component was observed due to the aggregating nature of the protein. Although slight contributions of autofluorescence from cells could not be avoided, the major contribution of this third lifetime was observed to be the chromophore of the fusion construct itself, as clear from the DAS (Fig. 4.2.6d). The contribution of the third component was less than 20% compared to the contributions of the other lifetimes. Cerulean-Bsn1692-3263 did not show any deviations in the fractional contributions of its lifetimes or distribution pattern of the mean lifetimes (Figs. 4.2.6e, f), similar to Cerulean alone. Due to the contribution of the short lifetime component, the mean lifetime of Cerulean-Bsn1692-3263 was reduced from 2.46 ± 0.04 ns to 2.09 ± 0.17 ns at the donor emission maxima (Table 4.2.1). But the DAS showed only positive values for the pre-exponential factors of all the lifetimes (Fig. 4.2.6d).

Co-expression of Cerulean-Bsn1692-3263 and Citrine-CtBP1 resulted in significant differences in the fluorescence emission spectra as well as decay of both the probes (Figs. 4.2.6a, b). A clear Citrine enhancement at 529 nm was observed, which could arise only due to energy transfer from Cerulean to Citrine. The lifetimes of Cerulean-Bsn1692-3263 were similar in presence of FRET with the exception in the changes in the contributions of the individual lifetimes (Table 4.2.1). The contribution of τ_1 was significantly reduced from 44% to 24%, whereas τ_2 and τ_3 increased from 38% and 19% to 45% and 31%, respectively. The DAS showed clear negative values for τ_2 at the acceptor emission maxima, whereas τ_3 showed only a reduction at the same (Fig. 4.2.6g). The fractional contributions revealed an increase in τ_1 along the wavelength axis with a simultaneous decrease for the two short lifetimes (Fig. 4.2.6h). The mean lifetime distribution showed a distinct change from previous measurements with a clear decrease at the donor emission maxima from 2.09 ± 0.17 ns to 1.51 ± 0.10 ns (Table 4.2.1), which increased along the spectra to 2.87 ± 0.15 ns at the acceptor maxima (Fig. 4.2.6i).

Since Cerulean-Bsn1692-3263 showed a distinct punctated pattern with a clear recruitment of Citrine-CtBP1 to these fine puncta, a detailed study at smaller regions consisting of these complexes was necessary for a better understanding of this interaction. To this end, COS-7 cells expressing Cerulean-Bsn1692-3263 and Citrine-CtBP1 were imaged using the QA detector. Small ROIs were defined as shown in Fig. 4.2.7a and the corresponding fluorescence decays analysed for the donor and the acceptor probes

simultaneously (Table 4.2.2, Fig. 4.2.7b). Clear reductions in the donor mean lifetimes with simultaneous increase in the mean lifetimes of the acceptor were observed, as shown previously with the point detector. The changes in the contributions of the lifetimes from the control were also similar (Table 4.2.2). The acceptor fluorescence decay showed a clear change with negative contributions (<10%) for the 1.4 ns (τ_2) component. Small deviations in fluorescence lifetimes from the two detectors could be well expected due to the differential illumination methods used and the differential influence from cell autofluorescence. The donor and the acceptor decays were fit with similar lifetimes and the quality of the fit was observed to be good from the residues of the individual fits (Fig. 4.2.7c).
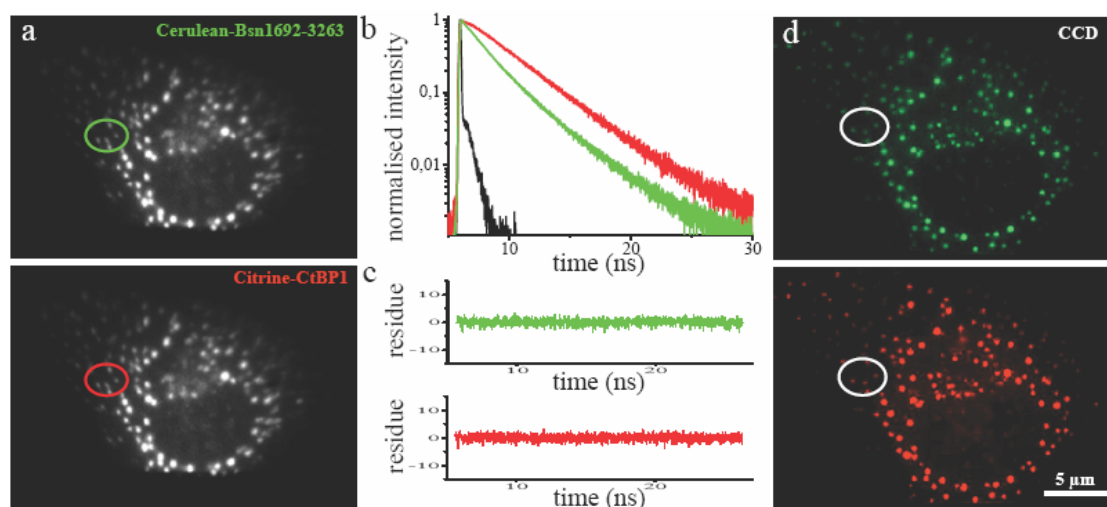
Fig. 4.2.7 *COS-7 cells co-expressing Cerulean-Bsn1692-3263 and Citrine-CtBP1 as measured by the imaging detector. a) The fluorescence emission was split up into Cerulean-Bsn1692-3263 and Citrine-CtBP1 emission bands as shown. Selected ROIs are indicated by coloured circles. b) In presence of energy transfer, Cerulean-Bsn1692-3263 (green) showed a short fluorescence decay (Table 4.2.2) with a simultaneous rise for Citrine-CtBP1 (red). IRF is shown in black. c) The quality of the individual fits (donor-green, acceptor-red) is shown by the distribution of the residues. In the corresponding fluorescence images from the CCD camera (d), the green and red spots denote the donor and acceptor channels, respectively.*

Table 4.2.2 Fluorescence dynamics of Cerulean in COS-7 cells in the absence and presence of FRET

construct	τ_1 %	τ_1 (ns)	τ_2 %	τ_2 (ns)	τ_3 %	τ_3 (ns)	τ_{mean} (ns)
Cerulean-Bsn1692- 3263	40±3	3.14±0.09	41±2	1.57±0.07	19±3	0.39±0.12	1.98±0.11
Cerulean-Bsn1692-3263 + Citrine-CtBP1	21±3	3.3±0.23	48±4	1.44±0.20	31±5	0.38±0.12	1.49±0.18

The fluorescence lifetimes of Cerulean-Bsn1692-3263 as well as their fractional contributions were significantly changed in presence of FRET, which resulted in drastic decrease of mean lifetimes at the donor emission peak. The lifetimes are denoted as τ_1, τ_2 and τ_3 and their corresponding contributions as τ_1%, τ_2% and τ_3%, respectively. The values shown are from five independent measurements, with at least 6 ROIs selected from each cell. The data were recorded using the imaging detector.

Using τ_1 of Cerulean-Bsn1692-3263 alone as the unperturbed donor lifetime (τ_D) and τ_2 of cells co-expressing Cerulean-Bsn1692-3263 and Citrine-CtBP1 (Table 4.2.2) as the FRET lifetime (τ_{DA}), the FRET efficiency was calculated to be 54%. τ_2 was chosen as the FRET lifetime since it was observed to be most affected in presence of energy transfer, yielding negative values for its pre-exponential factors. τ_1 of the donor probe (Table 4.2.2) took into account the deviations in the kinetics due to the aggregating nature of the protein. Assuming a random orientation for the dipole moments with $\kappa^2=2/3$, and using $R_0=4.9$ nm for CFP/YFP pairs; this yielded an inter-molecular distance r of 4.8 nm between the Cerulean and Citrine chromophores of the interacting proteins.

4.2.5 FLIM studies on Bassoon and CAST in COS-7 cells

Cerulean-Bsn1692-3263 and Citrine-CAST expressing COS-7 cells were imaged to study interactions between the proteins in similar complexes. The co-expressed cells revealed fluorescence dynamics similar to the donor probe alone, except for a slight Citrine enhancement in the emission spectra (Fig. 4.2.8a).
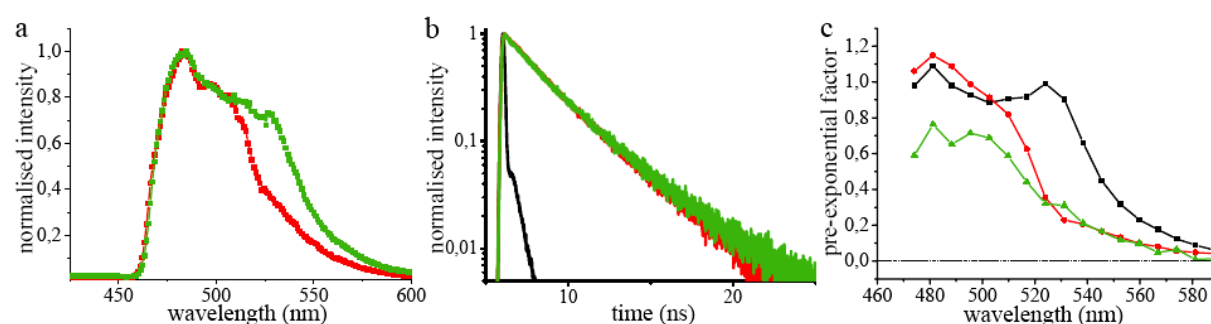
Fig. 4.2.8 Fluorescence emission of Cerulean-Bsn1692-3263 in the absence and presence of Citrine-CAST in living COS-7 cells. a) Comparison of fluorescence emission spectra of Cerulean-Bsn1692-3263 (red) with the co-expressed sample (green). A slight Citrine enhancement was observed in presence of Citrine-CAST. b) Fluorescence decay of Cerulean-Bsn1692-3263 in the co-expressed sample (green) was similar to the control (red). IRF is shown in black. c) DAS of the co-expressed sample. The pre-exponential factors of lifetimes, τ_1 (black), τ_2 (red) and τ_3 (green) were plotted along the wavelength.

The donor fluorescence decay for the pair was comparable to that of Cerulean-Bsn1692-3263 (Fig. 4.2.8b). The decay was fit by a three exponential model with lifetimes of 3.42±0.18 ns (τ_1), 1.59±0.11 ns (τ_2) and 0.40±0.08 ns (τ_3) contributing to 36±4%, 41±3% and 23±3%, respectively, at the donor emission maxima. This yielded a mean lifetime of 1.98±0.06 ns at the same, which slightly increased up to 2.14±0.14 ns at the acceptor emission maxima. DAS displayed only positive pre-exponential factors for all the lifetimes (Fig. 4.2.8c). Though Bassoon and CAST were recruited to similar complexes in COS-7 cells, direct interaction between the proteins could not be confirmed by FRET, which could be due to the the large distance between the interacting domains bringing the fluorophores outside the FRET radius.

Thus a direct physical association of Bassoon and CtBP1 was confirmed in living cells using a combination of FRET and FLIM. Bassoon was observed to be essential for forming a macromolecular complex with CtBP1 and CAST as proven from the FLIM studies, where no interaction was observed between the latter in the absence of Bassoon. Deviations in the fluorescence properties of Cerulean were observed depending on the protein to which it was fused. Nevertheless, interaction studies were confirmed by simultaneous analysis of donor and acceptor decays, whereby clear reduction and simultaneous increase in the donor and acceptor mean lifetimes, respectively, as well as negative amplitudes for the lifetimes of the acceptor involved in FRET were observed.

4.3 IMAGING INTRACELLULAR TRAFFICKING OF THE PRESYNAPTIC PROTEINS BASSOON AND CTBP1/BARS IN NEURONS BY FRET-FLIM

4.3.1 Localisation studies of Bassoon, CtBP1 and CAST in neurons

Neurons are highly specialised cells whose dynamic nature make them difficult for deep investigation, but at the same time make them all the more interesting. In order to study the role of Bassoon in recruiting the presynaptic proteins including CtBP1 and CAST, it was essential to study these interactions in living hippocampal neurons to address the formation of such complexes.
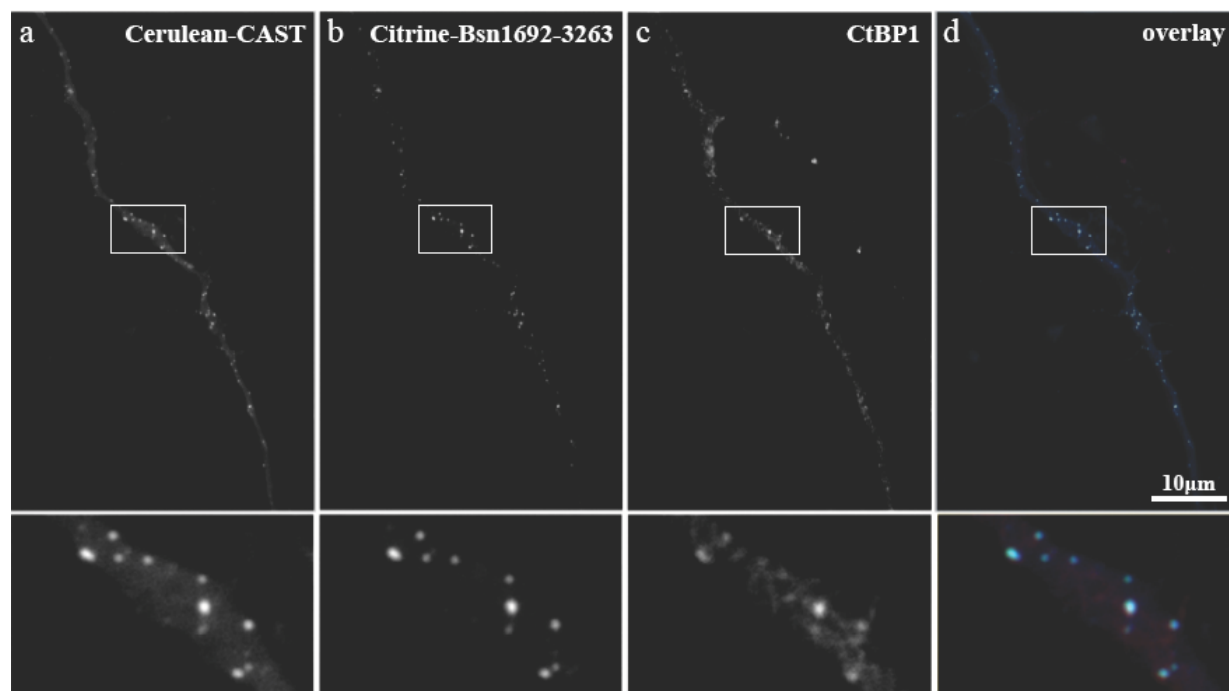
Fig. 4.3.1 *Colocalised spots of Bsn1692-3263, CTBP1 and CAST in neuronal axons of DIV 7. Cerulean-CAST and Citrine-Bsn1692-3263 were co-expressed along with endogenous staining of CtBP1.*

Young neurons at DIV 7 expressing Cerulean-CAST and Citrine-Bsn1692-3263 were immunostained with antibodies against CtBP1, which revealed the co-recruitement of these proteins to similar complexes in neuronal axons (Fig. 4.3.1). Immunostainings revealed the distribution pattern of Bassoon and CtBP1 at different stages of neuronal development. In cultured hippocampal neurons at early stages of neuronal differentiation (~DIV 2), Bassoon along with CtBP1 were detected at the cell soma and in all minor neurites (Fig. 4.3.2).
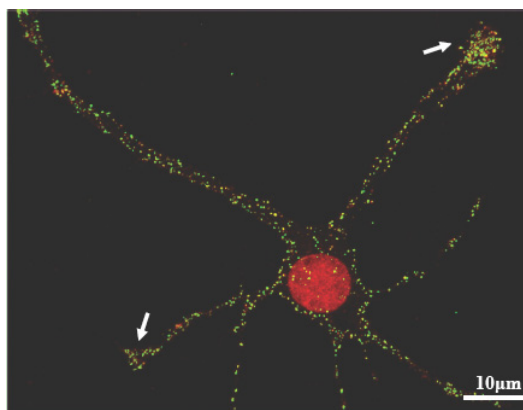
Fig. 4.3.2 Colocalisation of Bassoon and CtBP1 in neurites of DIV 2. Endogenous stainings of Bassoon and CtBP1 are shown in green and red, respectively. At early stages of neuronal differentiation, the proteins otherwise purely axon-associated were present in all processes.

By DIV3, the distributions of the proteins were polarised. In this case, Bassoon exhibited primarily a fine punctate pattern in the distal part of axon and its dynamic actin-supported extensions; the growth cones, which is eventually modified to form the presynaptic terminal at a later point of differentiation (Fig. 4.3.4, (Sanes and Lichtman, 1999; Ziv and Garner, 2004). The observations were in agreement with the previous reports on recruitment of Bassoon to the presynaptic bouton at the initial phase of synaptogenesis (Zhai et al., 2000), indicating the scaffolding nature of the protein.
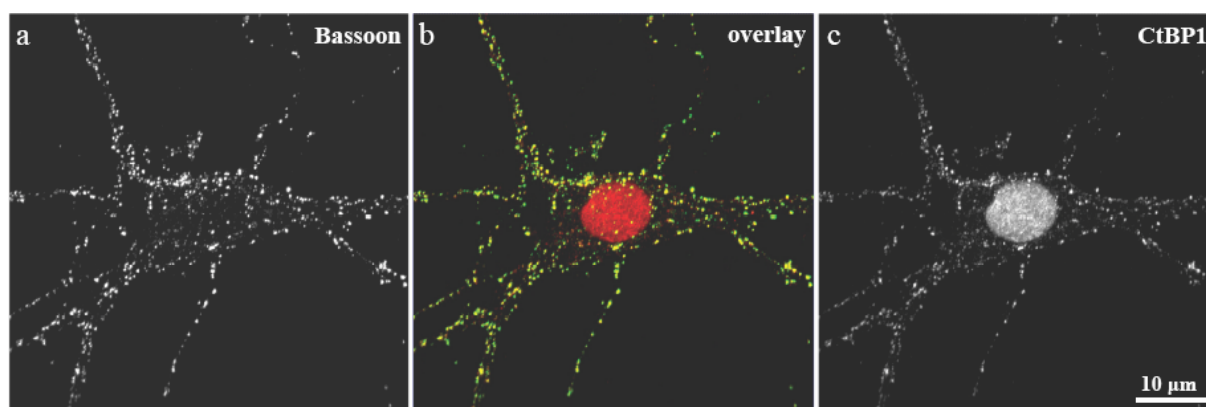
Fig. 4.3.3 Endogenous staining of Bassoon (green) and CtBP1 (red) in mature neurons at DIV 16. A colocalised punctuate distribution of the proteins were observed along the processes, indicating possible synapses.

CtBP1 was also observed at Bassoon containing complexes in young axons and its terminals, in addition to its nuclear localisation pattern (Fig. 4.3.4). The proteins were also

observed to be colocalised in the neuronal axons and synapses of mature neurons (DIV 16) (Fig. 4.3.3, (tom Dieck et al., 2005)). The studies indicated the potential capability of the short fragment of Bassoon to form trimeric complexes with its interaction partners in neurons, as observed in COS-7 cells, confirming the functionality of the construct. These preassembled complexes could be transported along axons to presynaptic active zones. This in turn signified the scaffolding potential of a short fragment of Bassoon in synaptogenesis.

4.3.2 Translocation studies of Bassoon and CtBP1 in living neurons

In order to study whether Bassoon and CTBP1 are recruited in similar PTVs to synapses, young neurons at DIV 4 expressing Cerulean-CtBP1 and Citrine-Bsn1692-3263 were imaged continuously for 30 minutes (Fig. 4.3.4a, Movie 4.3.1). This revealed retrograde (Fig. 4.3.4b, Movie 4.3.2) as well as anterograde (Fig. 4.3.4c, Movie 4.3.3) co-transport of the proteins along axons.
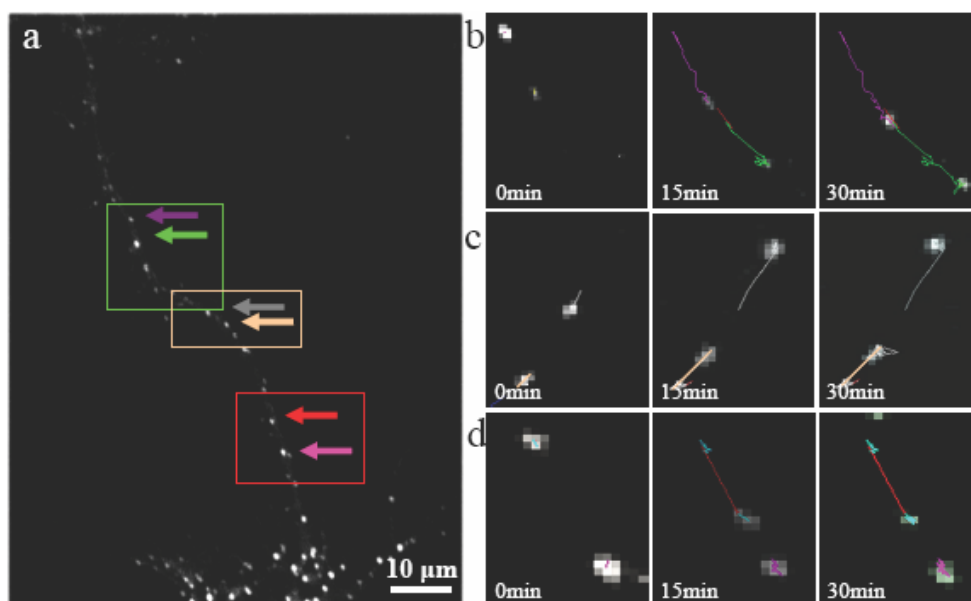
Fig. 4.3.4 a) *A young neuron at DIV 4 expressing Cerulean-CtBP1 and Citrine-Bsn1692-3263 was imaged continuously for 30 minutes (Movie 4.3.1). Individual frames were captured at an interval of 1 minute. The captured frames at 0, 15 and 30 min are shown for different types of movement (b-d). The co-expression was observed along the axon as well as at growth cones. Co-transport of the proteins in both directions was observed along the same processes. The fine puncta were observed to merge into larger complexes as well as to exit from them. Similar complexes also showed bidirectional transport. The entire measurements were done at 37°C. b-d) Time-lapse studies revealed retrograde (b, Movie 4.3.2), anterograde (c, Movie 4.3.3) or random (d, Movie 4.3.4) movements for the puncta corresponding to the focussed regions shown by green, peach and red rectangles in (a), respectively. The arrows point to the focussed spots, the colours corresponding to their trajectories being shown in b-d. The region selected in the red rectangle is rotated 90° clockwise and is shown in (d). The stationary punctum focussed in (d) showed a random movement around a fixed point, the trajectory being shown in pink. A second punctum displaying retrograde transport (red trajectory) is focussed in the same image to confirm the motion of the former punctum to be its own, rather than the motion of the cell culture as a whole. Retrograde transport (b, violet, green trajectories) was slower compared to the anterograde (c, grey, peach trajectories). For the latter, fast movements of puncta followed by their stationary nature was observed. Only the bright complexes which show slow movement were tracked by the software.*

Most of the puncta observed were mobile, a very few of them being quite stationary and showing slow 'to and fro' movement (Fig.4.3.4d, Movie 4.3.4), the latter being larger and brighter complexes. The mobile puncta were classified into two types. 1) Highly mobile puncta below the resolution limit which were dim and difficult to track due to their high speed, indicating potential PTVs. 2) Brighter and more stable puncta, which showed a moderate movement. These were usually formed by merging of few PTVs and remained stable for a certain period of time. PTVs were also observed to exit from these complexes. Smallest puncta, indicating PTVs showed very fast movements between these complexes. In contrast to the highly mobile PTVs, the larger complexes were stable and seemed to scan the area before moving to the next point. The same complexes also exhibited bidirectional transport over time along the same processes. The bright stationary puncta which could possibly indicate synapses were very few in number due to the young age of neurons. The trajectories of moderately moving larger puncta were traced using a particle tracking software (Section 3.2.4.2) as shown in Figs. 4.3.4b-d (Movies 4.3.2-4.3.4), corresponding to the regions focussed in Fig. 4.3.4a. Anterograde transport (Movie 4.3.3) was faster compared to retrograde (Movie 4.3.2) and was difficult to track. Over a short distance, a fast movement followed by a stationary nature was observed for most of these larger puncta. The relatively stationary puncta showed movement around a fixed point (Movie 4.3.4). Similar studies were also done with Cerulean-CAST and Citrine-Bsn1692-3263, which indicated similar co-transport of proteins. In this case, larger complexes were also seen due to the oligomerising tendency of the proteins, which moved slower in contrast to the smaller spots. The studies indicated the possibility for transport of the presynaptic proteins CtBP1 and CAST as a single complex with Bassoon as the linker, to the presynapses.

4.3.3 Fluorescence emission dynamics of Cerulean-Bsn1692-3263 in neurons

For FRET-FLIM studies, it was important to understand the properties of the donor molecule alone in similar conditions as the sample. To overrule any deviations in the photophysical properties of Cerulean due to ionic variations in neurons along development, neurons expressing the donor fusion construct Cerulean-Bsn1692-3263 were imaged at young (DIV 9) as well as at mature (DIV 16) stages. This short construct of Bassoon, recruited to the presynapse, was used instead of full length Bassoon since the latter was too large for FRET studies. Irrespective of the maturation stage of neurons, Cerulean-Bsn1692-3263 showed the emission maximum at 486 nm (Fig. 4.3.5a). A biexponential fluorescence decay was observed with lifetimes of 3.14 ± 0.14 ns (τ_1) and 1.29 ± 0.16 ns (τ_2) with contributions, $59\pm3\%$ and

41±3% at its emission maxima, respectively (Table 4.3.1, Fig. 4.3.5b). This resulted in a mean lifetime of 2.32±0.15 ns at the same (Fig. 4.3.5d). The mean lifetimes of Cerulean-Bsn1692-3263 remained constant over the spectra. DAS displayed only positive values for the pre-exponential factors of all the lifetimes (Fig. 4.3.5c). The plots of fractional contributions of the individual lifetimes exhibited slight decrease in τ_1 with a simultaneous increase in τ_2, along the spectra.
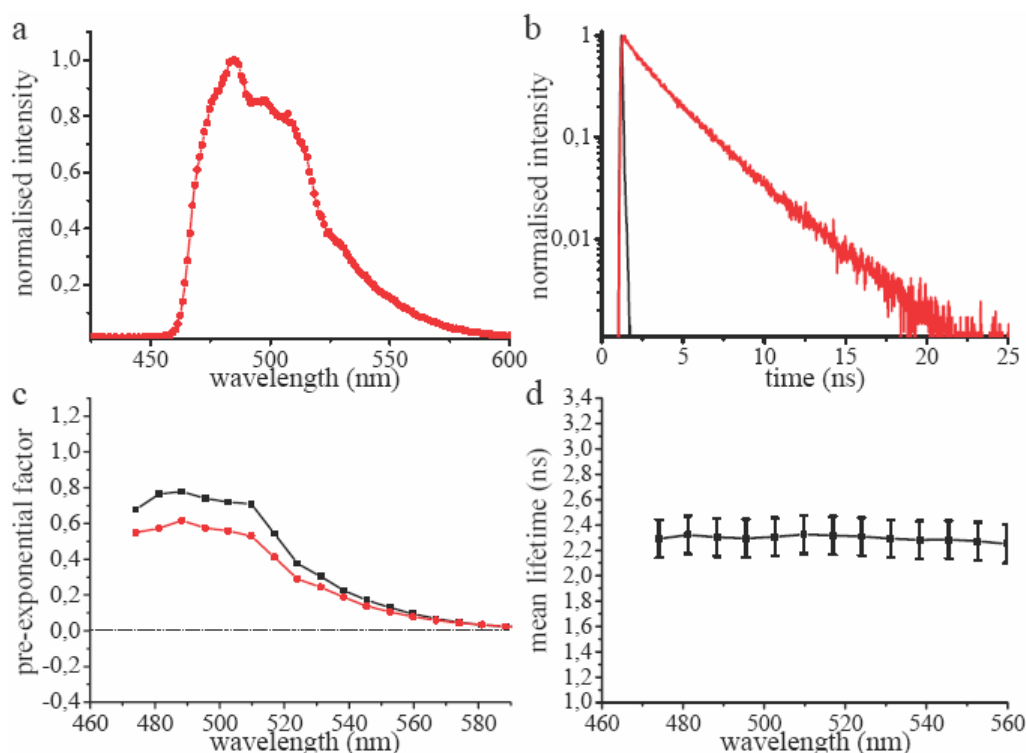
Fig. 4.3.5 *Fluorescence emission dynamics of Cerulean-Bsn1692-3263 in living neurons at DIV 9 (n=8). The fluorescence dynamics were similar in young and mature neurons. a) The fluorescence emission maximum was observed at 486 nm. b) A biexponential fluorescence decay was observed irrespective of the age of the neuron measured. c) DAS of Cerulean- Bsn1692-3263 in living neurons. Intensity decays were analysed in 17 emission bands from 470 nm to 590 nm and the pre-exponential factors of lifetimes, τ_1 (black) and τ_2 (red) (Table 4.3.1) were plotted along the wavelength. The pre-exponential factors showed only positive values for all the lifetimes. d) Mean lifetimes of each emission band was plotted along the wavelength. No deviations along the spectra were observed.*

4.3.4 Interaction studies of Bassoon and CtBP1 in living hippocampal neurons by FRET-FLIM

Neurons co-expressing Cerulean-Bsn1692-3263 and Citrine-CtBP1 were imaged at two different stages of development, namely DIV 9 and DIV 16. Similar to the donor probe alone, the fluorescence dynamics for the expressed protein pair was comparable at both stages. The donor fluorescence emission maximum was observed at 486 nm with a Citrine enhancement at 529 nm (Fig. 4.3.6a).

The fluorescence emission was collected from regions close to the nucleus, where an enrichment of proteins was observed indicating the Golgi network, by closing the iris. The

fluorescence decays yielded lifetimes of 3.23±0.05 ns (τ_1), 1.47±0.12 ns (τ_2) and 0.25±0.09 ns (τ_3), the maximum contribution being observed for τ_2 (Table 4.3.1, Fig. 4.3.6b). DAS displayed negative amplitudes for τ_2 at the acceptor emission maxima (Fig. 4.3.6c). At the same, τ_1 and τ_2 exhibited contributions of 81±3% and 14±9% with τ_3 contributing <10%. The differences in the contributions were evident from the plots of normalised fractional contributions of individual lifetimes. Consequently, the mean lifetimes increased from 1.43±0.15 ns to 2.83±0.08 ns along the spectra from the donor to the acceptor emission maxima (Fig. 4.3.6d). The kinetics at the Golgi network was similar, irrespective of the maturation stage of neurons.
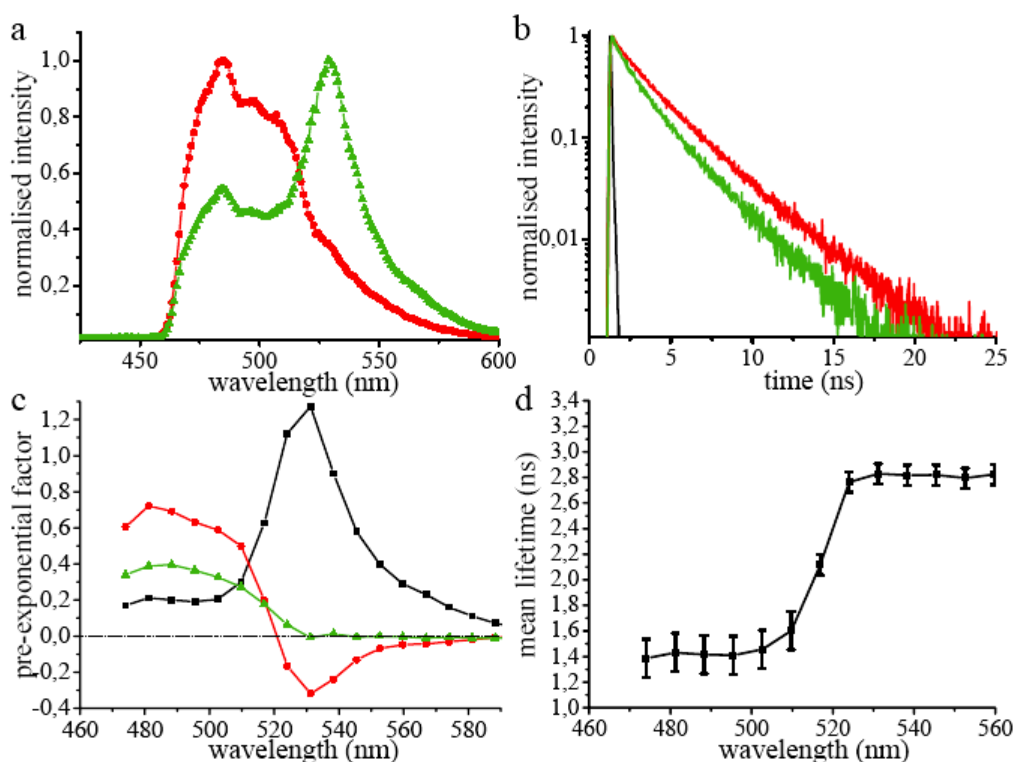
Fig. 4.3.6 *Fluorescence emission of Cerulean-Bsn1692-3263 in the absence and presence of Citrine-CtBP1 in Golgi complexes of living neurons at DIV 9 (n=8). a) Comparison of fluorescence emission spectra of Cerulean-Bsn1692-3263 (red) with the FRET sample (green). A significant Citrine enhancement was observed in presence of FRET. b) Fluorescence decay of Cerulean-Bsn1692-3263 in the FRET sample (green) was shorter compared to the control (red). IRF is shown in black. c) DAS of the FRET sample, Cerulean-Bsn1692-3263+Citrine-CtBP1. The pre-exponential factors of lifetimes, τ_1 (black), τ_2 (red) and τ_3 (green) (Table 4.3.1) were plotted along the wavelength. Negative amplitudes were observed for τ_2 at the acceptor emission maximum in presence of FRET. d) Mean lifetimes of each emission band was plotted with error bars along the wavelength for the FRET sample.*

The cells were also measured using the imaging detector which showed similar results as observed with the point detector. Negative pre-exponential factors (<3%) were observed for τ_2. The imaged cells were fixed and immunostained with antibodies against syntaxin6, a trans-Golgi marker, which specifically identified the colocalised complexes of Bassoon and CtBP1 in the trans-Golgi network of neurons (Fig. 4.3.7c). Bassoon and CtBP1 enriched

complexes did not show entire overlap with trans-Golgi markers, consistent with previous studies on the distribution patterns of Bassoon (Dresbach et al., 2003; Dresbach et al., 2006).
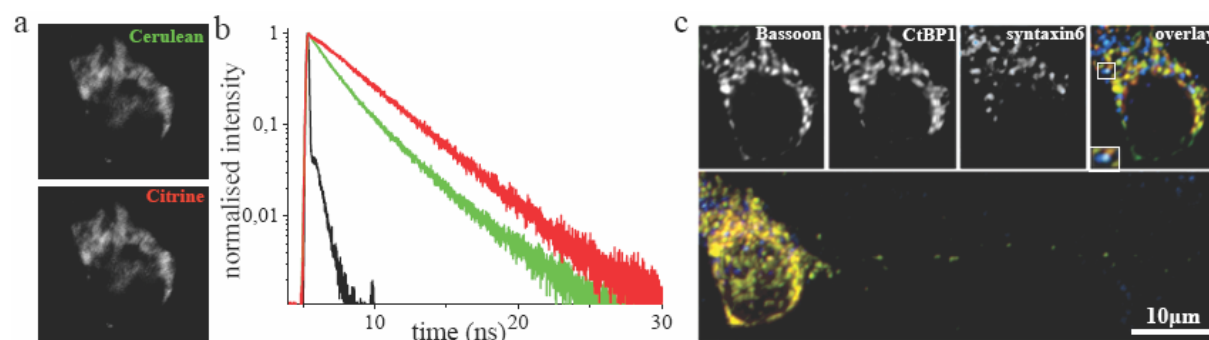
Fig. 4.3.7 Neurons at DIV 9 co-expressing Cerulean-Bsn1692-3263 and Citrine-CtBP1 as measured by the imaging detector. a) The fluorescence emission was split up into Cerulean-Bsn1692-3263 and Citrine-CtBP1 emission bands as shown. The cell body of neurons were focussed to obtain the emission dynamics from the Golgi apparatus by closing the iris. b) In presence of energy transfer, Cerulean-Bsn1692-3263 (green) showed a short fluorescence decay with a simultaneous rise for Citrine-CtBP1 (red) with negative amplitudes for τ_2 (Fig. 4.3.6c). IRF is shown in black. c) The imaged cells were fixed and immunostained with syntaxin6, a trans-Golgi marker. Confocal images were obtained from similar regions as measured by FLIM. In the overlay image, Cerulean-Bsn1692-3263, Citrine-CtBP1 and syntaxin6 are shown in green, red and blue, respectively. Some overlapping spots in white were observed, as indicated in the window of the overlay image. There was no entire overlap, consistent with previous reports. The top panel represents images from a single confocal plane. A confocal stack of the same cell was collected and a maximum projection image is shown in the lower panel.

Table 4.3.1 Fluorescence dynamics of Cerulean in living hippocampal neurons in the absence and presence of FRET as well as at different subcellular compartments.

Construct	ROI	n	τ_1%	τ_1 (ns)	τ_2%	τ_2 (ns)	τ_3%	τ_3 (ns)	τ_{mean} (ns)
Cerulean-Bsn1692-3263	cell body	8	59±3	3.14±0.14	41±3	1.29±0.16	-	-	2.32±0.15
Cerulean-Bsn1692-3263 + Citrine-CtBP1	golgi	8	19±3	3.23±0.05	51±4	1.47±0.12	30±4	0.25±0.09	1.43±0.15
Cerulean-Bsn1692-3263 + Citrine-CtBP1	synapses	5	25±6	3.29±0.04	44±5	1.29±0.11	31±3	0.16±0.04	1.44±0.16

Measurements were taken using the point detector. ROI denotes the region of interest selected for FLIM measurements. Co-expression of Bassoon and CtBP1 resulted in FRET at different subcellular compartments of neurons. In all the cases, the mean lifetimes at the donor emission maxima were significantly reduced, compared to the donor control. n denotes the number of imaged cells. The lifetimes are denoted as τ_1, τ_2 and τ_3 and their corresponding contributions as τ_1%, τ_2% and τ_3%, respectively. τ_{mean} is the corresponding mean lifetime at the donor emission maxima.

The fluorescence emission from processes of mature neurons at DIV 16 expressing Cerulean-Bsn1692-3263 and Citrine-CtBP1 were collected to study the interactions at synapses. As observed in the neuronal cell body, a Citrine enhancement in the emission spectra was observed at the protein complexes in axons (Fig. 4.3.8a). The fluorescence decays

revealed lifetimes of 3.29±0.04 ns, 1.29±0.11 ns and 0.16±0.04 ns, slightly different from those exhibited at the Golgi network (Fig. 4.3.8b). Differences in contributions of the lifetimes were also observed with slightly decreased contributions of τ_2 and simultaneous increase in τ_1, whereas τ_3 remained unchanged (Table 4.3.1). τ_2 displayed negative pre-exponential factors at the acceptor emission peak (Fig. 4.3.8c). Similar to the kinetics at the Golgi network, the plots of normalised fractional contributions exhibited increasing contributions of τ_1 and simultaneous decrease for τ_2 and τ_3, along the spectra. At the acceptor emission maxima, τ_1 and τ_2 showed contributions of 84±6% and 10±4%, respectively, with τ_3 contributing <10%. As a result, the donor mean lifetime of 1.44±0.16 ns was increased to 2.89±0.14 ns at the acceptor emission maxima (Fig. 4.3.8d).
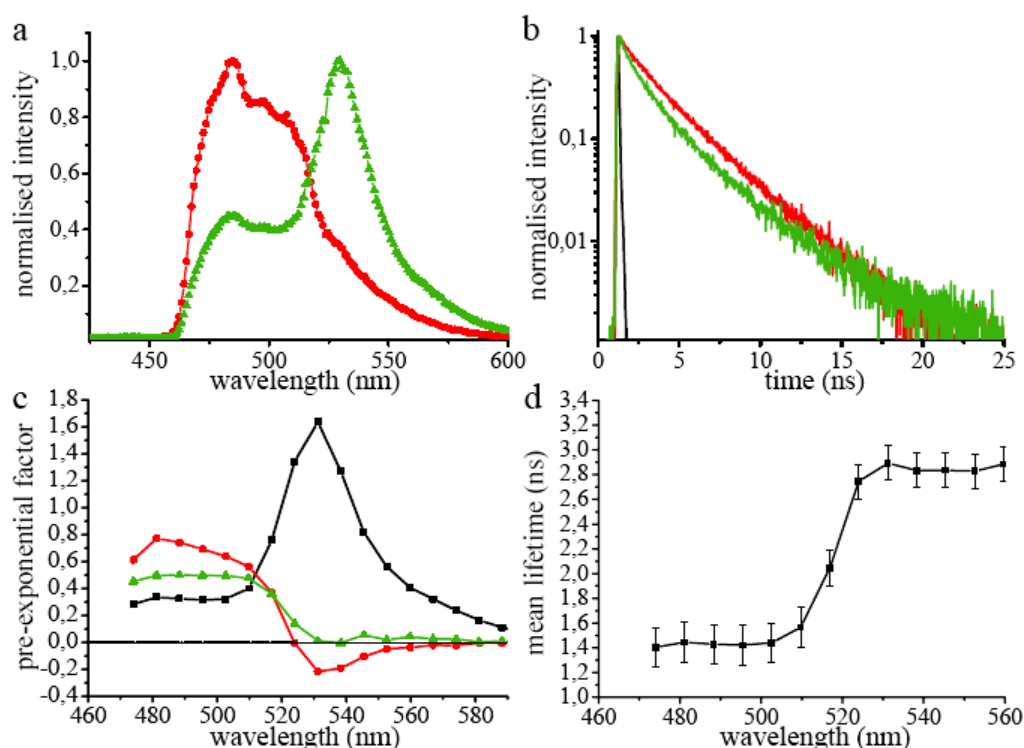
Fig. 4.3.8 *Fluorescence emission of Cerulean-Bsn1692-3263 in the absence and presence of Citrine-CtBP1 in synapses of living neurons at DIV 16 (n=5). a) Comparison of fluorescence emission spectra of Cerulean-Bsn1692-3263 (red) with the FRET sample (green). A significant Citrine enhancement was observed in presence of FRET. b) Fluorescence decay of Cerulean-Bsn1692-3263 in the FRET sample (green) was shorter compared to the control (red). IRF is shown in black. c) DAS of the FRET sample, Cerulean-Bsn1692-3263+Citrine-CtBP1. The pre-exponential factors of lifetimes, τ_1 (black), τ_2 (red) and τ_3 (green) (Table 4.3.1) were plotted along the wavelength. Negative amplitudes were observed for τ_2 at the acceptor emission maximum in presence of FRET. d) Mean lifetimes of each emission band were plotted with error bars along the wavelength for the FRET sample.*

The imaging detector was used to confirm FRET in different subcellular compartments of cells, including synapses in the neuronal processes (Fig. 4.3.9). The deduced lifetimes showed minor changes from those measured using the point detector. In this case, τ_2 displayed smaller negative amplitudes (<1%) in the acceptor channels, compared to the previous measurements in the Golgi network. Since the excitation wavelength of 420 nm was

optimal for excitation of Cerulean alone and not for Citrine (<5%), the complexes in the Citrine channel of the QA image (Fig. 4.3.9a) corresponded to those complexes where FRET was observed. The imaged cells were fixed and immunostained with antibodies against SAP90/PSD95, a post-synaptic marker, which specifically identified many of the colocalised complexes of Bassoon and CtBP1 to be synapses (Fig. 4.3.9c).
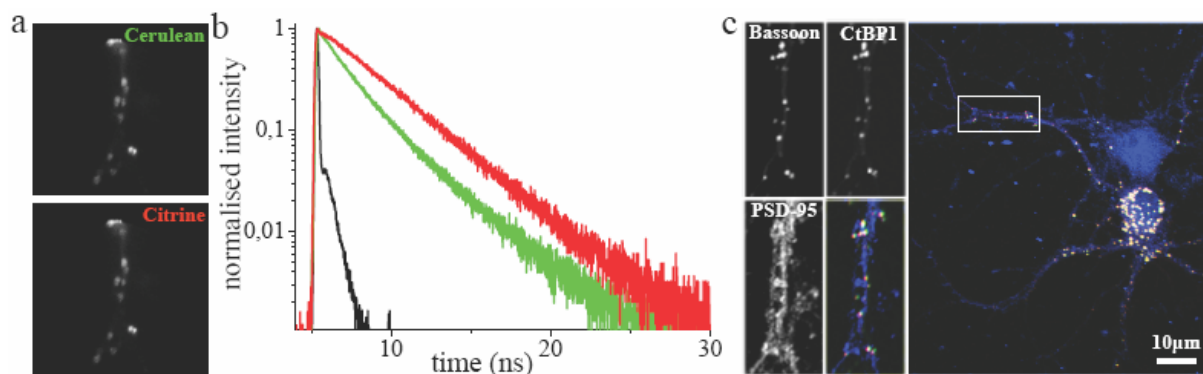
Fig. 4.3.9 Neurons at DIV 16 co-expressing Cerulean-Bsn1692-3263 and Citrine-CtBP1 as measured by the imaging detector. a) The fluorescence emission was split up into Cerulean-Bsn1692-3263 and Citrine-CtBP1 emission bands as shown. The processes of neurons were focussed to obtain the emission dynamics from synapses. b) In presence of energy transfer, Cerulean-Bsn1692-3263 (green) showed a short fluorescence decay with a simultaneous rise for Citrine-CtBP1 (red), with negative amplitudes for τ_2 (Fig. 4.3.8c). IRF is shown in black. c) The imaged cells were fixed and immunostained with SAP90/PSD95, a post-synaptic marker. Confocal images were obtained from similar regions as measured by FLIM. In the overlay image, Cerulean-Bsn1692-3263, Citrine-CtBP1 and SAP90 are shown in green, red and blue, respectively.

Thus interaction studies of Bassoon and CtBP1 were confirmed by FRET-FLIM in different subcellular compartments of neurons including the Golgi network as well as synapses, which in turn was corroborative with the model of a co-transport of the presynaptic proteins as a single prefabricated complex from the trans-Golgi network to the synapses.

The current investigation on presynaptic active zone formation is published in (Jose et al., 2007a).

5 DISCUSSION

5.1 Discriminating FRET from other excited state reactions

FRET-FLIM studies along neuronal development are challenging due to the different cellular effects involved, limiting the feasibility of this technique. Further, the existence of the different molecular conformations of the fluorophores makes FRET determination using lifetime imaging very difficult inside a cell (Chen et al., 2003; Elangovan et al., 2002; Tramier et al., 2002; Tramier et al., 2004). Monitoring the donor mean lifetimes alone does not give enough information regarding the sources of individual lifetimes which could take part in energy transfer or in other excited state reactions. In the present study, the pre-exponential terms or contributions of a given fluorescence lifetime as a function of wavelength (Decay Associated Spectra/DAS) were used to characterise the changes in the biophysical properties with the help of simultaneous donor-acceptor detection and analysis. This approach which has been used successfully in solutions (Loefroth, 1986) was extended to biological samples, where it helped to discriminate deviations in fluorescent properties of probes due to excited state reactions from other cellular effects. Apart from their complicated photophysics, ECFP and EYFP are used as a common FRET pair to study protein-protein interactions in cells by fusing to the respective proteins of interest (Evans and Yue, 2003; Karpova et al., 2003) and in development of FRET based fluorescent protein biosensors like Cameleon (Habuchi et al., 2002; Miyawaki et al., 1997; Truong et al., 2001), Clomeleon (Kuner and Augustine, 2000) etc. Studying the photophysics of these probes in controlled conditions and a comparison of the properties with those observed in cells was essential for a clear understanding of the deviations of the measured parameters to discriminate FRET.

The quenching effects on intensity of GFPs due to acidification have already been reported (Llopis et al., 1998), though their effect on lifetimes has not yet been deeply investigated. The biexponential decay of purified CFP with lifetimes of 3.26 ± 0.10 ns (τ_1) and 1.12 ± 0.03 ns (τ_2) was changed to 3.09 ± 0.09 ns (τ_1), 1.38 ± 0.08 ns (τ_2) and 0.28 ± 0.06 ns (τ_3) at acidic pH levels. According to our kinetic model of CFP, the unperturbed τ_1 of CFP (3.3 ns) and the 1st emission maxima originates from its 1st conformation, whereas the unperturbed τ_2 (1.1 ns) of CFP as well as the 2nd emission peak arises from its 2nd conformation (Nair et al., 2006). This was in agreement with the observation of reduction of contribution of τ_1 of ECFP along the spectra, with a simultaneous increase of τ_2 (Fig. 4.1.2f). It could be assumed that the individual conformations of CFP take part in quenching independently (Borst et al., 2005). There are different amino acid residues in CFP which could account for its complex pH

sensitivity (Guerrero and Isacoff, 2001). From the effects observed in solution at 0mM Cl⁻, the 1st conformation of CFP was concluded to be most affected by quenching at acidic pH levels. Such a difference in quenching effects for the two lifetimes could arise only if the folding of the 2nd conformation of CFP is in such a way as to introduce a steric shielding for the respective amino acid residues from the quenchers. This model was also in agreement with the deviations in the emission spectra of CFP at 0mM Cl⁻ at varying pH levels (Fig. 4.1.1a). Lesser quenching of the 1st conformation of CFP was revealed at higher pH levels, resulting in a higher ratio for the major peak of CFP at 486 nm compared to its shoulder. However, if the quenching of τ_1 of CFP (3.3 ns) would result in lifetimes close to the unperturbed τ_2 of CFP (1.1ns) as displayed at low pH levels, this would in turn reduce the quenching effects observed for the resulting lifetime (1.38 ns) due to the contribution of unquenched τ_2, as observed.

A developmental shift in the fluorescence dynamics of ECFP was observed, where in young hippocampal neurons ECFP displayed a three exponential fluorescence decay (Table 4.1.1). This was in contrast to its typical biexponential nature (Tramier et al., 2004) as observed in the major fraction of mature neurons, resulting in an overall increase in the mean lifetime of ECFP along neuronal development. The source of this short lifetime component of 0.29 ns for CFP could be explained by the difference in the pH levels of the cells, which shows a shift with maturation (Bevensee et al., 1996). It was reported that pH levels in immature neurons shows a Gaussian distribution with a mean of 6.95±0.025, whereas in mature neurons, two populations of neurons are observed with pH levels of 6.68±0.007 and 7.32±0.21 (Bevensee et al., 1996). This was consistent with the mean lifetimes of CFP calculated for the two groups of neurons from the values observed in solution at different pH levels, namely 6.5 and 7.3 for groups I and II, respectively. The multiple lifetimes in neurons were also similar to those observed in solution at different pH levels with the shortest lifetime component arising at acidic pH levels (<7.0). This was also corroborative with the deviations in the emission spectra of ECFP, where an increase in the contribution of its red shifted shoulder at 505 nm was observed on lowering the pH (Figs. 4.1.1a, 4.1.2a).

A comparison of our results with the previous reports (Bevensee et al., 1996) showed a developmental shift of pH and chloride in different fractions of neurons. This could in turn indicate overlapping fractions, as observed from our results in cells and solution. The differences in the fluorescence dynamics of ECFP observed with neuronal development due to effects like quenching have to be taken into account when studying interactions in living

cells, since the reduced donor mean lifetimes or the presence of a third lifetime component could be misinterpreted as the presence of energy transfer.

5.2 Photophysics of Clomeleon

Quenching effects were observed for purified Clomeleon on increasing the chloride concentrations (Fig. 4.1.3a). At 0mM Cl⁻, only the shortest lifetime component (τ_3) displayed negative pre-exponential factors (Fig. 4.1.4d) in contrast to the other chloride concentrations, where both the short lifetime components (τ_2 and τ_3) were involved in FRET. This would indicate an involvement of both conformers of CFP in energy transfer, probably displaying different quenching patterns (Nair et al., 2006). The increase in donor mean lifetimes with chloride indicated lowering of FRET in Clomeleon in these conditions (Fig. 4.1.3 e). In the acceptor channels, the drastic decrease in the contribution of τ_1 indicated significant quenching of Topaz on increasing the chloride concentrations. Consequently, the mean lifetimes of Clomeleon in the acceptor channels were observed to approach mean lifetimes of CFP at high chloride concentrations (Fig. 4.1.3 e).

The high quenching effect of Topaz could be explained by its static quenching due to the possibility of its direct binding to chloride ions (Kuner and Augustine, 2000). In this case, bound or contact quencher complexes would be present in the ground state, which compete with the ground state of Topaz for incident excitation. This would in turn yield excited acceptor-quencher complexes whose excitation results in instantaneous quenching on absorption (Birks, 1970). This was also in agreement with the observation that Clomeleon at high chloride concentrations, on direct excitation for steady state imaging, showed reduced fluorescence with the YFP filter. Also, no additional lifetimes were observed in the acceptor channels on increasing the chloride concentrations. Further, the chloride association from the bulk solution might favour protonation and thereby reduce the fluorescence of Topaz (Guerrero and Isacoff, 2001). The high static quenching of Topaz would override the possibility for Clomeleon to show FRET. Depending on the prevalent effects, the overall fluorescence properties of Clomeleon were altered. The lifetimes of Clomeleon remained unchanged in presence of high quenching effects too, since no conformational change was involved.

The pH effects on the fluorescence emission spectra of Clomeleon were significant. At 0 mM Cl⁻, R values decreased to less than 50% at acidic pH levels (Fig. 4.1.3b). The fluorescence lifetimes of Clomeleon approached those of CFP at low pH levels, indicating the absence of FRET. The fractional contributions of τ_3 were higher at pH levels <6.5 and >7.2

due to the different excited state reactions involved. A reverse effect with decreased contribution of τ_1 was observed for the same, whereas τ_2 remained relatively unaffected (Fig. 4.1.3d). At low pH levels Clomeleon exhibited high quenching effects similar to CFP, whereas at high pH levels FRET was significant. As a result, a Gaussian distribution was observed for the donor mean lifetimes around pH 6.9 (Fig. 4.1.3f). The unperturbed kinetics of digested Clomeleon under varying chloride concentrations and pH levels excluded the possibility of any additional lifetimes in the acceptor channels arising due to quenching effects of Topaz, as expected.

The observation of negative amplitudes for τ_2 and τ_3 of Clomeleon at chloride concentrations (>0mM) indicated the participation of both conformations of CFP in FRET. Since it was not possible to discriminate which among the CFP conformers was the source of the shortest FRET lifetime (τ_{DA}), distance calculations were done using both probabilities. Assuming that the FRET lifetime of 0.21 ns arises from the quenching of the 2nd conformation of CFP (1.1 ns), such a calculation yielded the efficiency to be 80% and consequently the distance r to be 3.9 nm. Distance calculations using conventional mean lifetimes were not possible due to the presence of free CFP conformers not involved in energy transfer. The fluorescence characteristics of both CFP and Topaz were perturbed due to pH effects. Further, the changes in the absorption spectra of Topaz due to the binding of chloride ions would influence the R_0 values. Therefore, the distance determination in Clomeleon was performed only at 0mM Cl$^-$ at pH 7.4.

τ_1 of Clomeleon can be taken as the unperturbed donor lifetime which is not involved in any excited state reaction. This can be considered as the subpopulation of one of the CFP conformers that are unquenched. Calculation of mean lifetime of Clomeleon excluding this contribution of free conformers yielded τ_{DA}=0.57 ns. Using τ_{mean} of CFP under similar conditions (0mM Cl$^-$, pH 7.4) as τ_D, FRET efficiency of Clomeleon was calculated to be 76.5% which in turn yielded r=4.0 nm, close to the values calculated from the multiple lifetimes of the assumed model (3.9 nm). The slight increase in this value could be explained by the presence of the second set of unquenched conformers of CFP (giving rise to the unperturbed lifetime τ_2), whose resolution was much more complicated. According to the previous assumption, this lifetime would be close to the quenched lifetime from τ_1, beyond the discriminating capability of any currently used multi-exponential analysis methods.

However, the degree of competition between FRET and quenching of CFP can be understood by comparing the dynamics of purified CFP and Clomeleon under varying pH conditions. It was observed that the quenching of CFP at pH 7.0 resulted in a reduction of its

mean lifetime to 2.23 ns (0mM Cl⁻, Fig. 4.1.1d), whereas in presence of FRET at the same conditions, this was reduced down to 1.43 ns (Fig. 4.1.3f). Therefore the presence of energy transfer significantly affected the fluorescence dynamics of CFP compared to the quenching by acidic pH levels, as expected. The unperturbed mean lifetime of CFP at pH 8.0 was observed to be 2.5 ns (Fig. 4.1.1d). The FRET efficiency of Clomeleon was calculated with the unperturbed as well as the quenched lifetimes of CFP at different pH levels, which yielded 43% and 36%, respectively. The difference of 7% indicated the efficiency of excited state reactions of CFP excluding FRET. The quenching effects on CFP excluding FRET increased from 0% to 18% on lowering the pH from 8.0 to 6.0, whereas the FRET efficiency of Clomeleon decreased from 64% to 38% in similar conditions. The differential effects on Clomeleon under varying conditions revealed that the quenching effects as well as energy transfer for the two conformations of CFP could be independent from each other.

5.3 A ratiometric and lifetime chloride indicator during neuronal development

The multiple lifetimes of Clomeleon were constant throughout development, indicating that no conformational change was involved (Table 4.1.2). The contributions of the individual lifetimes and their spectral spread showed clear differences along development (Table 4.1.2, Figs. 4.1.6, 4.1.7), thereby resulting in an overall decrease and a simultaneous increase in the mean lifetimes at the donor and acceptor emission maxima with maturation (Figs. 4.1.6f, 7f, 7i). The pre-exponential factors of the individual lifetimes showed only positive values for all cells at DIV 7 (Fig. 4.1.6d) similar to ECFP (Fig. 4.1.2c), whereas the contributions of τ_2 and τ_3 showed negative values for the majority of mature neurons (Fig. 4.1.7g). Such a change in sign or negative amplitudes for the lifetimes at the acceptor emission maxima could arise only due to the presence of energy transfer (Lakowicz, 1999). The fractional contributions of individual lifetimes also differed between cells showing high FRET efficiency from those which do not. In the former, the contribution of τ_1 increased drastically along the wavelength axis combined with a simultaneous decrease of τ_2 and τ_3 (Fig. 4.1.7h), whereas in the latter, no significant change was observed (Figs. 4.1.6e, 4.1.7e).

For mature neurons, fluorescence lifetime analysis revealed higher FRET with negative values for the pre-exponential factors of τ_3 at the cell periphery, as indicated by TIRF studies (Figs. 4.1.8a-d). The expression of the potassium chloride cotransporter KCC2 at the plasma membrane of a mature neuron (DIV 15) could account for the lower chloride concentrations at the cell periphery, as measured by FLIM (Figs. 4.1.8f). In the imaging detector, negative pre-exponential factors were observed only for τ_3, in contrast to the

measurements from the point detector. This could be accounted by the lack of wavelength resolution in the imaging detector due to the usage of bandpass filters for collecting the donor and the acceptor fluorescence, with unavoidable cross-talk between the channels. When measuring in different intracellular compartments, though the influence of pH or of varying refractive indices on lifetimes could not be avoided, negative amplitudes for the individual lifetimes at the acceptor emission maximum arose only in presence of FRET.

The classification of neurons in the present work was based on the *R* values of individual cells. The subpopulations of cells, namely the presence of excitatory (pyramidal) and inhibitory (interneurons) neurons were not individually considered. Since both these groups exhibited high intracellular chloride concentrations at young stages which lower on maturation, the majority of neurons were expected to belong to class I at DIV 7 which shifted to classes II and III with maturation (DIV 15). Further, in dissociated hippocampal cultures <20% of interneurons were expected. Since no deviation was observed in the measured results from those expected, further classifications were not considered for a detailed study.

The fluorescence decay of Clomeleon measured in COS-7 cells (pH 7.4) yielded lifetimes similar to those observed in neurons with the contributions and mean lifetimes similar to the class showing highest *R* values at DIV 15 or the lowest intracellular chloride concentrations (Table 4.1.2). This was also in agreement with the measurements of ECFP in COS-7 cells where the mean lifetimes were similar to those observed for the majority of mature neurons, indicating similar chloride and pH levels for both (Table 4.1.1).

Since the donor CFP itself shows heterogeneity in its lifetimes along development of neurons, a direct calculation of FRET efficiency or chloride determination from the absolute donor or acceptor lifetimes can be misleading. In this regard, chloride calculations from ratiometric parameters like *R* are better conceivable since they average out these different effects to a good extent and will thereby be less affected. Utilising this possibility, the ratios of acceptor to donor mean lifetimes were calculated from purified Clomeleon at pH 7.4 under varying chloride conditions (Fig. 4.1.9d) and compared with those obtained from the different fractions of neurons at a particular maturation stage, namely DIV 15. According to previous reports, though heterogeneity in pH levels between individual neurons is to be expected, the majority of cells at this stage would exhibit pH levels close to 7.4 and thereby be comparable (Bevensee et al., 1996). This in turn resulted in similar values of intracellular chloride concentrations from the ratio of lifetimes with those calculated from *R* values, namely 61±14mM and 48±4mM for class I and 14±1mM and 15±4mM for class III, respectively. In the minor fraction of mature neurons of class I, FRET was hindered due to high intracellular

chloride concentrations as well as at low pH levels, accounting for the high deviations observed. Since the lifetimes obtained from neurons were not measured under regulated conditions, more precise calculations were not possible due to the differential influences of pH on CFP and Topaz.

Thus Clomeleon was used for the first time as a ratiometric lifetime indicator for chloride, which was successful under comparable pH conditions. Usage of pH insensitive probes like Sapphire (Zapata-Hommer and Griesbeck, 2003) and photostable donors like Cerulean (Rizzo et al., 2004) in the ratiometric biosensors would make such direct calculations of intracellular ionic concentrations in living cells more feasible.

5.4 Kinetic model for simultaneous quenching and FRET

The fluorescence dynamics of Clomeleon and Cameleon were studied simultaneously to understand the mechanism of how energy transfer occurs in presence of quenching effects of the solvent. Strong quenching effects were observed for Clomeleon at high chloride concentrations as well as at low pH levels. In Clomeleon, the presence of these two quenching effects overrode the possibility for energy transfer, though CFP and Topaz were well within the FRET distance. The observation of decrease in FRET in Clomeleon at high chloride levels and low pH levels were probably due to three different reasons: a) incapability of CFP to donate energy; b) incapability of Topaz to accept energy; c) incapability of Topaz to emit energy. The fluorescence dynamics of Cameleon in young neurons showed that even in presence of quenching effects due to high anionic concentrations and low pH levels, FRET could be observed. This would indicate that even in presence of quenching, energy transfer was possible from the donor molecule. Thus the possibility to observe FRET would purely depend on the sensitivity of the acceptor to the ionic effects, either to absorb or emit. This was very well the case of Cameleon where Citrine was expected to be more stable as well as less sensitive to ions compared to Topaz. The observation of increase in donor mean lifetimes of Clomeleon with increasing chloride concentrations indicated the absence of transfer of energy from CFP to Topaz at high chloride levels. Comparing with the results on Cameleon, this reduction in FRET would be due to the incapability of Topaz to accept energy from CFP rather than the failure of CFP to donate in these conditions, quenching the Topaz emission significantly. It is still to be known whether the formation of excited acceptor-quencher complexes would influence its direct excitation or also the energy transfer. The results confirmed that the biophysical properties of Clomeleon depended on the properties of Topaz alone and not on CFP, though the quenching effects were observed for the latter too, making

it a suitable optical indicator for ratiometric studies inside a living cell. Thus, with the current work it was possible to arrive at a model which could explain the mechanism of how competitive quenching effects as well as excited state reactions present in a single molecule could affect its biophysical properties.

5.5 FRET-FLIM for probing interactions of active zone proteins

FRET determination by FLIM using fluorescent tagged proteins is highly affected by the presence of endogenous interaction partners. This makes FRET studies highly intricate and complex in a real system. Donor decay analysis alone is not always sufficient to discriminate energy transfer from other excited state reactions. Acceptor analysis with changes in the amplitudes of the lifetimes provide a much better background for FRET discrimination, though it is highly determined by the FRET efficiency which is in turn affected by the number of interacting molecules. Thus, a method had to be adopted for studying interactions in real cell conditions without compromising the possibility for understanding FRET in these conditions. Therefore, COS-7 cells which express endogenous CtBP1 but no Bassoon were adopted as a suitable system. This also provided a better cellular environment for biophysical studies compared to neurons since the photophysical properties of the fluorescent probes were observed to be significantly affected in presence of varying ionic concentrations in neurons (Jose et al., 2007b), as discussed previously in Section 5.1. Fusion proteins of Bassoon and CtBP1 with modified GFP variants like Cerulean and Citrine were used for the investigation.

Cerulean, a recently developed fluorescent probe is a photostable variant of CFP (Rizzo et al., 2004). Based on our previous findings, it was important to investigate the donor probes in similar conditions as FRET samples for determining the relevance of deviations in the biophysical properties studied. COS-7 cells expressing Cerulean revealed biexponential fluorescence decay with similar lifetimes as CFP (Tramier et al., 2002). The advantages of FRET determination by donor excitation and simultaneous analysis of donor and acceptor emission were signified by co-expressing Cerulean with a stable variant of YFP called Citrine. The decay kinetics of this mixture was not different from that of Cerulean itself, proving this as a suitable control (Table 4.2.1, Fig. 4.2.3). The lack of changes in the DAS for the lifetimes of the mixture also confirmed the absence of any excited state reaction (Figs. 4.2.3d, g). The advantage of confirming the sources of individual lifetimes from DAS was further affirmed from the direct excitation of Citrine at 420 nm, which showed the source of the short lifetime component to be cell autofluorescence and not the Citrine chromophore

(Fig. 4.2.4c). This was also in agreement with the high variability associated with this component in contrast to the 3.20 ns lifetime of Citrine. This could be well expected since the excitation maxima of Flavins was 435 nm, whereas Citrine was excited <5% at the excitation wavelength used in the set up (Lippincott-Schwartz and Patterson, 2003).

Cerulean-Bsn1692-3263 exhibited more complex behaviour with the presence of a shorter lifetime component in the fluorescence decay (Table 4.2.1, Fig. 4.2.6b). This was in agreement with previous reports on the aggregating nature of the protein in non-neuronal cells (Dresbach et al., 2003). Fluorescence characterisation of the different deletion constructs of Bassoon traced this property of aggregation to the second CC of the protein. The comparison of the fluorescence dynamics of Cerulean alone with its fusion constructs with CtBP1 and Bsn1692-3263 clearly showed how the properties of a fluorescent probe depend on the protein component to which it is fused (Figs. 4.2.5, 4.2.6). In the presence of Citrine-CtBP1 FRET was observed with Cerulean-Bsn1692-3263, where the DAS showed negative pre-exponential factors for $\tau 2$ indicating the better involvement of this lifetime in energy transfer (Fig. 4.2.6g). The change in sign at the acceptor emission maxima evolved only due to presence of energy transfer (Lakowicz, 1999). Comparison of contributions of lifetimes further affirmed the suitability of the present approach, whereby FRET could be distinguished even in presence of additional multi-exponential components from the donor (Table 4.2.1, Fig. 4.2.6h).

Using the point detector, the fluorescence dynamics of the whole cell in the field of illumination was obtained. For a better understanding of the Bassoon-CtBP1 interaction at individual puncta, recordings were done using the imaging detector whereby we could define small ROIs corresponding to groups of these complexes (Fig. 4.2.7). This in turn gave deeper information regarding the protein interactions inside a cell at normal conditions. In this case, the influence of cell autofluorescence was negligible and the fluorescence dynamics showed slight deviations from the whole cell as expected. Nevertheless, negative amplitudes were observed for τ_2 even in presence of cross talk between Cerulean and Citrine using the band-pass emission filters which restricts these observations to a large extent.

Using our new approach of distance calculations excluding the contribution of free conformers of donor not participating in FRET (Section, 5.3, (Jose et al., 2007b)), the inter-chromophore distance between Cerulean and Citrine tagged interacting proteins were calculated and compared with the calculations from multiple lifetimes (Section 4.2.4). τ_1 of co-expressed cells (Table 4.2.2) indicated the major contribution of Cerulean conformers not involved in any excited state reaction. Exclusion of this major contribution yielded mean

lifetimes of donor in presence of FRET to be 1.02 ns (τ_{DA}). Using mean lifetimes of Cerulean-Bsn1692-3263 alone (Table 4.2.2) as τ_D, the FRET efficiency and the corresponding inter-chromophore distance r were calculated to be 49% and 5.0 nm, respectively, well in agreement with the calculations using multiple lifetimes and further verifying our assumptions. Thus with a combination of FLIM and FRET, we were successful in proving direct physical interactions between Bassoon and CtBP1 in macromolecular complexes for the first time in living cells.

5.6 Bassoon: a backbone in a multiprotein complex linking CtBP1 and CAST

The presence of Bassoon in COS-7 cells completely distorted the endogenous nuclear staining pattern of CtBP1 and resulted in the recruitment of this protein to Bassoon-containing protein complexes in the cytoplasm of these cells (Figs. 4.2.1d-i). Such a recruitment was not observed in case of a mutant construct of CtBP1, signifying the recruitment to be interaction specific and not due to protein overexpression (Figs. 4.2.1j-l). Biochemical studies have shown the possibility for binding of CtBP1 to Bassoon in conventional synapses (tom Dieck et al., 2005). Bassoon and CAST are observed to be colocalised in synapses and partly on PTVs (Takao-Rikitsu et al., 2004), though the possibility for simultaneous binding of different interaction partners including CtBP1 has not been proven. The relevance amplified in the case of a short construct of Bassoon capable of co-recruiting its interaction partners (Figs. 4.2.2a-d). Expression of CAST alone in COS-7 cells did not result in disruption of the endogenous nuclear recruitment of CtBP1 (Fig. 4.2.2e-g). FLIM studies of CtBP1 and CAST (Fig. 4.2.8) verified the absence of any direct interaction between the pair in the absence of Bassoon, proving Bassoon to be an essential linker in the formation of such multi-protein complexes linking CtBP1 and CAST and potentially other molecules of the CAZ network inside a cell.

5.7 The presynaptic apparatus: A prefabricated complex transported to synapses?

It has been previously suggested that the presynaptic molecules could be transported as a single preformed complex from the Golgi apparatus to the synapses, though it has not yet been proven. The time-lapse studies in young neurons, where a co-transport of Bassoon and CtBP1 as well as Bassoon and CAST was observed, were in favour of this (Fig. 4.3.4). The observations of three populations of puncta, two of them being mobile, were in agreement with previous studies on mobility characteristics of PTVs. The maximal velocity of the highly mobile puncta were reported to 0.35 μm/s and those of slower ones, 0.1 μm/s (Shapira et al.,

2003). Previous studies have indicated that packets of SVs in developing axons are highly mobile before being recruited to synaptic sites (Ahmari et al., 2000; Hopf et al., 2002). The mobile, bidirectionally moving puncta splitting into smaller puncta or coalescing into less mobile larger clusters has been reported for non-synaptic SV clusters moving along axons (Ahmari et al., 2000; Dai and Peng, 1996; Kraszewski et al., 1995; Matteoli et al., 1992) as well as for GFP-Bsn609-3938 puncta which shows similar characteristics as the full length protein, when expressed in primary cultures (Dresbach et al., 2003; Shapira et al., 2003). This was also the case for Bsn1692-3263 which is recruited to presynapses in neurons, although with somewhat reduced efficacy (Dresbach et al., 2003). The observations also pointed to the hypothesis that PTVs constitute a major form of AZ precursor vesicles and that AZs may be assembled from the unitary insertion of a small number of PTVs into the presynaptic membrane (Bresler et al., 2004; Shapira et al., 2003). The scanning nature of larger complexes, indicating packets of PTVs, was in favour of this model where the termination point of these complexes where they become stationary could indicate synapses. EM micrographs have suggested that PTVs travel along axons - as individual vesicles (Zhai et al., 2001). Our observations that the fastest and smallest puncta appeared to merge into single brighter punctum and vice versa were also in agreement with previous reports that some puncta within the non-synaptic Bassoon and Piccolo populations were in fact pairs or triplets of PTVs (Shapira et al., 2003).

However, not all of the mobile particles seem to be part of the same 'prototerminal' population. A recent study has described another class of mobile presynaptic structures (Krueger et al., 2003). These mobile clusters displayed a capacity for synaptic vesicle release, with functional characteristics similar to those observed at mature presynaptic sites, including increased sensitivity to tetanus toxin and reduced sensitivity to brefeldin A. They occasionally gave rise to small mobile vesicle clusters that move along axons, sometimes merging with nearby presynaptic sites. Furthermore, these clusters were sometimes observed to move from one location to another. Surprisingly, many of these mobile clusters were not juxtaposed to postsynaptic structures, or even to dendrites, but they were associated with the CAZ molecule Bassoon. It was therefore suggested that these mobile structures might be well-formed synaptic vesicle release sites that do not have postsynaptic counterparts, and they were termed 'orphan' release sites. The recycling synaptic vesicle pool of orphan release sites was smaller than that of synaptic release sites, but quantitative analysis indicated that synaptic release sites might contain integer multiples of unitary amounts of recycling synaptic vesicle pools that are associated with orphan release sites. Intriguingly, orphan release sites were sometimes

observed to give rise to new presynaptic sites at axodendritic contacts, indicating that new presynaptic compartments might be assembled from 'units' of synaptic vesicle release machinery that 'bud off' preexisting synapses (Ziv and Garner, 2004). In the present work the larger Bassoon complexes which showed a modest movement, scanning the nearby areas and moving along the axonal process or being stationary possibly forming synapses, could also indicate such preassembled units of synaptic vesicle machinery.

FLIM data from neurons are highly difficult to be interpreted due to the dynamic nature of the cell. Based on our previous studies where the biophysical properties of fluorescent probes were highly deviated depending on the microenvironment to which they were exposed (Jose et al., 2007b), photostable probes like Cerulean and Citrine were adopted.

Neurons expressing the donor fusion construct namely, Cerulean-Bsn1692-3263 was imaged at DIV 9 and DIV 16. The former was optimal for comparable studies in the Golgi apparatus, since it was close to the peak of synaptogenesis and the molecules of interest would be produced and transported from the Golgi network to the synapses. Further, the intracellular ionic concentrations were suitable with higher pH at this stage so that the photophysical properties of fluorescent probes were less affected compared to younger neurons. The studies in mature neurons were essential to compare the dynamics in synapses, in addition to similar studies in the Golgi apparatus. The biexponential fluorescence decay of Cerulean-Bsn1692-3263 in neurons indicated the lower aggregation probability of the construct, when expressed in their natural environment (Fig. 4.3.5). This was in agreement with previous reports where a clustering of Bassoon constructs was observed only in non-neuronal cells and on blocking of Golgi trafficking in neurons (Dresbach et al., 2006). The constant lifetimes and contributions of Cerulean at different stages of neuronal maturation confirmed the photostability of the probe in presence of changing ionic environments, in contrast to CFP.

FLIM studies combined with immunocytochemisty revealed interaction of Bassoon and CtBP1 in the trans-Golgi network of neurons as well as at presynapses (Figs. 4.3.6-4.3.9). Bassoon and CtBP1 did not show entire overlap with the trans-Golgi network since the measurements were carried out at >20°C, so that the proteins were actively exported out of the network as soon as they were assembled and sorted into vesicles. The interacting complexes of Bassoon and CtBP1 in neuronal processes were observed to be synaptic as well as non-synaptic. The observations further supported the model of interaction of the proteins during transport to the presynapses along neuronal axons. The slight differences in lifetimes and their corresponding contributions at different subcellular compartments indicated a

difference in the transfer rate between the fluorophores when involved in different complexes (Table 4.3.1). It was difficult to compare the inter-chromophore distances between the donor and acceptor probes in these complexes directly from the individual lifetimes, since according to our hypothesis the quenching of τ_1 of Cerulean-Bsn1692-3263 would result in lifetimes close to τ_2 of the FRET sample making it difficult to discriminate between the two contributions. Also, the involvement of τ_3 in FRET could not be excluded, though τ_2 alone displayed negative amplitudes at the acceptor emission maxima. Therefore, distance calculations were done using modified mean lifetimes from the multiple components of the fluorescence decay, using our new approach adopted in COS-7 cells (Section 5.5).

Excluding the contribution of free conformers of Cerulean not involved in energy transfer (τ_1), FRET efficiencies were calculated in neurons in different subcellular compartments in which the proteins were present. For interactions in the cell body and processes, τ_{DA} were calculated to be 1.02 ns and 1.38 ns, respectively. τ_1 of Cerulean-Bsn1692-3263 (Table 4.3.1) was taken as τ_D. Using $R_0 = 4.92$ nm for CFP-YFP pairs and a random orientation of dipoles assumed with $\kappa^2 = 2/3$, FRET efficiencies of 57% and 42% were calculated in the Golgi network and synapses, respectively, which yielded the inter-chromophore distances r to be 4.7 nm and 5.2 nm at the same. The results were in close agreement with the distances predicted using molecular modelling of 4.9 nm. Higher FRET efficiency observed at the Golgi network was also corroborative with higher negative amplitudes of τ_2 observed for the same, using the imaging detector. The difficulty to observe negative pre-exponential factors using the imaging detector compared to the point detector, due to its lower wavelength resolution, has already been discussed (Section 5.3). Due to the absence of FRET between Bassoon and CAST in COS-7 cells, most probably due to large distances between the chromophores, similar studies were not done in neurons.

Thus interactions of CAZ associated molecules including Bassoon and CtBP1 were confirmed in the Golgi network and synaptic contacts in living neurons. The findings were consistent with the 'active zone precursor vesicle hypothesis', which suggests that active zone and CAZ molecules assemble into a complex at the Golgi apparatus and are deposited as preformed complexes at nascent synapses from so-called Piccolo-Bassoon-Transport vesicles (Fig. 1.4, (Fejtova and Gundelfinger, 2006; Garner et al., 2002; Ziv and Garner, 2004)). The presence of presynaptic complexes of CAST and CtBP1 recruited by Bassoon in axons and axonal growth cones, the precursors of neuronal contacts, also supported the model of PTVs as 'active zone precursors' (Zhai et al., 2001). The lack of deviations in the biophysical properties of the donor probe alone during neuronal development confirmed the photostability

of Cerulean to differing ionic levels, ensuring it as a suitable FRET donor. Though FRET-FLIM studies in living neurons were highly challenging due to the different cellular influences involved, time-resolved imaging under optimal conditions with proper characterisation resulted in a huge wealth of information regarding cellular signalling pathways, not available by any other existing method.

Thus my PhD work included a deep investigation to study the photophysical effects of ionic shifts along neuronal development on the properties of fluorescent probes as well as interactions of synaptic scaffolding proteins in living neurons. A highly complex microscopic system with non-scanning detectors based on single photon counting for studying FRET using time-domain FLIM was constructed for the purpose. An extensive characterisation of the biophysical and biochemical properties of the proteins involved, including their fluorescent probes, by microscopic, spectroscopic, biochemical, molecular biological and computational techniques allowed to address the different biological questions of interest.

Manuscripts under preparation:

Fluorescence Lifetime Imaging to predict folding of macromolecules in living cells (to be submitted)
Deepak K. Nair, **Mini Jose**, Carsten Reissner, Wolfgang Paster, Werner Zuschratter, Hannes Stockinger, Roland Hartig
Equal authorship

6 EPILOGUE

Neurons are highly dynamic cells, the studies of which poses difficulties for the current imaging techniques, but at the same time makes them all the more interesting. They are the sources of various biophysical phenomena, one of the major events being the switch of GABA from excitatory to inhibitory nature mediated by chloride ions. The effect of cellular ionic regulation on fluorescence properties has made it possible to address this shift in chloride ions using FRET-FLIM. In the present work, chloride regulation in living neurons along development was addressed in cell culture. This would only be a highly simplified example of what could be expected in a living brain, the latter being a synchronised network of millions of neurons, the excitation and inhibition of which have to be in equilibrium to avoid pathological consequences. Though different theories have been proposed on how chloride regulation in brain takes place, the stringent techniques so far adopted poses difficulties for a proper characterisation. Detailed investigation on the role of chloride ions in the developmental switch as well as the differential ionic regulation in multiple populations of neurons and other cell types are still under way. The success of biophysical approaches using genetically encoded biosensors for addressing the intracellular ionic changes gives hope for similar studies in the future, where it could be extended to brain slices as well as to transgenic animals. This would prove to be less tedious compared to the current approaches, but at the same time provide deep insights to the ionic regulation and signalling network events in a living brain. From our present results, the usage of pH insensitive probes would widen the range of possibilities where biosensors could be adopted for these applications.

Synaptogenesis is a prime feature in a developing brain, connecting its different regions to coordinate the whole body. Though it is an area of ongoing investigation, the actual mechanism underlying the synapse formation is still unknown. Various theories have been proposed of which 'active zone precursor vesicle' hypothesis provides potential possibilities. The interaction studies of the CAZ associated molecules, Bassoon, CtBP1 and CAST, addressed using FRET-FLIM were supportive of this theory, where prefabricated complexes of these proteins were observed at the Golgi network and along neuronal axons to synapses. It is yet to be addressed, how sorting of these proteins at the Golgi apparatus takes place. Though Bassoon and CtBP1 are limited to PTVs, the presence of CAST in different vesicle fractions raises questions on the importance of the formation of such trimeric complexes. The possibility for such complex formation and synapse recruitment with a short fragment of Bassoon gets even more intriguing and questions the necessity of the enormous size of the protein, not conserved during evolution. It is still to be known, how the cell regulates the

synthesis of such large proteins which are supposed to play a significant role in synaptogenesis, but at the same time ensures the possibility to replensish and stabilise the developing neuronal network. The fast moving PTVs carrying the preassembled complexes of these scaffolding molecules offers promising possibilities in this aspect. Though Bassoon is one of the earliest proteins present at nascent synapses and has been suggested to be scaffolding in nature, the potential role of Bassoon in the initial moments of synaptogenesis is still a matter of question. The interactions of Bassoon with other potential scaffolding molecules like CtBP1 and CAST could play a significant role in its scaffolding nature. These interactions have been studied at different subcellular compartments, the current imaging techniques proving to monitor them in their natural environment. All the more, improved imaging techniques would be a prerequisite to address the dynamic nature of these complexes. Single molecule FRET-FLIM microscopy could be a promising technique in the future as to address these interactions during their transport from the Golgi network and during the foremost moments of synapse formation. The possibility for simultaneous interaction studies of more than two proteins by FRET using FLIM, would be highly advantageous in this aspect. This would in turn provide deeper understanding on the mechanisms underlying the dynamic nature of synapses as well as on the different signalling pathways involved.

To date, only very few FRET-FLIM studies have been done in living cells, fewer in neurons, due to the high complexity of cells as well as due to the difficulty in interpreting the data. The lifetimes of a fluorescent probe are highly influenced by its microenvironment, which is the basis of FLIM, but at the same time poses difficulties in uncontrolled conditions like a living environment. Studying the Decay Associated Spectra of both donor and acceptor probes provide means of gaining information regarding the sources of individual lifetimes and allows to overcome the foresaid problems to a great extent. This would be important for discrimination of FRET from other cellular influences which deviates the fluorescent properties of probes, possibly leading to false interpretations. The development of better fluorescent probes would be a prerequisite for widening the range of biological applications where FRET-FLIM could prove to be a powerful tool. This would be a major technological breakthrough, bringing promising possibilities for bridging the gaps in the current state of knowledge regarding the different biological questions of interest, not possible to address by existing methods.

REFERENCES

Ahmari, S. E., Buchanan, J., and Smith, S. J. (2000). Assembly of presynaptic active zones from cytoplasmic transport packets. Nat Neurosci *3*, 445-451.

Altrock, W. D., tom Dieck, S., Sokolov, M., Meyer, A. C., Sigler, A., Brakebusch, C., Fassler, R., Richter, K., Boeckers, T. M., Potschka, H.*, et al.* (2003). Functional inactivation of a fraction of excitatory synapses in mice deficient for the active zone protein bassoon. Neuron *37*, 787-800.

Ballestrem, C., and Geiger, B. (2005). Application of microscope-based FRET to study molecular interactions in focal adhesions of live cells. Methods Mol Biol *294*, 321-334.

Bastiaens, P. I., and Squire, A. (1999). Fluorescence lifetime imaging microscopy: spatial resolution of biochemical processes in the cell. Trends Cell Biol *9*, 48-52.

Beechem, J. M., and Haas, E. (1989). Simultaneous determination of intramolecular distance distributions and conformational dynamics by global analysis of energy transfer measurements. Biophys J *55*, 1225-1236.

Ben-Ari, Y. (2002). Excitatory actions of gaba during development: the nature of the nurture. Nat Rev Neurosci *3*, 728-739.

Ben-Ari, Y., Cherubini, E., Corradetti, R., and Gaiarsa, J. L. (1989). Giant synaptic potentials in immature rat CA3 hippocampal neurones. J Physiol *416*, 303-325.

Berman, H. M., Westbrook, J., Feng, Z., Gilliland, G., Bhat, T. N., Weissig, H., Shindyalov, I. N., and Bourne, P. E. (2000). The Protein Data Bank. Nucleic Acids Res *28*, 235-242.

Bevensee, M. O., Cummins, T. R., Haddad, G. G., Boron, W. F., and Boyarsky, G. (1996). pH regulation in single CA1 neurons acutely isolated from the hippocampi of immature and mature rats. J Physiol *494*, 315-328.

Birks, J. B. (1970). Photophysics of Aromatic molecules, John Wiley & Sons Ltd., New York.

Bonazzi, M., Spano, S., Turacchio, G., Cericola, C., Valente, C., Colanzi, A., Kweon, H. S., Hsu, V. W., Polishchuck, E. V., Polishchuck, R. S.*, et al.* (2005). CtBP3/BARS drives membrane fission in dynamin-independent transport pathways. Nat Cell Biol *7*, 570-580.

Borst, J. W., Hink, M. A., van Hoek, A., and Visser, A. J. (2005). Effects of refractive index and viscosity on fluorescence and anisotropy decays of enhanced cyan and yellow fluorescent proteins. J Fluo *15*, 153-160.

Brady, S. T. (1991). Molecular motors in the nervous system. Neuron *7*, 521-533.

Brady, S. T. (1992). Axonal dynamics and regeneration. In Neural Regeneration, A. Gorio, ed., Raven Press Ltd., New York, pp. 7-36.

Bresler, T., Shapira, M., Boeckers, T., Dresbach, T., Futter, M., Garner, C. C., Rosenblum, K., Gundelfinger, E. D., and Ziv, N. E. (2004). Postsynaptic density assembly is fundamentally different from presynaptic active zone assembly. J Neurosci *24*, 1507-1520.

Brunger, A. T. (1988). X-PLOR, 3.1, HHMI, DMBB, Yale University, New Haven, CT.

Burns, M. E., and Augustine, G. J. (1995). Synaptic structure and function: dynamic organization yields architectural precision. Cell *83*, 187-194.

Cases-Langhoff, C., Voss, B., Garner, A. M., Appeltauer, U., Takei, K., Kindler, S., Veh, R. W., De Camilli, P., Gundelfinger, E. D., and Garner, C. C. (1996). Piccolo, a novel 420 kDa protein associated with the presynaptic cytomatrix. Eur J Cell Biol *69*, 214-223.

Chen, Y., Mills, J. D., and Periasamy, A. (2003). Protein localization in living cells and tissues using FRET and FLIM. Differentiation *71*, 528-541.

Couteaux, R., and Pecot-Dechavassine, M. (1970). Synaptic vesicles and pouches at the level of "active zones" of the neuromuscular junction. C R Acad Sci Hebd Seances Acad Sci D *271*, 2346-2349.

Dai, Z., and Peng, H. B. (1996). Dynamics of synaptic vesicles in cultured spinal cord neurons in relationship to synaptogenesis. Mol Cell Neurosci 7, 443-452.

Day, R. N., Periasamy, A., and Schaufele, F. (2001). Fluorescence resonance energy transfer microscopy of localized protein interactions in the living cell nucleus. Methods 25, 4-18.

Deguchi-Tawarada, M., Inoue, E., Takao-Rikitsu, E., Inoue, M., Ohtsuka, T., and Takai, Y. (2004). CAST2: identification and characterization of a protein structurally related to the presynaptic cytomatrix protein CAST. Genes Cells 9, 15-23.

Dick, O., tom Dieck, S., Altrock, W. D., Ammermuller, J., Weiler, R., Garner, C. C., Gundelfinger, E. D., and Brandstatter, J. H. (2003). The presynaptic active zone protein bassoon is essential for photoreceptor ribbon synapse formation in the retina. Neuron 37, 775-786.

dos Remedios, C. G., and Moens, P. D. (1995). Fluorescence resonance energy transfer spectroscopy is a reliable "ruler" for measuring structural changes in proteins. Dispelling the problem of the unknown orientation factor. J Struct Biol 115, 175-185.

Dresbach, T., Hempelmann, A., Spilker, C., tom Dieck, S., Altrock, W. D., Zuschratter, W., Garner, C. C., and Gundelfinger, E. D. (2003). Functional regions of the presynaptic cytomatrix protein bassoon: significance for synaptic targeting and cytomatrix anchoring. Mol Cell Neurosci 23, 279-291.

Dresbach, T., Qualmann, B., Kessels, M. M., Garner, C. C., and Gundelfinger, E. D. (2001). The presynaptic cytomatrix of brain synapses. Cell Mol Life Sci 58, 94-116.

Dresbach, T., Torres, V., Wittenmayer, N., Altrock, W. D., Zamorano, P., Zuschratter, W., Nawrotzki, R., Ziv, N. E., Garner, C. C., and Gundelfinger, E. D. (2006). Assembly of active zone precursor vesicles: obligatory trafficking of presynaptic cytomatrix proteins Bassoon and Piccolo via a trans-Golgi compartment. J Biol Chem 281, 6038-6047.

Elangovan, M., Day, R. N., and Periasamy, A. (2002). Nanosecond fluorescence resonance energy transfer-fluorescence lifetime imaging microscopy to localize the protein interactions in a single living cell. J Microsc 205, 3-14.

Evans, J., and Yue, D. T. (2003). New turf for CFP/YFP FRET imaging of membrane signaling molecules. Neuron 38, 145-147.

Fejtova, A., and Gundelfinger, E. D. (2006). Molecular organization and assembly of the presynaptic active zone of neurotransmitter release. Results Probl Cell Differ 43, 49-68.

Fenster, S. D., Chung, W. J., Zhai, R., Cases-Langhoff, C., Voss, B., Garner, A. M., Kaempf, U., Kindler, S., Gundelfinger, E. D., and Garner, C. C. (2000). Piccolo, a presynaptic zinc finger protein structurally related to bassoon. Neuron 25, 203-214.

Friedman, H. V., Bresler, T., Garner, C. C., and Ziv, N. E. (2000). Assembly of new individual excitatory synapses: time course and temporal order of synaptic molecule recruitment. Neuron 27, 57-69.

Furusawa, T., Moribe, H., Kondoh, H., and Higashi, Y. (1999). Identification of CtBP1 and CtBP2 as corepressors of zinc finger-homeodomain factor deltaEF1. Mol Cell Biol 19, 8581-8590.

Gadella, T. W. J., Jr. , Jovin, T. M., and Clegg., R. M. (1993). Fluorescence lifetime imaging microscopy (FLIM)—spatial resolution of microstructures on the nanosecond time-scale. Biophys Chem 48, 221–239.

Ganguly, K., Schinder, A. F., Wong, S. T., and Poo, M. (2001). GABA itself promotes the developmental switch of neuronal GABAergic responses from excitation to inhibition. Cell 105, 521-532.

Garner, C. C., Kindler, S., and Gundelfinger, E. D. (2000). Molecular determinants of presynaptic active zones. Curr Opin Neurobiol 10, 321-327.

Garner, C. C., Zhai, R. G., Gundelfinger, E. D., and Ziv, N. E. (2002). Molecular mechanisms of CNS synaptogenesis. Trends Neurosci *25*, 243-251.

Goslin, K., Asmussen, H., and Banker, G. (1998). Rat hippocampal neurons in low-density culture. In Banker, G., Goslin, K. (Eds.), Culturing Nerve Cells, MIT Press, Cambridge, MA, pp. 339–370.

Griesbeck, O., Baird, G. S., Campbell, R. E., Zacharias, D. A., and Tsien, R. Y. (2001). Reducing the environmental sensitivity of yellow fluorescent protein. Mechanism and applications. J Biol Chem *276*, 29188-29194.

Guerrero, G., and Isacoff, E. Y. (2001). Genetically encoded optical sensors of neuronal activity and cellular function. Curr Opin Neurobiol *11*, 601-607.

Guex, N., and Peitsch, M. C. (1997). SWISS-MODEL and the Swiss-PdbViewer: an environment for comparative protein modeling. Electrophoresis *18*, 2714-2723.

Gulyas, A. I., Sik, A., Payne, J. A., Kaila, K., and Freund, T. F. (2001). The KCl cotransporter, KCC2, is highly expressed in the vicinity of excitatory synapses in the rat hippocampus. Eur J Neurosci *13*, 2205-2217.

Gundelfinger, E. D., and tom Dieck, S. (2000). Molecular organization of excitatory chemical synapses in the mammalian brain. Naturwissenschaften *87*, 513-523.

Habuchi, S., Cotlet, M., Hofkens, J., Dirix, G., Michiels, J., Vanderleyden, J., Subramaniam, V., and Schryver, F. C. D. (2002). Resonance Energy Transfer in a Calcium Concentration-Dependent Cameleon Protein. Biophys J *83*, 3499–3506.

Hammerschlag, R., Cyr, J. L., and Brady, S. T. (1994). Axonal Tansport and the Neuronal Cytoskeleton. In Basic Neurochemistry, Raven Press Ltd., New York, pp. 545-571.

Hidalgo Carcedo, C., Bonazzi, M., Spano, S., Turacchio, G., Colanzi, A., Luini, A., and Corda, D. (2004). Mitotic Golgi partitioning is driven by the membrane-fissioning protein CtBP3/BARS. Science *305*, 93-96.

Hink, M. A., Bisselin, T., and Visser, A. J. (2002). Imaging protein-protein interactions in living cells. Plant Mol Biol *50*, 871-883.

Hopf, F. W., Waters, J., Mehta, S., and Smith, S. J. (2002). Stability and plasticity of developing synapses in hippocampal neuronal cultures. J Neurosci *22*, 775-781.

Jares-Erijman, E. A., and Jovin, T. M. (2003). FRET imaging. Nat Biotechnol *21*, 1387-1395.

Jose, M., Nair, D. K., Altrock, W. D., Dresbach, T., Gundelfinger, E. D., and Zuschratter, W. (2007a). Investigating Interactions Mediated by the Presynaptic Protein Bassoon in Living Cells by Fret-Flim. Biophys J.

Jose, M., Nair, D. K., Reissner, C., Hartig, R., and Zuschratter, W. (2007b). Photophysics of Clomeleon by FLIM: Discriminating Excited State Reactions along Neuronal Development. Biophys J *92*, 2237-2254.

Kapusta, P., Erdmann, R., Ortmann, U., and Wahl, M. (2003). Time-resolved fluorescence anisotropy measurements made simple. J Fluo *13*, 179-183.

Karpova, T. S., Baumann, C. T., He, L., Wu, X., Grammer, A., Lipsky, P., Hager, G. L., and McNally, J. G. (2003). Fluorescence resonance energy transfer from cyan to yellow fluorescent protein detected by acceptor photobleaching using confocal microscopy and a single laser. J Microsc *209*, 56-70.

Kemnitz, K., Pfeifer, L., Paul, R., and Coppey-Moisan, M. (1997). Novel detectors for fluorescence lifetime imaging on the picosecond time scale. J Fluo *7*, 93–98.

Khimich, D., Nouvian, R., Pujol, R., Tom Dieck, S., Egner, A., Gundelfinger, E. D., and Moser, T. (2005). Hair cell synaptic ribbons are essential for synchronous auditory signalling. Nature *434*, 889-894.

Kim, S., Ko, J., Shin, H., Lee, J. R., Lim, C., Han, J. H., Altrock, W. D., Garner, C. C., Gundelfinger, E. D., Premont, R. T*., et al.* (2003). The GIT family of proteins forms

multimers and associates with the presynaptic cytomatrix protein Piccolo. J Biol Chem *278*, 6291-6300.

Ko, J., Na, M., Kim, S., Lee, J. R., and Kim, E. (2003). Interaction of the ERC family of RIM-binding proteins with the liprin-alpha family of multidomain proteins. J Biol Chem *278*, 42377-42385.

Kraszewski, K., Mundigl, O., Daniell, L., Verderio, C., Matteoli, M., and De Camilli, P. (1995). Synaptic vesicle dynamics in living cultured hippocampal neurons visualized with CY3-conjugated antibodies directed against the lumenal domain of synaptotagmin. J Neurosci *15*, 4328-4342.

Krueger, S. R., Kolar, A., and Fitzsimonds, R. M. (2003). The presynaptic release apparatus is functional in the absence of dendritic contact and highly mobile within isolated axons. Neuron *40*, 945-957.

Kuner, T., and Augustine, G. J. (2000). A genetically encoded ratiometric indicator for chloride: capturing chloride transients in cultured hippocampal neurons. Neuron *27*, 447-459.

Lakowicz, J. R. (1999). Principles of Fluorescence Spectroscopy, Second edn, Kluwer Academic/Plenum Publishers, New York.

Lakowicz, J. R., Szmacinski, H., Nowaczyk, K., and Johnson, M. L. (1992). Fluorescence lifetime imaging of free and protein-bound NADH. Proc Natl Acad Sci U S A *89*, 1271-1275.

Landis, D. M., Hall, A. K., Weinstein, L. A., and Reese, T. S. (1988). The organization of cytoplasm at the presynaptic active zone of a central nervous system synapse. Neuron *1*, 201-209.

Laskowski, R. A., Rullmannn, J. A., MacArthur, M. W., Kaptein, R., and Thornton, J. M. (1996). AQUA and PROCHECK-NMR: programs for checking the quality of protein structures solved by NMR. J Biomol NMR *8*, 477-486.

Lippincott-Schwartz, J., and Patterson, G. H. (2003). Development and Use of Fluorescent Protein Markers in Living Cells. Science *300*, 87-90.

Llopis, J., McCaffery, J. M., Miyawaki, A., Farquhar, M. G., and Tsien, R. Y. (1998). Measurement of cytosolic, mitochondrial, and Golgi pH in single living cells with green fluorescent proteins. Proc Natl Acad Sci U S A *95*, 6803-6808.

Lodish, H., Berk, A., Zipursky, S. L., Matsudaira, P., Baltimore, D., and Darnell, J. (2000). Nerve Cells. In Molecular Cell Biology, W.H. Freeman and Company, New York, pp. 911-967.

Loefroth, J. E. (1986). Time-Resolved Emission Spectra, Decay-Associated Spectra and Species-Associated Spectra. J Phys Chem *90*, 1160-1168.

Matteoli, M., Takei, K., Perin, M. S., Sudhof, T. C., and De Camilli, P. (1992). Exo-endocytotic recycling of synaptic vesicles in developing processes of cultured hippocampal neurons. J Cell Biol *117*, 849-861.

Miyawaki, A., Llopis, J., Heim, R., McCaffery, J. M., Adams, J. A., Ikura, M., and Tsien, R. Y. (1997). Fluorescent indicators for Ca2+ based on green fluorescent proteins and calmodulin. Nature *388*, 882-887.

Nair, D. K., Jose, M., Kuner, T., Zuschratter, W., and Hartig, R. (2006). FRET-FLIM at nanometer spectral resolution from living cells. Optics Express *14*, 12217-12229.

O'Connor, D. V., and Phillips., D. (1984). Time-Correlated Single Photon Counting, Academic Press, New York.

Ohtsuka, T., Takao-Rikitsu, E., Inoue, E., Inoue, M., Takeuchi, M., Matsubara, K., Deguchi-Tawarada, M., Satoh, K., Morimoto, K., Nakanishi, H., and Takai, Y. (2002). Cast: a novel protein of the cytomatrix at the active zone of synapses that forms a ternary complex with RIM1 and munc13-1. J Cell Biol *158*, 577-590.

Ormo, M., Cubitt, A. B., Kallio, K., Gross, L. A., Tsien, R. Y., and Remington, S. J. (1996). Crystal structure of the Aequorea victoria green fluorescent protein. Science *273*, 1392-1395.

Patterson, G. H., Piston, D. W., and Barisas, B. G. (2000). Forster distances between green fluorescent protein pairs. Anal Biochem *284*, 438-440.

Phillips, G. R., Huang, J. K., Wang, Y., Tanaka, H., Shapiro, L., Zhang, W., Shan, W. S., Arndt, K., Frank, M., Gordon, R. E*., et al.* (2001). The presynaptic particle web: ultrastructure, composition, dissolution, and reconstitution. Neuron *32*, 63-77.

Pollok, B. A., and Heim, R. (1999). Using GFP in FRET-based applications. Trends Cell Biol *9*, 57-60.

Richter, K., Langnaese, K., Kreutz, M. R., Olias, G., Zhai, R., Scheich, H., Garner, C. C., and Gundelfinger, E. D. (1999). Presynaptic cytomatrix protein bassoon is localized at both excitatory and inhibitory synapses of rat brain. J Comp Neurol *408*, 437-448.

Rivera, C., Voipio, J., Payne, J. A., Ruusuvuori, E., Lahtinen, H., Lamsa, K., Pirvola, U., Saarma, M., and Kaila, K. (1999). The K+/Cl- co-transporter KCC2 renders GABA hyperpolarizing during neuronal maturation. Nature *397*, 251-255.

Rizzo, M. A., Springer, G. H., Granada, B., and Piston, D. W. (2004). An improved cyan fluorescent protein variant useful for FRET. Nat Biotechnol *22*, 445-449.

Roos, J., and Kelly, R. B. (2000). Preassembly and transport of nerve terminals: a new concept of axonal transport. Nat Neurosci *3*, 415-417.

Sanders, R., Draaijer, A., Gerritsen, H. C., Houpt, P. M., and Levine, Y. K. (1995). Quantitative pH imaging in cells using confocal fluorescence lifetime imaging microscopy. Anal Biochem *227*, 302-308.

Sanes, J. R., and Lichtman, J. W. (1999). Development of the vertebrate neuromuscular junction. Annu Rev Neurosci *22*, 389-442.

Sauder, M. J. (1999). Blast 2 model, 1.0, Fox Chase Cancer Centre, Philadelphia, PA, USA.

Schagger, H., and von Jagow, G. (1987). Tricine-sodium dodecyl sulfate-polyacrylamide gel electrophoresis for the separation of proteins in the range from 1 to 100 kDa. Anal Biochem *166*, 368-379.

Schmitz, F., Konigstorfer, A., and Sudhof, T. C. (2000). RIBEYE, a component of synaptic ribbons: a protein's journey through evolution provides insight into synaptic ribbon function. Neuron *28*, 857-872.

Schoch, S., and Gundelfinger, E. D. (2006). Molecular organization of the presynaptic active zone. Cell Tissue Res *326*, 379-391.

Shapira, M., Zhai, R. G., Dresbach, T., Bresler, T., Torres, V. I., Gundelfinger, E. D., Ziv, N. E., and Garner, C. C. (2003). Unitary assembly of presynaptic active zones from Piccolo-Bassoon transport vesicles. Neuron *38*, 237-252.

Shepherd, G. M. (1998). The Synaptic Organization of the Brain, 4 edn, Oxford University Press, Inc., New York.

Stoscheck, C. M. (1990). Quantitation of protein. Methods Enzymol *182*, 50-68.

Stryer, L. (1978). Fluorescence energy transfer as a spectroscopic ruler. Annu Rev Biochem *47*, 819-846.

Stryer, L., and Haugland, R. P. (1967). Energy transfer: a spectroscopic ruler. Proc Natl Acad Sci U S A *58*, 719-726.

Takao-Rikitsu, E., Mochida, S., Inoue, E., Deguchi-Tawarada, M., Inoue, M., Ohtsuka, T., and Takai, Y. (2004). Physical and functional interaction of the active zone proteins, CAST, RIM1, and Bassoon, in neurotransmitter release. J Cell Biol *164*, 301-311.

tom Dieck, S., Altrock, W. D., Kessels, M. M., Qualmann, B., Regus, H., Brauner, D., Fejtova, A., Bracko, O., Gundelfinger, E. D., and Brandstatter, J. H. (2005). Molecular

dissection of the photoreceptor ribbon synapse: physical interaction of Bassoon and RIBEYE is essential for the assembly of the ribbon complex. J Cell Biol *168*, 825-836.

tom Dieck, S., Sanmarti-Vila, L., Langnaese, K., Richter, K., Kindler, S., Soyke, A., Wex, H., Smalla, K. H., Kampf, U., Franzer, J. T*., et al.* (1998). Bassoon, a novel zinc-finger CAG/glutamine-repeat protein selectively localized at the active zone of presynaptic nerve terminals. J Cell Biol *142*, 499-509.

Tramier, M., Gautier, I., Piolot, T., Ravalet, S., Kemnitz, K., Coppey, J., Durieux, C., Mignotte, V., and Coppey-Moisan, M. (2002). Picosecond-hetero-FRET microscopy to probe protein-protein interactions in live cells. Biophys J *83*, 3570-3577.

Tramier, M., Kemnitz, K., Durieux, C., and Coppey-Moisan, M. (2004). Picosecond time-resolved microspectrofluorometry in live cells exemplified by complex fluorescence dynamics of popular probes ethidium and cyan fluorescent protein. J Microsc *213*, 110-118.

Truong, K., Sawano, A., Mizuno, H., Hama, H., Tong, K. I., Mal, T. K., Miyawaki, A., and Ikura, M. (2001). FRET-based in vivo Ca2+ imaging by a new calmodulin-GFP fusion molecule. Nat Struct Biol *8*, 1069-1073.

Van Der Meer, B. W., Coker, G., and Chen, S. S.-Y. (1994). Resonance Energy Transfer:Theory and Data, VCH Publishers Inc., New York.

Vriend, G. (1990). WHAT IF: a molecular modeling and drug design program. J Mol Graph *8*, 52-56, 29.

Wang, X., Kibschull, M., Laue, M. M., Lichte, B., Petrasch-Parwez, E., and Kilimann, M. W. (1999). Aczonin, a 550-kD putative scaffolding protein of presynaptic active zones, shares homology regions with Rim and Bassoon and binds profilin. J Cell Biol *147*, 151-162.

Wang, Y., Liu, X., Biederer, T., and Sudhof, T. C. (2002). A family of RIM-binding proteins regulated by alternative splicing: Implications for the genesis of synaptic active zones. Proc Natl Acad Sci U S A *99*, 14464-14469.

Winter, C., tom Dieck, S., Boeckers, T. M., Bockmann, J., Kampf, U., Sanmarti-Vila, L., Langnaese, K., Altrock, W., Stumm, M., Soyke, A*., et al.* (1999). The presynaptic cytomatrix protein Bassoon: sequence and chromosomal localization of the human BSN gene. Genomics *57*, 389-397.

Wu, P., and Brand, L. (1994). Resonance energy transfer: methods and applications. Anal Biochem *218*, 1-13.

Zamorano, P. L., and Garner, C. C. (2001). Unwebbing the presynaptic web. Neuron *32*, 3-6.

Zapata-Hommer, O., and Griesbeck, O. (2003). Efficiently folding and circularly permuted variants of the Sapphire mutant of GFP. BMC Biotechnol *3*, 5.

Zhai, R., Olias, G., Chung, W. J., Lester, R. A., tom Dieck, S., Langnaese, K., Kreutz, M. R., Kindler, S., Gundelfinger, E. D., and Garner, C. C. (2000). Temporal appearance of the presynaptic cytomatrix protein bassoon during synaptogenesis. Mol Cell Neurosci *15*, 417-428.

Zhai, R. G., and Bellen, H. J. (2004). The architecture of the active zone in the presynaptic nerve terminal. Physiology (Bethesda) *19*, 262-270.

Zhai, R. G., Vardinon-Friedman, H., Cases-Langhoff, C., Becker, B., Gundelfinger, E. D., Ziv, N. E., and Garner, C. C. (2001). Assembling the presynaptic active zone: a characterization of an active one precursor vesicle. Neuron *29*, 131-143.

Ziv, N. E., and Garner, C. C. (2001). Principles of glutamatergic synapse formation: seeing the forest for the trees. Curr Opin Neurobiol *11*, 536-543.

Ziv, N. E., and Garner, C. C. (2004). Cellular and molecular mechanisms of presynaptic assembly. Nat Rev Neurosci *5*, 385-399.

ABBREVIATIONS

% (vol/vol)	percent by volume
% (w/v)	percent by mass
2D	two dimensional
3D	three dimensional
°C	degree celsius
μF	microfarad
μg	microgram
μl	microlitre
μm	micrometer
η	refractive index
λ	wavelength
γ	gamma
κ^2	orientation factor
Ω	Ohm
τ	lifetime
τ_A	acceptor lifetime
τ_D	donor lifetime
τ_{DA}	donor lifetime in presence of acceptor
τ_{mean}	mean lifetime
A	Avogadro number
aa	amino acid
acorr	autocorrelation
ADC	Analog to Digital Converter
Amp	amplifier
Ar	argon
AZ	Active Zone
Bicine	N,N-bis-(2-hydroxyethyl)-glycine
bp	base pair
BSA	bovine serum albumin
Bsn	Bassoon
C. *elegans*	*Caenorhabditis elegans*
C1/C2	protein kinase C-domain 1/ protein kinase C-domain 2
Ca^{2+}	calcium ion
CASK	calcium/Calmodulin-dependent serine protein kinase
CAST	CAZ associated structural protein
CAZ	Cytomatrix at the Active Zone
CC	coiled coil

CCD	Charge Coupled Device
cDNA	complementary DNA
CFD	Constant Fraction Discriminator
CFP	Cyan Fluorescent Protein
Cl$^-$	chloride ion
CNS	Central Nervous System
COS-7	african green monkey cell line
C-terminal	carboxy-terminal
CtBP	C-terminal Binding Protein
DAS	Decay Associated Spectra
DIC	Differential Interference Contrast
DIV	days in vitro
DL	Delay Line
DMEM	Dulbecco´s Modified Eagle Medium
DMSO	dimethyl sulfoxide
DNA	deoxyribonucleic acid
DNAse	deoxyribonuclease
dNTPs	deoxyribonucleotide triphosphate
DTT	dithiothreitol
Δ	deletion
E_{Cl}	electrochemical equilibrium potential
ECFP	enhanced CFP
E. coli	*Escherichia coli*
ECL	enhanced chemiluminiscence
EDTA	ethylenediamine-N,N,N`,N`-tetraacetic acid
EGFP	enhanced GFP
EGTA	ethylene glycol-bis(2-aminoetylether)-N,N,N',N'-tetraacetic acid
em	emission
ERC	ELKS/Rab6-interacting protein 2/CAST
ex	excitation
EYFP	enhanced YFP
FC	fibre coupler
Fig.	figure
FLIM	Fluorescence Lifetime Imaging
FPLC	Fast Performance Liquid Chromtaography
FRET	Förster's/Fluorescence Resonance Energy Transfer
FWHM	Full Width at Half Maximum
g	gram
GABA	γ-aminobutyric-acid

GABA$_A$	GABA$_A$ receptor
GFP	Green Fluorescent Protein
GIT	G protein-coupled receptor kinase interactor
h	hour
HBSS	Hank's Balanced Salt Solution
HEPES	N-2-Hydroxyethyl piperazine-N'-2-ethane sulfonic acid
Hg	mercury
Hz	Herz
i.e.	that is
IF	immunofluorescence
I	iris
IP	immunoprecipitation
IPTG	isopropyl-β-D-1-thiogalactopyranoside
IRF	Instrument Response Function
K$^+$	potassium ion
kb	kilo base pair
KD	Karl Diesseroth
kDa	kilo Dalton
kV	kilo volt
l	litre
L	lens
LAR1	Leukocyte Antigen-Related protein
LASER	Light Amplification by Stimulated Emission of Radiation
LB	Luria-Bertani
Liprin	LIP related protein
M	molar
M1-4	mirrors 1-4
mA	milliampere
MCA	Multi-Channel Analyser
MCP	Multi-Channel Plate
MES	2-(N-Morpholino)-ethane sulphonic acid monohydrate
min	minutes
mg	milligram
ml	millilitre
mM	millimolar
MOPS	3-(N-Morpholino)-propane sulphonic acid
mOsm	milliosmolar
Munc13	Mammalian homologue of UNC13
mut	mutant

mV	millivolt
N	Normal
n	number of measured cells
Na	sodium
Na$^+$	sodium ion
ND	neutral density
nm	nanometer
ns	nanosecond
N-terminal	amino-terminal
OCFD	Optical Constant Fraction Discriminator
O.D.	optical density
PAGE	polyacrylamide gel electrophoresis
PC	personal computer
PBH	Piccolo-Bassoon-Homology-Domain
PBS	phosphate buffered saline
PCR	polymerase chain reaction
PDZ	PSD-95/Dlg/ZO-1
Pfu	*Pyrucoccus furiosus*
PMT	Photo-Multiplier Tube
PRA1	Prenylated Rab3 Acceptor protein
ps	picosecond
PSD	postsynaptic density
PTV	Piccolo-Bassoon-Transport Vesicle
QA	Quadrant Anode
r	inter-chromophore distance between the donor and the acceptor
R$_0$	Förster distance
R	intensity ratio of acceptor to donor emission maxima
RIM	Rab3A interacting molecule
RIMBP	RIM-binding protein
RNase	ribonuclease
ROI	Region of Interest
rpm	revolutions per minute
RT	room temperature
s	second
S	micrometer screw
SAS	Species Associated Spectra
SDS	sodium dodecyl sulfate
SDS-PAGE	sodium dodecyl sulfate-polyacrylamide gel electrophoresis

SH3	Src homology 3 domain
SV	synaptic vesicle
TAE	Tris-Acetate-EDTA
TAC	Time to Amplitude Converter
Taq	*Thermus aquaticus*
TBE	Tris-Borate-EDTA
TBTC	Tributyltin Chloride
TEMED	N,N,N',N'-Tetramethylethylenediamine
TIRF	Total Internal Reflection
Tris	Tris(hydroxymethyl)-aminomethane
Tris –HCl	Tris(hydroxymethyl)-aminomethanhydrochloride
U	unit
UNC13	Uncoordinated movement 13
UV	ultraviolet
VAMP	Vesicle Associated Membrane Protein
WB	Western Blot
YFP	Yellow Fluorescent Protein
Zn	double zinc finger

CURRICULUM VITAE

PERSONAL INFORMATION

- Name: Mini
- Family Name: Jose
- Date of birth: 26th December 1979
- Place of birth: Kanjirapally, Kerala, India
- Nationality: Indian
- Parents: Late Prof. Dr. P. K. Jose
            Annamma Jose
- Spouse: Deepak Kumaran Nair
- Child: Naina Maria Deepak

EDUCATION

1985-1988 *1988-1995* *School*	St. Joseph's Anglo Indian Girl's High School, Calicut, Kerala Mount Carmel Girl's High School, Kottayam, Kerala
1995-1997 *Pre Degree*	B.C.M. College, Mahatma Gandhi University, Kottayam, Kerala
1997-2000 *Bachelor of Science/* *Physics*	B.C.M. College, Mahatma Gandhi University, Kottayam, Kerala
2000-2002 *Master of Science/* *Physics*	Indian Institute of Technology, Madras, Tamil Nadu
Oct 2002- April 2007 *PhD/Biophysics*	Leibniz Institute for Neurobiology, Magdeburg,Germany

AWARDS RECEIVED

1995	Proficiency Prize for Academic Excellence
1997-2000	Mahatma Gandhi University Merit Scholarship
1997-2000	Scholarship awarded for the highest marks

1999-2000   Best Outgoing Student

2001-2002   Institute Merit Scholarship

SCIENTIFIC PROJECTS

2001   Cochin University of Science and Technology, Kerala
                Project work on *"Photothermal Optics Induced by Lasers"*,
                International School of Photonics, Cochin University of Science
                and Technology, Kerala

2001-2002   Indian Institute of Technology, Madras
                Master's project on *"Change of dipole moment in the excited
                state, diffraction efficiency and relaxation profiles of some laser
                dyes"*, Ultrafast Lasers and Fluorescence Microscopy Laboratory,
                Indian Institute of Technology, Madras.

24th April 2007, Magdeburg   _____

                                                Mini Jose

SCIENTIFIC PUBLICATIONS

PUBLISHED ARTICLES:

R. J. Rajesh, **Mini Jose** and P. B. Bisht.
Diffraction efficiency of transient grating and relaxation profiles of some laser dyes, (2002). Ind. J. Physics B *76* 737-742.

This issue carried a photo on its front cover from this paper.

Deepak K. Nair, **Mini Jose**, Thomas Kuner, Werner Zuschratter, Roland Hartig.
FRET-FLIM at nanometer spectral resolution from living cells. (2006). Optics Express *14*, 12217-12229.

Equal authorship

Mini Jose, Deepak K. Nair, Carsten Reissner, Roland Hartig, Werner Zuschratter.
Photophysics of Clomeleon by FLIM: Discriminating Excited State Reactions along Neuronal Development. (2007). Biophys J *92*, 2237-2254.

First Author, Corresponding Author

Mini Jose, Deepak K. Nair, Wilko D. Altrock, Thomas Dresbach, Eckart D. Gundelfinger, and Werner Zuschratter.
Investigating Interactions Mediated by the Presynaptic Protein Bassoon in Living Cells by Fret-Flim. (2007). Biophys J.

First Author, Corresponding Author

POSTERS AND PUBLISHED ABSTRACTS:

2003

Werner Zuschratter, **Mini Jose**, Deepak Nair, Daniela Dieterich , Thomas Dresbach, Eckart D. Gundelfinger, Martin Kreutz, Michael Kreutz, Klaus Kemnitz.
Proceedings of Göttingen Neurobiology Conference, June 2003 "Fluorescence Lifetime Imaging and Spectroscopy of xFP-fused Proteins in Hippocampal Cell Cultures using Ultra-Low Excitation Levels and Ultra-Sensitive Imaging Detectors".

Mini Jose, Deepak Nair, Klaus Kemnitz, Werner Zuschratter.
Ultra school on 'Ultrafast processes in Photochemistry and Photobiology', Torun, Poland Aug 2003 ''Fluorescence analysis of molecular dynamics in the synaptic cytomatrix at ultra-low excitation levels''.

Deepak Nair, **Mini Jose**, Klaus Kemnitz, Zdenek Petrasek, Werner Zuschratter.

Ultra school on 'Ultrafast processes in Photochemistry and Photobiology', Torun, Poland Aug 2003 ''FLIM at minimal invasive conditions: Microspectroscopy of the living state''.

2004

Mini Jose, Deepak Nair, Thomas Kuner, Thomas Dresbach, Eckart D. Gundelfinger, Klaus Kemnitz, Werner Zuschratter.

First Westerburg Symposium, 'Spinogenesis and Synaptic Plasticity' Westerburg, Aug 2004 ''Imaging interactions in living hippocampal neurons at minimal invasive conditions using the chloride indicator Clomeleon''.

Ronald Steffen, **Mini Jose**, Deepak Nair, Thomas Dresbach, Thomas Kuner, Eckart D. Gundelfinger, Klaus Kemnitz, Werner Zuschratter.

Annual meeting of SPP 1128 Supramolecular biostructures, Asselheim Nov 2004 ''Fluorescence lifetime imaging Microspectroscopy using ultra-low excitation levels and ultra-sensitive imaging detectors''.

2005

Mini Jose, Deepak Nair, Thomas Dresbach, Klaus Kemnitz, Michael Kreutz, Eckart D. Gundelfinger and Werner Zuschratter
Proceedings of Göttingen Neurobiology Conference, Feb 2005 "Visualisation of Interactions in Living Cells at Ultra-Low Excitation Levels''.

Deepak Nair, **Mini Jose**, Thomas Kuner, Roland Hartig, Carsten Reissner, Klaus Kemnitz, Michael Kreutz, Eckart. D. Gundelfinger and Werner Zuschratter
Proceedings of Göttingen Neurobiology Conference, Feb 2005 ''Imaging Interactions in Living Hippocampal Neurons at Minimal Invasive Conditions Using the Chloride Indicator Clomeleon''.

Mini Jose, Deepak Nair, Ronald Steffen, Roland Hartig, Thomas Kuner, Klaus Kemnitz, Werner Zuschratter
Focus on Microscopy, Jena, March 2005 ''FRET in calcium indicator Cameleon and chloride indicator Clomeleon with maturation of hippocampal neurons''.

Deepak Nair, **Mini Jose**, Ronald Steffen, Roland Hartig, Thomas Kuner, Carsten Reissner, Klaus Kemnitz, Werner Zuschratter
Focus on Microscopy, Jena, March 2005 ''Mapping distances between chromophores in macromolecules using FRET-FLIM microscopy: comparison with predicted 3D structures''.

Mini Jose, Deepak Nair, Ronald Steffen, Roland Hartig, Thomas Kuner, Klaus Kemnitz, Werner Zuschratter

XIth Magdeburg International Neurobiological symposium 'Learning and Memory: Cellular and Systemic Views', May 2005 ''Visualisation of Interactions in Living Cells at Minimal Invasive Conditions''.

Deepak Nair, **Mini Jose**, Ronald Steffen, Roland Hartig, Thomas Kuner, Carsten Reissner, Klaus Kemnitz, Werner Zuschratter
XIth Magdeburg International Neurobiological symposium 'Learning and Memory: Cellular and Systemic Views', May 2005 "Imaging Interactions in Living Hippocampal Neurons Using the Chloride Indicator Clomeleon".

2006
Mini Jose, Deepak Nair, Wilko Altrock, Thomas Dresbach, Thomas Kuner, Carsten Reissner, Eckart D. Gundelfinger, Werner Zuschratter.
International Symposium, Optical Analysis of Biomolecular Machines Berlin, July 2006 "Fluorescence Lifetime Imaging of protein-protein interactions in living hippocampal neurons".

Deepak Nair, **Mini Jose**, Roland Hartig, Thomas Kuner, Klaus Kemnitz, Werner Zuschratter.
International Symposium, Optical Analysis of Biomolecular Machines, Berlin, July 2006 "Imaging spatial and temporal interaction profiles of proteins in living cells using FRET-FLIM".

INVITED TALKS:

Forschungsseminar, Wörlitz, Sep 2003 ''Visualisation of protein-protein interactions in living neurons:- problems and new protein-protein interactions in living neurons:- problems and new approaches''.

International Symposium, Optical Analysis of Biomolecular Machines, Berlin, July 2006 "Visualisation of interactions in living cells using FLIM and FRET".

Physiologie Cellulaire de la Synapse, University of Bordeaux, April 2007 "FRET-FLIM for investigating interactions of synaptic scaffolds in living neurons: a passage from dreams to reality".